Trapping and 3D manipulation of vapor microbubbles: an experimental and theoretical analysis of the Marangoni effect

by

M. Sc. Julio Aurelio Sarabia Alonso

A Dissertation
Submitted to the Program of Optics,
Optics Department
in partial fulfillment of the requirements for the degree of

Ph.D. in Optics

at the

National Institute for Astrophysics, Optics, and Electronics
June, 2022
Tonantzintla, Puebla

Advisor:
Dr. Rubén Ramos García
Principal Research Scientist
Optics Department
INAOE

Abstract

The trapping and manipulation of bubbles have been studied by several researchers from a distinct points of view due to the potential applications in numerous fields. The most common techniques to achieve the trapping and manipulation lie in thermal, optics, and acoustics phenomena. However, these techniques require a complex experimental setup and exhibit a lack of spatial accuracy. Moreover, the techniques are incapable to trap and manipulate bubbles bigger than 50 µm in diameter.

In this thesis, we show both theoretical and experimental results concerning the 3D quasi-steady-state trapping and manipulation mechanism of ethanol vapor microbubbles up to 300 µm of diameter immersed in pure ethanol via optothermal effects employing low optical power, i.e., the laser radiation is absorbed by both a thin film and light bulk absorption in liquids. Thus, heating the liquid up to its boiling point and beyond, inducing a temperature gradient in the liquid. Drag, buoyancy, optical, and Marangoni forces are the main forces present due to both optothermal and hydrodynamics effects.

The controlled generation of the ethanol vapor microbubbles lies on photothermally mechanism produced by the light absorption from silver nanoparticles, previously photodeposited on the core of one distal end of an optical fiber. The other distal end of the optical fiber is coupled to laser radiation, either CW laser or pulsed laser, at low power or low energy, respectively.

The 3D trapping and manipulation of the photothermally-induced ethanol vapor microbubbles, immersed in a glass cell filled with pure ethanol, occurred by employing the same optical fiber configuration. Both the trapping and the manipulation of vapor microbubbles are driven by switching on and off the laser radiation, i.e., spatially switching the origin of the optothermal effects. Moreover, the vapor microbubbles can be trapped and manipulated within an optical fiber array (we explored an experimental setup composed of three fibers coupled to a three CW laser) emitting at different wavelengths at low power.

The heart of the optothermal 3D trapping and manipulation of vapor microbubbles lies in the Marangoni effect. It is triggered by a temperature gradient induced by either light bulk absorption or heating of a substrate like silver nanoparticles absorption (AgNPs, previously photodeposited on the core of the optical fiber). The temperature gradient modules the surface tension of the bubble wall and creates longitudinal and transversal forces just like optical forces, effectively creating a 3D potential well. By numerical simulation, we obtain expressions for the temperature profiles and present analytical expressions for the Marangoni force. The balance of the optothermal forces drives successfully the 3D steady-state trapping and manipulation of the vapor microbubbles up to 150 µm of radius.

Resumen

El confinamiento y manipulación de burbujas ha sido estudiada por varios investigadores desde distintos puntos de vista debido a las posibles aplicaciones en numerosos campos. Las técnicas más comunes para lograr el confinamiento y la manipulación radican en los fenómenos térmicos, ópticos y acústicos. Sin embargo, estas técnicas requieren una configuración experimental compleja y muestran una falta de precisión espacial. Además, las técnicas son incapaces de confinar y manipular burbujas de más de 50 μm de diámetro.

En esta tesis, mostramos resultados tanto teóricos como experimentales sobre el mecanismo de confinamiento y manipulación 3D en estado-casi-estacionario de microburbujas de vapor de etanol de hasta 300 μm de diámetro sumergidas en etanol puro a través de efectos optotérmicos que emplean baja potencia óptica, es decir, la radiación láser es absorbida tanto por una película delgada como por una absorción ligera a granel en líquidos. Por tanto, calentar el líquido hasta su punto de ebullición y más allá, induce un gradiente de temperatura en el líquido. Las fuerzas de arrastre, flotabilidad, ópticas y de Marangoni son las principales fuerzas presentes debido a los efectos optotérmicos e hidrodinámicos.

La generación controlada de microburbujas de vapor de etanol se basa en un mecanismo optotérmico producido por la absorción de luz de nanopartículas de plata, previamente fotodepositadas en el núcleo de un extremo distal de una fibra óptica. El otro extremo distal de la fibra óptica está acoplado a la radiación láser, ya sea láser CW o láser pulsado, a baja potencia o baja energía, respectivamente.

El atrapamiento y manipulación 3D de las microburbujas de vapor de etanol inducidas optotérmicamente, sumergidas en una celda de vidrio llena de etanol puro, se produjo empleando la misma configuración de fibra óptica. Tanto el confinamiento como la manipulación de las microburbujas de vapor son impulsados por el encendido y apagado de la radiación láser, es decir, cambiando espacialmente el origen de los efectos optotérmicos. Además, las microburbujas de vapor se pueden atrapar y manipular dentro de un arreglo de fibras ópticas (exploramos una configuración experimental compuesta por tres fibras) acopladas a tres láseres de onda continua CW que emiten en diferentes longitudes de onda a baja potencia.

El corazón del atrapamiento y manipulación optotérmica en 3D de microburbujas de vapor radica en el efecto Marangoni. Este efecto se desencadena por un gradiente de temperatura inducido por la absorción de la radiación láser, tanto por una absorción ligera a granel en líquidos como por una película delgada (nanopartículas de plata, AgNP, previamente fotodepositadas en el núcleo de las fibra óptica). El gradiente de temperatura modula la tensión superficial de la pared de la burbuja y crea fuerzas longitudinales y transversales al igual que las fuerzas ópticas, creando efectivamente un pozo de potencial 3D. Mediante simulación numérica, obtenemos expresiones para los perfiles de temperatura

y presentamos expresiones analíticas para la fuerza de Marangoni. El equilibrio de las fuerzas optotérmicas impulsa con éxito la captura y manipulación 3D en estado estacionario de las microburbujas de vapor de hasta 150 µm de radio.

Acknowledgments

I am so grateful to **Dr. Rubén Ramos García** for his unique and warm way of providing me guidance, for his continuous support throughout my stay at *INAOE*, and for his coaching and encouragement, thank you a lot Doc Rubén !!

I would like to thank the National Council of Science and Technology, *CONACyT*, for their financial support.

I wish to thank and acknowledge the National Institute for Astrophysics, Optics, and Electronics, *INAOE*, for both receiving me and educating me through its academic staff and researchers.

I would like to thank to people who have stand by me: Gaby, Juan, Julían, Nancy, Manuel, Jorge (George), Rocío, Nahum, Rosa, Manfred, Sani, and Lupita.

Finally, I would like to thank my parents for their tireless and unconditional love, I am in debt to you; ***Mauris and Lulú***.

Dedication

I have no words to describe my *love* and *gratitude* to my parents and siblings, at any moment I have needed any kind of support they have been next to me; each step I have taken has been both accompanied and supported by them, thank you so much.

It is hard to figure out my life without the help, tips, and support that everyone has given to me: relatives, friends, professors, and academic mates, I am in debt to you.

Finally, I would like to write down a few words that my parents told me throughout my whole life and they are always present in my mind: “Si deseas algo, si quieres tener más …, hay que chingarle más (trabajar duro), no hay de otra !!”

This little trip have begun seven years ago and it has turned my whole life around, today I am a completely different person with more doubts but more self-confidence.

To my Iktan & Elian.

Contents

1

Chapter 1. Introduction *19*

History and development of the generation, trapping, and manipulation of microbubbles 19

Mechanism of generation of microbubbles 21

- Acoustic 21
- Electrolysis 22
- Hydrodynamic 23
- Thermal 24
- Optical 25

Mechanisms for trapping and manipulation of microbubbles 26

- Acoustic 26
- Electric 27
- Thermal 28
- Electrocapillary 29
- Hydrodynamic 30
- Chemical 31
- Magnetic 31
- Optics 32

Optothermal effects 32

Application of the microbubbles 33

Thesis structure 34

- Chapter 2 34
- Chapter 3 34
- Chapter 4 34
- Chapter 5 35
- Chapter 6 35
- Chapter 7 36
- Chapter 8 36
- Chapter 9 36

Chapter 2. Phase changes and nucleation *37*

- Phase changes in liquids 37
- Nucleation theory 38

Superheated liquid 41

- Laser heating 41
- Boiling crisis 42

Dynamics of spherical bubbles 43

- Bubble collapse 43
- Rayleigh-Plesset equation 44
- Bubble collapse near a solid wall 46

Chapter 3. Dynamics of the trapping and 3D manipulation of microbubbles *48*

Surface tension 48
Cohesive forces 48
Stokes law 49
Buoyancy force 50
Optical forces 50
Optical forces on a vapor bubble 53
Marangoni force 54
Inertia force 55

Chapter 4. Trapping and 2D manipulation of microbubbles by low power CW laser .. 56
Experimental description 56
Experimental results 58
Discussion 60
Conclusions 65

Chapter 5. Trapping and 3D manipulation of microbubbles by pulsed laser 66
Experimental description 66
Experimental results 67
Discussion 70
Conclusions 74

Chapter 6. Trapping and 3D manipulation of microbubbles by CW laser at low power 76
Experimental description 76
Experimental results 77
Discussion 80
Conclusions 86

Chapter 7. 3D steady-state trapping and manipulation of microbubbles by the Marangoni force 87
Experimental description 87
Experimental results 88
Discussion 89
Conclusions 95

Chapter 8. General conclusions and future work 96
Conclusions 96
Future work 97

Chapter 9. Productions 98
List of publications 98
Proceedings 98

Bibliography 101

List of Figures

Fig. 1.1 Bubble generation driven by an acoustic field, usually induced by a piezoelectric transducer attach toa resonator cavity. 22

Fig. 1.2 Generation of bubbles by electrolysis[49,50]. 23

Fig. 1.3 (a) Example of hydrodynamic cavitation produced on a propeller (b) The violent collapse of the bubbles produce structural damage on the turbine impellers. Images taken from Ref [53]. 23

Fig. 1.4 Classification of boiling on the basis of the presence of bulk fluid motion[55]. 24

Fig. 1.5 Classification of boiling on the basis of the presence of bulk liquid temperature[55]. 25

Fig. 1.6 Schematic of a bubble-based micro-object manipulator with three bubble operations: creation, transportation and elimination. (a) and (b) A bubble created from the top platinum electrodes by electrolysis can push a micro-object while being transported by EWOD. (c) and (d) If the bubble is not needed, it can be eliminated in the elimination site by a Pt-catalyzed electrochemical reaction. Note that the elimination Pt electrode is covered with a thin porous Teflon layer. Figure taken from Ref [65]. 28

Fig. 1.7 Microbubble displacement induced by thermal gradients. (a) A photo taken during the fabrication process is shown in figure 2, where there are 63 heaters (7×9 array) on a single device chip. The dimensions of each heater are $8 \times 23\ \mu m^2$ and the distances between heaters are 93 μm (in the horizontal direction) and 134 μm (in the vertical direction). To connect the heaters with the electrical circuits on a PCB (printed circuit board), a 0.4 μm thick Al film was coated and patterned to form the final metal leads. (b) Single thermal bubble departure and return driving by a pulsed heating power of 103 mW. Images taken from ref [44]. 29

Fig. 1.8 Oscillating hydrogen bubbles by electrocapillary. (a) Scheme of the slightly deformed spherical bubble, sitting on the Pt electrode, and the carpet of microbubbles beneath, with their relevant geometric parameters. (b) Electric current I (solid line) and aspect ratio H* of the bubbles versus time in 1 mol dm^{-3} H_2SO_4 at −5 V[67]. 30

Fig. 1.9 Polystyrene microspheres (10 μm) trapped in steady streaming eddies generated by different geometries. All trapping was performed at very low particle densities, so we show an "×" to indicate symmetric, but unfilled, trapping locations. Image i displayed no stable trapping sites for the range of conditions used here. The arrow denotes fluid oscillation direction. Figure taken from ref [71]. 30

Fig. 1.10 Locomotion of oxygen bubbles in the upright elongated cell. (a) Oxygen bubbles movement perpendicular to the anode surface during oxygen evolution reaction without magnetic field. (b) Oxygen bubbles away from the magnet when the magnet N-pole perpendicular to the electrode. (c) Oxygen bubbles movement parallel to the anode surface during oxygen evolution reaction when the magnet S-pole faced with the anode. Figure taken from ref [74]... 31

Fig. 1.11 Demonstration of three-dimensional optical trapping of a microbubble in the inverted scanning optical tweezers (a) Direction of forces on a microbubble in the inverted optical tweezers. (b) Experimental set-up for optical trapping of microbubbles. (c-f) Demonstration of microbubbles manipulation by optical trapping in the inverted scanning optical tweezers[39]. 32

Fig. 1.12 Trapping and manipulation of microparticles by optothermal effects. (a) Optical set up. A 1W, 532 nm laser is focused onto a 1μm a-Si:H film. (b) Experimental image of the ring projected on the sample. (c) Schematic of the model. The $z = 0$ plane is placed at the glass-water interface and the beam waist is placed at a distance z_0 = - 95 μm. (d) Temperature profile and (e) convective currents field obtained from COMSOL Multiphysics simulations[77]. 33

Fig. 2.1 Phase diagram of water (water temperature T as a function of pressure P). The yellow dot represents the ambient pressure at room temperature, whereas the arrows indicate the paths to induce either boiling or cavitation[90,91]. 37

Fig. 2.2 Spherical vapor bubble of radius R in an equilibrium within a liquid. p_∞ represents the pressure of the surrounding liquid, p_v is the vapor pressure, and p_g is the partial pressure of the gas within the bubble.. 39

Fig. 2.3 Different boiling regimes in pool boiling for water. (a) Natural convection boiling. (b) Nucleate boiling. (c) Transition boiling. (d) Film boiling, also called boiling crisis[110]. 43

Fig. 2.4 Non-spherical bubble collapse at $\gamma = 1$.. 46

Fig. 3.1 Sketch of the cohesive forces between liquid molecules. 48

Fig. 3.2 Operation range of intermolecular forces. Repulsive forces are the ones that operate closest to the particle.. 49

Fig. 3.3 Optical forces on a dielectric particle[7]. 51

Fig. 3.4 Gradient force on a particle whose size is comparable with the wavelength used and refractive index $n_p > n_m$. 52

Fig. 3.5 Scattering force on a particle whose size is comparable with the wavelength used and $n_p > n_m$. 53

Fig. 3.6 Gradient force on a vapor bubble, $n_B < n_m$. 54

Fig. 3.7 Marangoni force over a vapor microbubble. 55

Fig. 4.1 Experimental setup for photodeposition AgNPs at the core of the optical fibers. . 57

Fig. 4.2 Experimental setup for the generation and manipulation of microbubbles. (a) Optical fibers vertically opposed. (b) Optical fibers horizontally opposed. 57

Fig. 4.3 Sequence of birth (a) and growth of a microbubble (b-d) adhered to the tip of an optical fiber. Bright areas represent scatter light picked up by the camera. 58

Fig. 4.4 Snap shots of a travelling microbubble in the +*z* direction between two opposed optical fibers. The bubble is generated in the lower fiber and attracted towards the upper fiber. 59

Fig. 4.5 Snap shots of a travelling microbubble in the -*z* direction between two opposed optical fibers. The bubble is generated in the upper fiber and attracted towards the lower fiber. 59

Fig. 4.6 Manipulation of a microbubble between two horizontally opposed optical fibers (a) due to the switching of the temperature gradients (see Visualization 1). Manipulation of a microbubble in the + *z* and -*z* direction between two vertically opposed and off-axis optical fibers (a) 33 ° (see Visualization 2) and (b) 43 ° (see Visualization 3) respectively. 60

Fig. 4.7 (a) Configuration used to calculate the temperature spatial distribution using COMSOL. The fiber is placed into the cell containing ethanol. (b) Temperature profile from the fiber to the bottom of the cell which in this case r coincides with the *z*-axis. 61

Fig. 4.8 Microbubble radius as function of time. 61

Fig. 4.9 (a) Displacement of a microbubble in the +*z* direction, (b) displacement of a microbubble towards –*z* direction and (c) displacement of microbubble when the optical fibers are off-axis. 63

Fig. 4.10 Marangoni force on a microbubble (with radius R = 110 μm, heat source is placed at r = 0) as a function of the distance (r) between heat source and the microbubble when the heat source is placed at the lower fiber. 64

Fig. 4.11 Microbubble displacement velocity as a function of the distance between the heat source and the microbubble. (a) Dots correspond to experimental data and continuous line corresponds to fittings. (b) Triangles correspond to Marangoni and terminal´s velocities as a result to combining experimental results and continuous lines correspond to fitting of $\boldsymbol{u_M}$ and $\boldsymbol{u_T}$. 65

Fig. 5.1 (a) Experimental setup for the generation and 3D manipulation of microbubbles. A pulsed laser is coupled to the multimode optical fiber using a microscope objective (MO). Bubbles dynamics are viewed with a fast Phantom camera. (b) Image of the distal end of the multimode optical fiber obtained with a SEM after 3.5 dB of attenuation was achieved. (c) Closer view of the optical fiber core showed on (b). 67

Fig. 5.2 Growth of the main-bubble as a function of time. (a) Snapshots of the temporal evolution of the main-bubble radius recorded at 6,600 fps. (b) Blue dots correspond to the measured from the video main-bubble radius. The continuous blue line is fit to a double exponential function. The lower horizontal axis represents the number of coalesced bubbles and the upper one the corresponding elapsed time. The red solid line indicates the calculated radius of the main-bubble as a function of microbubbles generated at 2.1 µJ per pulse-energy at a repetition rate of 10 kHz. 68

Fig. 5.3(a) Profile of the bubble's velocity as a function of the laser energy, extracted from recorded images at 43,000 fps. Continuous lines are fit to an exponential function. (b) Snapshot of the tracers and bubbles when a 2.6 µJ of laser energy was used. White circles and white squares indicate the tracer and bubble displacement, respectively. Both the bubble and the tracer start from the same position at t = 50 µs, however, the bubble moves faster as time goes on. 68

Fig. 5.4 (a) Snapshot of the optothermal generation of microbubbles: (i) maximum bubble size, (ii) bubble collapse, (iii) bubble ejection, (iv-vi) bubble moves away from the optical fiber. (b) 4.2 µJ of laser-pulse energy. (i) Maximum cavitation bubble. (ii-iv) Temporal evolution of the remaining bubble. (v) Bright spots represent scatter laser-light due to AgNPs picked up by the video-camera. (vi) Bubble ejection due to the counterjet. The frame rate in all cases was 43,000 fps 69

Fig. 5.5 Temperature profile at the AgNPs-ethanol interface obtained by solving the heat diffusion equation coupled to the Navier-Stokes equations using COMSOL Multiphysics. The phase explosion is more likely to occur around T_c ~243 °C (continuous red line). The temperature increase at the interface is a linear function of the laser energy. Color solid lines represent the temporal profile of the temperature at the AgNPs-ethanol interface due to light absorption. The blue broken line represents the temporal profile of one laser pulse. The pink double-dot line represents the pure ethanol boiling temperature T_b ~ 78 °C. 71

Fig. 5.6 (a) Free-body diagram of the forces involved in the main-bubble manipulation. (b) Total force over a main-bubble of R = 131 µm illuminated with pulses of 3.7 µJ of energy as a function of the propagation axis.. 73

Fig. 5.7 Spatial displacement of the main-bubble Visualization 5.2. (a) The main-bubble moves in +*z* direction whereas the bubble stream does it in -*z* direction. (b) Total force over a main-bubble around the quasi-steady-state trapping distance for particles of different radii. Total force over a bubble of 129.5 µm of radius (red triangles), 131 µm of radius (blue dots) and 132.5 µm of radius (green squares) obtaining quasi-steady-state trapping at -430.2 µm, -439.7 µm and -451.4µm, respectively. 74

Fig. 6.1 Experimental set up for generation and trapping of microbubbles. The microbubbles are generated at fiber OF_G using a pulsed laser (λ = 532 nm, τ_p = 5 ns) and trapped at fiber OF_T using a CW low power laser (λ = 1550 nm, Power 1–15 mW)....... 77

Fig. 6.2 Generation and 3D trapping of a microbubble for different fiber OF_T positions: facing downwards (A), horizontally 2D, and upwards (G). Bubble release from the fiber OF_G: (B), (E), and (H). Bubble trapping (C), (F), and (I). See Visualizations 6.1, 6.2, and 6.3 for more details. 78

Fig. 6.3 Trapping of microbubbles through a temperature gradient induced with a power of 2 mW for different radii R and its corresponding trapping distance d: (A) $R \sim 32$ µm and $d \sim 71$ µm, (B) $R \sim 42$ and $d \sim 76$ µm, (C) $R \sim 50$ µm and $d \sim 74$ µm, and (D) $R \sim 62$ µm and $d \sim 78$ µm.. 79

Fig. 6.4 Trapping of microbubbles with a power of 2 mW. Large bubbles touch the optical fiber OF_T (A) $R \sim 130$ µm, and (B) $R \sim 333$ µm. For icrobubbles of radius $R \geq 130$ µm trapping becomes unstable and manipulation is not possible................. 80

Fig. 6.5 (A–C) Snapshots show that particles move in opposite direction to the beam propagation at a laser power P = 2 mW. White circles indicate the position of a cluster of several polystyrene microparticles. (D) Profile of the convective currents' velocity as a function of propagation distance *z* measured from the fiber end. Blue dots correspond to the microparticles' velocity whereas red squares correspond to the convective currents obtained from the COMSOL simulation. 80

Fig. 6.6 (A) Temperature distribution on ethanol due to light absorption for a power of 2 mW, (B) longitudinal temperature profile on the propagation axis z for several powers, (C) transverse temperature profile on z_{TH} =75.4 µm, and (D) convective currents velocity produced by the temperature gradient with an optical power of 2 mW. 83

Fig. 6.7 (A) Longitudinal gradient temperature profile along the propagation axis z and (B) transversal gradient temperature profile obtained at $z_{HT} \sim$ 5.4 µm, for 2, 5, 10, and 15 mW obtained through simulation in COMSOL Multiphysics. 84

Fig. 6.8 Total longitudinal force using Eq. 6.7 for microbubble with radii ~32, ~42, ~50, and ~62 µm. The zero crossing displaces to the smaller distances *z* as the convective current increases as discussed in the main text. 85

Fig. 7.1 Experimental setup for the generation and manipulation of microbubbles. Three CW lasers with optical fiber output: multi-mode optical fiber (MMOF) for 445 nm and single-mode optical fiber (SMOF) for 980 nm and 1550 nm. The distal ends of the three optic of the three optical fibers are horizontally placed into a glass cell filled with ethanol. Bubbles manipulation is viewed with a Motic3 camera coupled to a 5x microscope objective (MO). 88

Fig. 7.2 Trapping and manipulation of a microbubble of *R* = 100 µm by optothermal effects induced at a different wavelength with low optical powers. The microbubble is photothermally generated by the CW laser at 445 nm with 13 mW (not shown). (a) Only the CW laser at 445 mW is turned on, inducing the microbubble trapping by the MMOF (OF_1). The scale bar represents 200 µm. (b) The CW laser at 445 nm is turn off and only the CW laser at 980 nm is turned on, inducing the microbubble displacement towards the SMOF (OF_2). (c) The CW laser at 980 nm is turn off and only the CW laser at 1550 nm is turned on, inducing the microbubble displacement towards the SMOF (OF_3). (d) The three CW lasers are turn on, trapping the microbubble at the center of the optical fiber array (see Visualization 7.1). 89

Fig. 7.3 (a) Temperature distribution in ethanol due to bulk absorption extracted from COMSOL simulations (λ = 1,550 nm & 15 mW of optical power). The scale bar represents 200 µm. (b) 3D trapping and manipulation of a bubble of radius *R* = 50 µm, at λ = 1,550 nm and 15 mW. The scale bar represents 100 µm. See Visualization 7.2. (c) Transversal temperature distribution obtained at different positions along the *z*-axis. Continuous lines are fits to Gaussian functions Eq. (7.4). (d) Longitudinal temperature profile along the propagation axis z. The red line is fitted to Eq. (7.5). 91

Fig. 7.4 Marangoni force over a bubble of *R* = 50 µm induced by light bulk absorption of ethanol (blue) and by light absorption from AgNPs photodeposited on the core of an optical fiber (red). (a) Transversal Marangoni force measured at *z* = 80 µm from the fiber tip. (b) Longitudinal Marangoni force. 92

Fig. 7.5 (a) Convective currents velocity profile due to the light absorption at the AgNPs film (λ = 445 nm with 10 mW of optical power) extracted from COMSOL simulations. (b) Convective currents velocity profile due to the light bulk absorption of ethanol (λ = 1,550 nm with 15 mW of optical power) extracted from COMSOL simulations. (c) Transversal drag force along the *z*-axis due to light absorption from AgNPs for a bubble of R = 50 µm. (d) Longitudinal drag force gradient along the z-axis due to light bulk absorption of ethanol for a bubble of R = 50 µm. 93

Fig. 7.6 Optothermal forces on a microbubble of R = 100 µm. (a) Transversal components of the gradient forces $\boldsymbol{F_d}$ (red triangles) and $\boldsymbol{F_M}$ (blue squares). (b) Longitudinal component of FM (blue squares), $\boldsymbol{F_d}$ (red triangles), and $\boldsymbol{F_b}$ (red dots). Since $\boldsymbol{F_M}$ >> $\boldsymbol{F_D}$ and Fb, the microbubble is attracted to the optothermal source, i.e., the distal end of the optical fiber. 94

Chapter 1. Introduction

It is hard to figure out that a bubble, a tiny and common object, could involve an immense amount of processes behind its generation. Bubbles, are ubiquitous to our daily life, they can be found while we bath, dish, drink our coffee cup, or in boiling water. Bubbles, either of air or vapor, offer us a vast spectrum of applications in several fields such as medical diagnostic[1–3], drug delivery[4,5], lithography[6], industry, among others. However, these applications could not be achieved without exerting spatial control over the bubbles.

The words: "*trapping and manipulation*" could seem ordinary and common because we can trap and manipulate objects by ourselves, i.e., with our hands or external tools, nevertheless, our trapping and manipulation capabilities dimmish as we move towards the micro and nanoworld. This world is the one that has given us exciting information concerning our environment and has opened new avenues about life knowledge. It is not possible to talk about *trapping and manipulation* without mentioning the Nobel laureate Arthur Ashkin[7,8]. To be fair we cannot conceive our current understanding of life´s due to his invention, i.e., the optical tweezers. Even though optical tweezers have extended their landscape of contactless trapping and manipulation, it remains complex to trap and sort particles with refractive index n_p smaller than the surrounding medium n_m, i.e., $n_p/n_m < 1$, such as microbubbles[9].

Besides to optical means, several authors has been proposed different techniques for achieving the manipulation of bubbles based on thermal[10–12] and acoustic[13–15] means. Nevertheless, these methods are useful for small bubbles ($R < 30$ μm) and lack of spatially accuracy. In addition, the bubbles cannot be successfully trap due to both hydrodynamics effects and the continuous growing of the bubble that provoke instability in the trap. i.e., the steady-state trapping of the bubble is not possible.

In this chapter, the history of both trapping and manipulation of bubbles will be briefly described. In addition, a classification of the mechanism of microbubbles generation and their manipulation will be discussed. Then, the optothermal technique based on both light absorption and hydrodynamics phenomena is presented as an efficient and prominent method to achieved quasi-steady-state 3D trapping and manipulation of vapor microbubbles employing low optical power. Finally, several applications of microbubbles currently available are going to be presented.

History and development of the generation, trapping, and manipulation of microbubbles

The field of micro and nanomanipulation has been cemented by the wonderful and pioneering work of A. Ashkin for trapping and manipulate dielectric particles with his optical tweezers[7,8,16]. Through the years, optical tweezers have evolved and showed their capabilities to deal with a biological matter like DNA[17,18], cells[17]; microorganisms like worms[19], bacterias[20], metallic particles[21], among others. The vast spectrum of optical tweezers applications seems to be unlimited, however, the trapping of particles with refractive index n_p smaller than the surrounding medium n_m, i.e., $n_p/n_m < 1$, such as microbubbles[9] remains a challenge. This is due to the repelling optical gradient force that pushes the microbubble out of the high-intensity region of the laser beam[22].

Acoustics mechanism (acoustic tweezers) have been proposed to trap an manipulated particles/bubbles since early 1900´s. This mechanism lies in the principle that a particle/bubble immersed into an acoustic field experiencing an acoustic radiation via absorption and reflection, i.e., based on the momentum transfer of acoustic field and acoustic radiation force. Nevertheless, the trapping scale in the radiative acoustic field domain is severely limited by the Rayleigh diffraction limit of the classic wave[23], i.e., not efficient in nano-scale particle sizes[24]. Besides, heating problems during a long term process[25].

In addition, electric fields have been proven to be capable to trap and manipulate particles and bubbles. Electrophoresis, requires a uniform electric field to push charged particles towards opposite charge[26]. On the other hand, dielectrophoresis involves a non-uniform electric field over a neutral particles to induce they displacement. The particle motion depends on relative polarizability of the particle with respect to the fluid. Both electrical mechanism are highly affected by the fluid viscosity, permeability, particle conductivity, and particle size. Moreover, electrophoresis is limited to charged particles and exhibits slow displacement of the particles[27]. Dielectrophoresis is contra-indicated for bio applications due to of high electric field gradients and its forces decreases with particles size[28,29].

Besides the mechanism above mentioned, thermocapillary, also known as Marangoni force, have been proven to be a useful and efficient mechanism not only to trap but also manipulate vapor bubbles, even at large scale. The first experimental study concerning thermocapillary was developed by James Thompson in 1855[30]. In this study, he observed the displacement of a spheric microbubble immersed in a solution, he attributed the bubble´s displacement to the difference in the surface tension between the liquid and the bubble. Ten years later, in 1865, the Italian physicist Carlo Marangoni established in his Ph.D. dissertation that the surface tension between two fluids can be used to induce a force for the displacement of the fluids[31]. This gave the name to the phenomenon, the Marangoni effect. A few decades later, in 1911, J. Hadamard[32] and Rybczynski[33] derived an axial symmetry solution for flow surrounding a spherical bubble. This solution, called the Hadamard-Rybczynski equation, is based on the Navier-Stokes equation coupled to the buoyancy effect and drag force[34,35]. Later, in 1939, Allen V. Hershey[36] determined the dependence of the surface tension of a pure liquid as a function of the temperature, i.e., in most cases, the surface tension of the pure liquids decreases as their temperature increases. Nine years later, in 1948, A. I. Fedosov introduced a mathematical description of the thermocapillary effect in his Ph.D. dissertation[37]. However, it was in 1959 that the first experimental about the microbubble displacement within a measured temperature gradient was demonstrated by Young *et al.*[34]. In their model, spherical air bubbles were introduced into a solution based on an organic liquid *n*-hexadecane and silicone oils, the temperature gradient (electrically induced) was vertically applied to induced the microbubble displacement. Through the years, several experimental and theoretical works have been carried out to prove the thermocapillary capabilities for 2D trapping and manipulate bubbles; R. L. Thompson *et al.*[38] in 1980, Wozniak *et al.*[39] in 1988, Subramanian *et al.*[40] in 1989, K. Takahashi *et al.*[41] in 1999, A. Miniewicz *et al.*[42,43] in 2016.

From this brief historical review, we could say that the Marangoni effect, also known as the thermocapillary effect, has shown to be a wonderful tool to overcome the challenge faced by several trapping approaches where small bubbles (< 5 μm) have been 3D trapped such as optical[44], acoustics, and thermal means. Thermocapillary effects have emerged as an efficient and straightforward tool to accomplish non-invasive trapping and 3D manipulation of microbubbles up to 130 μm of radius. Moreover, the thermocapillary effect can induce larger and large-range forces than optical ones while maintaining the accuracy of spatial control of microbubbles[42,45–47].

Mechanism of generation of microbubbles

At present, the generation of vapor or gas microbubbles within a liquid can be achieved by methods that mainly involve acoustic, chemical, hydrodynamic, thermal, and optical methods. In this section, we are going to discuss the different mechanisms to create microbubbles, i.e., classified into five types depending on the physical mechanism of creation.

Acoustic

The sound wave, a mechanical vibration that travels longitudinally into the medium, has cycles of expansive (crest) and compression (troughs). The expansive cycle also called rarefaction, takes place at the negative amplitude of the sound wave whereas the compression cycle does so at the positive amplitude. According to classical nucleation theory (CNT) the vapor-gas phase in a liquid can be nucleated when the liquid pressure drops below its vapor-gas phase pressure, i.e., when any liquid is irradiated by a sound wave at high intensity (~ 16 kHz to 100 MHz), bubbles cavitation may occur. Once the bubble is generated, the acoustic field modulates the bubble radius, i.e., the cavitation bubbles are not stationary. The expansion and contraction of the bubble radius is driven by the rarefaction and compression cycle[48], respectively. It may induce the violent collapse of the bubble where a flash of light can be observed, as is illustrated in Fig. 1.1.

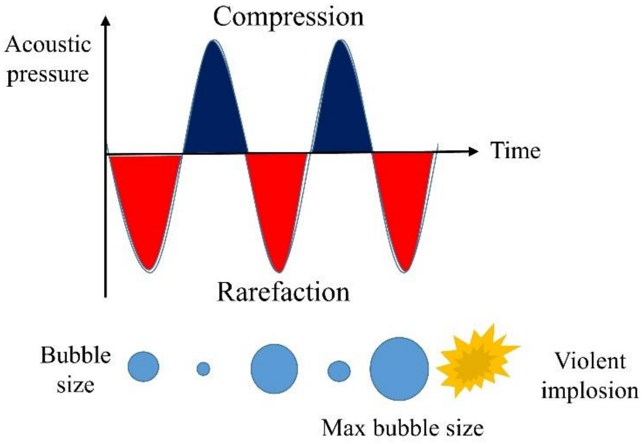

Fig. 1.1 Bubble generation driven by an acoustic field, usually induced by a piezoelectric transducer attach to a resonator cavity.

The sound waves can be classified according to the frequencies *f* as follows:

a. *Infrasound*: $f < 20$ kHz.

b. *Audible*: 20 Hz $< f <$ 20 kHz.

c. *Ultrasound*: $f > 20$ kHz.

It is essential to mention that acoustic generation of bubbles is a complicated task to carry out, because it involves a complex multidisciplinary problem. Furthermore, the bubbles acoustically generated rise up “from nowhere”, i.e., acoustic methods are unable to generate bubbles with spatial accuracy.

Electrolysis

It is a chemical process where the water is separated into its components (hydrogen and oxygen) by applying an electric current. The electric current passed through the water by electrodes (cathode and anode) to induce a chemical change where the water either gains or loses an electron, called reduction or oxidation, respectively. The water surrounding the cathode gets supersaturated with hydrogen and thus the formation and release of hydrogen at the cathode surface at several nucleation spots, therefore hydrogen bubbles (HBs) are generated. The HBs grows until it detaches from the cathode´s surface. In the same way, the oxygen bubbles (OBs) are produced but at the surface of the anode[49,50], as is depicted in Fig. 1.2.

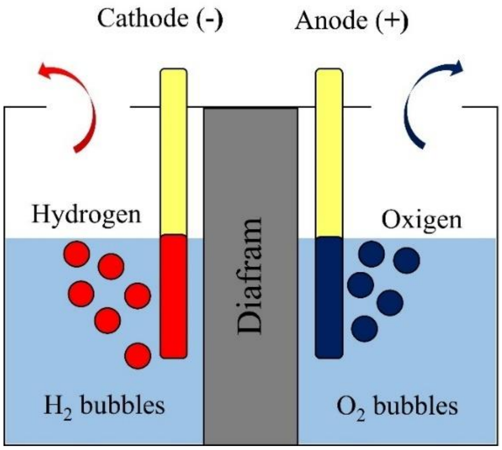

Fig. 1.2 Generation of bubbles by electrolysis[49,50].

Hydrodynamic

It is based on the assumption that any liquid contains either vapor or gas bubbles, these bubbles play as nucleation points, according to the CNT. The fast-moving of a liquid, a mechanical vibration, may induce the liquid pressure locally fall below the vapor pressure at which liquid-vapor phase transition takes place, similar to the acoustic mechanism[13,51].

Another way to produce bubbles by the hydrodynamic mechanism consists in the well-known Venturi effect, i.e., a liquid passing through a constricted area (a pipe) may generate that liquid pressure decay below the vapor pressure, generating a bubble[13,51].

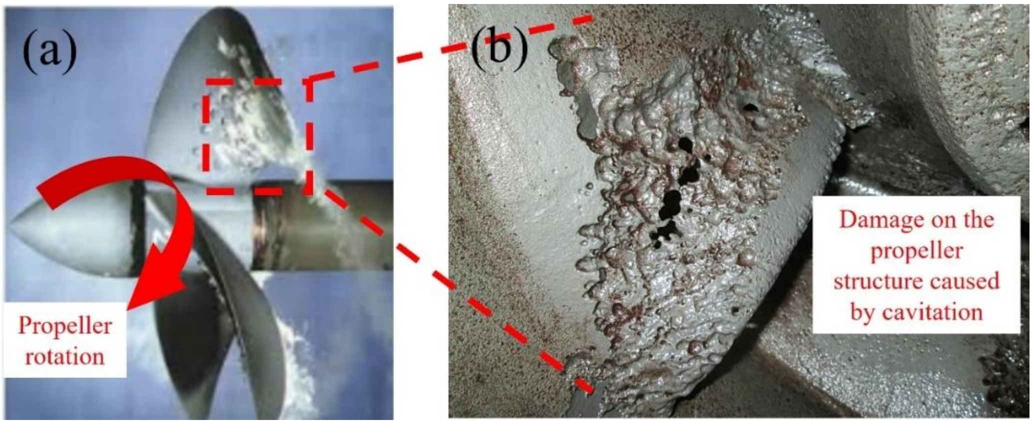

Fig. 1.3 (a) Example of hydrodynamic cavitation produced on a propeller (b) The violent collapse of the bubbles produce structural damage on the turbine impellers. Images taken from Ref [52].

Figure 1.3 shows structural damage to turbine impellers induced by hydrodynamic cavitation.

Thermal

Heat applied to a liquid (either by radiation, diffusion, or conduction) will give more kinetic energy to the liquid molecules and they will move faster and faster leading to the liquid expansion. Liquid molecules require extra kinetic energy to overcome the attraction forces between them. As the liquid heats up, more liquid molecules have enough kinetic energy to escape from the liquid. The most energetic liquid molecules at the surface will escape from the liquid surface as a vapor as it is heated. Eventually, even liquid molecules in the middle of the liquid form bubble composed of gas[53]. This is the so called boiling process. It is important to mention that the gas molecules are the same as they were in the liquid, only now they have more energy. At normal atmospheric pressure, all material have a specific temperature at which boiling process occurs. According to Incropera *et. al.*[54], depending on the presence of bulk fluid motion, boiling process may be classified as:

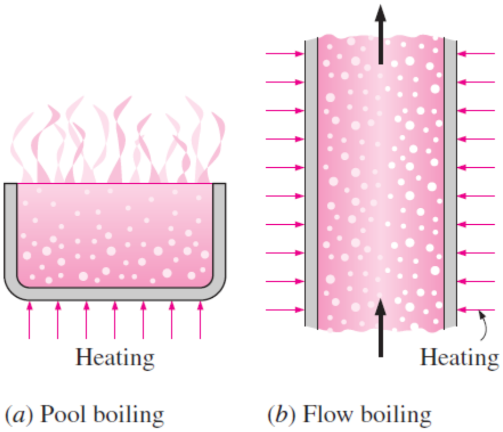

Fig. 1.4 Classification of boiling on the basis of the presence of bulk fluid motion[54].

a. *Pool boiling*: the liquid is quiescent and any motion of the fluid is due to natural convection currents and the motion of the bubbles under the influence of buoyancy.

b. *Forced convection boiling*: the liquid is in constant movement, by either external. Therefore, flow boiling is always accompanied by other convection effects.

Based on the bulk liquid temperature, both pool boiling and forced convection boiling may be subclassified as:

a. *Subcooled boiling*: the saturation temperature is above the temperature of the liquid, so the bubbles are generated at the surface but they may condensate in the liquid.

b. *Saturated boiling*: the saturation temperature is slightly below the temperature of the liquid, the bubbles are generated at the surface and then are expelled through the liquid by the buoyancy force up to reach the liquid surface.

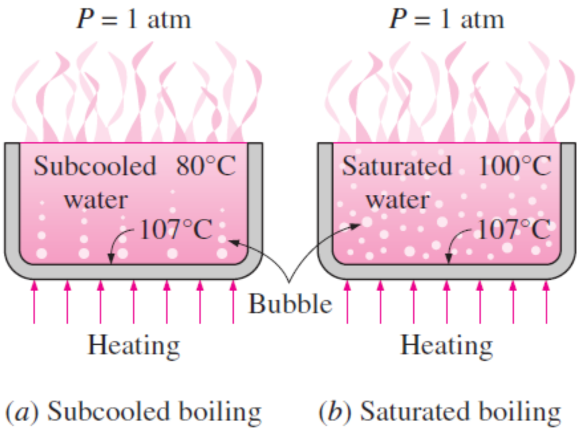

Fig. 1.5 Classification of boiling on the basis of the presence of bulk liquid temperature[54].

Optical

It is based on the principle of light absorption. The electromagnetic waves, coming from the light source are absorbed by the matter and then converted into thermal energy that is transferred to the surrounding liquid, i.e., the liquid molecules received extra kinetic energy to overcome the attraction forces between them, so liquid molecules have enough kinetic energy to escape from the liquid into gas. According to the absorption medium, the light absorption mechanism may be classified as follows:

a. *Bulk absorption*: the laser beam impinges on a highly absorbent liquid at the wavelength used, the energy from the laser is strongly absorbed by the liquid and transferred to the medium.

b. *Particles/thin-film absorption*: the laser beam is irradiated on either a colloidal solution or a metal film and transfer to the fluid.

If the thermal energy, converted from the laser radiation, is high enough to reach the liquid boiling point, the nucleation process will occur and bubbles will be generated.

Bubbles generation induced by optical technics can be achieved using pulsed lasers or CW lasers, however, the mechanism behind the bubbles optically-generated differs depending on the laser source employed: optical breakdown and laser-induced thermal, for pulsed laser and CW laser, respectively. The details concerning both mechanisms will be presented in Chapter 2.

Mechanisms for trapping and manipulation of microbubbles

Through the years, several mechanisms and approaches have been proposed and developed to carry out the trapping and manipulation of microbubbles, independently of the bubble generation mechanism. In this section, we are going to discuss the main mechanism of both trapping and manipulation of vapor or gas microbubbles, i.e., classified into seven types depending on the physical mechanism of creation.

Acoustic

This method employs acoustic waves at high-frequency rates, i.e., f > 20 kHz up to 10 GHz. Typically, acoustic methods use a piezoelectric element placed inside the liquid to induce acoustic waves[14]. When a fluid containing bubbles or particles is irradiated by an acoustic field, the suspended particles suffer steady hydrodynamics forces (time-averaged) which make them drift, attack, or repel one another[15]. Acoustic forces are analog to optical radiation pressure exerted by an laser beam, i.e., acoustic radiation implies an instantaneous pressure gradient in the liquid. However, in general acoustic radiation forces are larger than the optical ones.

Acoustic radiation forces, also known as Bjerknes forces in honor of C. A. Bjerknes and V. F. K. Bjerknes are classified as follows[55–57]:

a. *Primary Bjerknes force* F_{B_j}: this force is related to the bubble attraction or repelling. A bubble immersed into a liquid under the influence of an acoustic field will suffer oscillation in its volume, i.e., the bubble will expand and contract. Depending on the acoustic pressure gradient, these bubbles oscillations may couple to the acoustic field to drive the bubble migration, i.e., the acoustic pressure gradient must be different from zero. The bubbles with a radius lower than the acoustic field resonator will travel above the acoustic pressure gradient whereas the bubbles with a radius larger than the acoustic pressure gradient will travel below the acoustic pressure gradient. The primary Bjerknes force is given by:

$$F_{B_j} = f_{B_j} r, \tag{1.1}$$

$$f_{B_j} = -\frac{4}{3}\pi \langle R^3(t)\, P_{ac}(r,t) \rangle, \tag{1.2}$$

where r is the radial coordinate, $R(t)$ is the variation of the radius of the bubble as a function of the time, $P_{ac} = A(r)exp(-1\omega t)$ is the pressure of the acoustic excitation with amplitude $A(r)$, ω is the angular frequency, and $\langle \ldots \rangle$ represents the temporal average of one oscillation cycle. According to the value of f_{B_j}, the bubble will be either attract or repel, i.e., $f_{B_j} < 0$ the Bjerknes force is negative and the bubbles will be attracted to the acoustic trap, therefore, if $f_{B_j} > 0$ the Bjerknes force is positive, pushing the bubble away from the acoustic trap[15,58].

b. *Secondary Bjerknes force* F_{B_j2}: it is related to the force of attraction or repelling between two bubbles under an acoustic field. The secondary Bjerknes force is given by:

$$f_{B_j2} = -\frac{\rho}{4\pi} \langle V_1 V_2 \rangle \frac{x_2 - x_1}{|x_2 - x_1|}, \tag{1.3}$$

where ρ is the density of the medium containing the bubbles, V_1 and V_2 represent the volume of the bubble, x_1 and x_2 represent the spatial position of the bubbles. The bubbles will be attracted if their radius is less than the resonance one. On the other hand, if the radius of the bubbles is different from each other, the bubbles will repel[15,58,59].

Electric

Several electric techniques are proposed for both trapping and manipulation of microbubbles, techniques that employ an electric field over the bubbles to induce an unbalance on the electrostatic forces of the bubbles up-to techniques for inducing an electric field over the materials for tunning their permeability. The main electric methods are presented as follows:

a. *Dielectrophoresis*: it is based on the application of non-uniform electric fields over a colloidal solution of dielectric particles or microbubbles into a liquid for inducing an unbalance on the electrostatic forces of the particles/bubbles[60,61]. The unbalance of the electrostatic forces drives the dielectric particle/microbubble migration. For most dielectrophoresis cases, the applied electric field in an alternating current signal, produced by a frequency generator (usually sinusoidal frequencies > 100 kHz at magnitudes below 20 V peak-to-peak) [61].

   According to the dielectric particle/microbubble polarization, dielectrophoresis can be classified as positive and negative, i.e., the particle/microbubble is attracted or repelled, respectively. Positive dielectrophoresis occurs when the particle is more polarized to the liquid that contains it, while negative dielectrophoresis occurs when the particle/microbubble is less polarized to the liquid that contains it[61].

b. *Electrowetting on dielectric EWOD*: it is based on the tunning of the permeability of hydrophobic materials by applying an electric field[62]. The change in the permeability induces that a bubble/droplet placed on the hydrophobic material tends to elongate at one end, so the opposite end suffers a pressure gradient that drives the bubble/droplet displacement over the hydrophobic material. Figure 1.6 shows the micro-objects/particles manipulation driven by the microbubbles displacement induced by EWOD, i.e., micro-objects/particles are pushes and pulled by the microbubbles displacement[63].

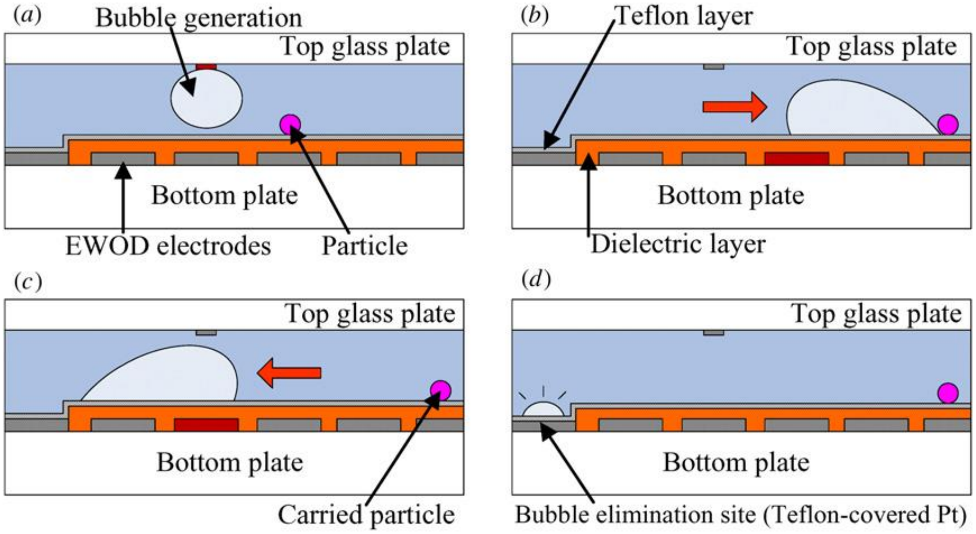

Fig. 1.6 Schematic of a bubble-based micro-object manipulator with three bubble operations: creation, transportation and elimination. (a) and (b) A bubble created from the top platinum electrodes by electrolysis can push a micro-object while being transported by EWOD. (c) and (d) If the bubble is not needed, it can be eliminated in the elimination site by a Pt-catalyzed electrochemical reaction. Note that the elimination Pt electrode is covered with a thin porous Teflon layer. Figure taken from Ref [63].

Thermal

It is based on the decrement of the liquid surface tension as a function of the temperature. According to Eötvös´ Law[64], the liquid surface tension σ decreases as the inverse of temperature T, $\sigma = {}^{1}\!/_{T}$. So a temperature gradient $\boldsymbol{\nabla T}$, generated by any mechanism, will produce a surface tension gradient $\boldsymbol{\nabla\sigma}$. A bubble immersed into a $\boldsymbol{\nabla\sigma}$ will suffer tangential stress on its wall driving the bubble displacement towards the lower surface tension[34,35,37,41], i.e., the bubble will be attracted towards the source of thermal gradient. Moreover, the bubble displacement occurs in opposite direction to the convective currents, in other words, the bubble is "swimming" against the liquid displacement. The phenomenon behind the bubble displacement by the $\boldsymbol{\nabla T}$ is called as the Marangoni effect $\boldsymbol{F_M}$, also known as thermocapillary effect.

This effect induces a force over the bubble given by[35,57]:

$$\boldsymbol{F_M} = -2\pi R^2 \boldsymbol{\nabla T} \, {}^{d\sigma}\!/_{dT}, \tag{1.4}$$

where R is the bubble radius and ${}^{d\sigma}\!/_{dT}$ is the temperature derivative of liquid surface tension.

Figure 1.7(a) shows a micro heater array fabricated on an N-type, single-side polished 〈100 oriented silicon wafer (4 inches in diameter and 500 µm in thickness). Figure 1.7(b) shows the horizontal microbubble displacement between micro heaters separated 23 µm. The thermal gradient is produced by a pulsed heating power of 103 mW[65].

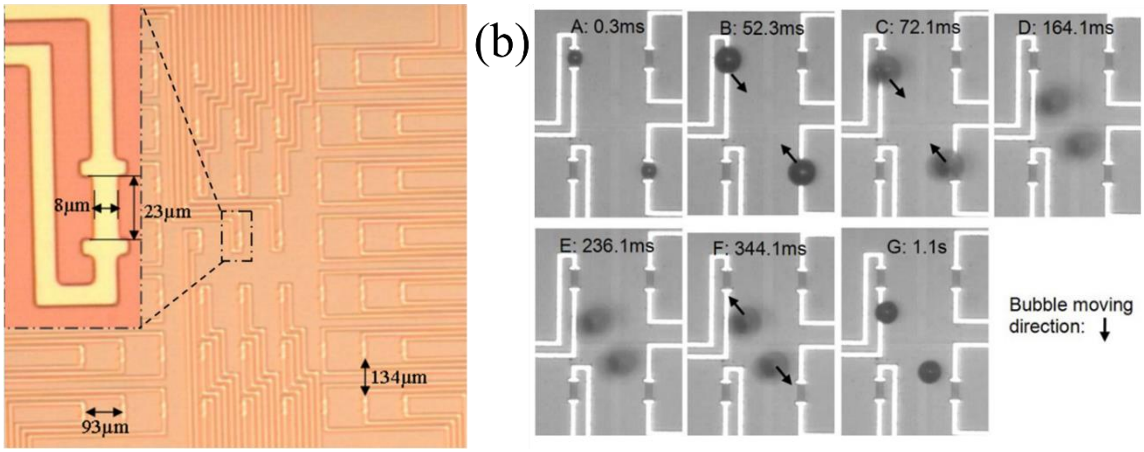

Fig. 1.7 Microbubble displacement induced by thermal gradients. (a) A photo taken during the fabrication process is shown in figure 2, where there are 63 heaters (7×9 array) on a single device chip. The dimensions of each heater are 8 × 23 µm² and the distances between heaters are 93 µm (in the horizontal direction) and 134 µm (in the vertical direction). To connect the heaters with the electrical circuits on a PCB (printed circuit board), a 0.4 µm thick Al film was coated and patterned to form the final metal leads. (b) Single thermal bubble departure and return driving by a pulsed heating power of 103 mW. Images taken from reference [65].

Electrocapillary

It is based on the application of an electric current over an electrolytic solution by electrodes[66]. The electric current induces an increment in the temperature of the electrolytic solution[67,68], i.e., a temperature gradient $\boldsymbol{\nabla T}$. This $\boldsymbol{\nabla T}$ induces the Marangoni force[34,35,41] over the bubble.

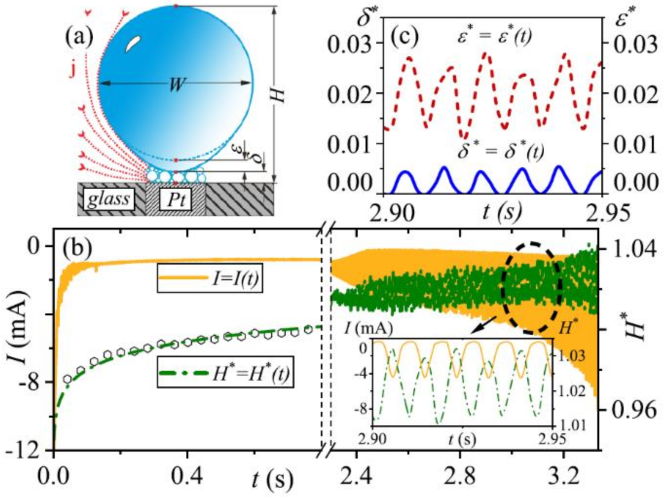

Fig. 1.8 Oscillating hydrogen bubbles by electrocapillary. (a) Scheme of the slightly deformed spherical bubble, sitting on the Pt electrode, and the carpet of microbubbles beneath, with their relevant geometric parameters. (b) Electric current I (solid line) and aspect ratio H of the bubbles versus time in 1 mol dm*$^{-3}$ *H_2SO_4 *at −5 V. Figure taken from reference*[66].

Hydrodynamic

Hydrodynamic mechanisms trapping lies in the use of hydrodynamic forces induces in low viscous aqueous solution within microfluidics devices. Typically, the microfluidics devices must have an obstruction or cavity for inducing a stagnation point flow. The fluid flow generated, which is a function of the geometry of the microfluidic device, drives the particles/bubbles to the confinement point[69,70].

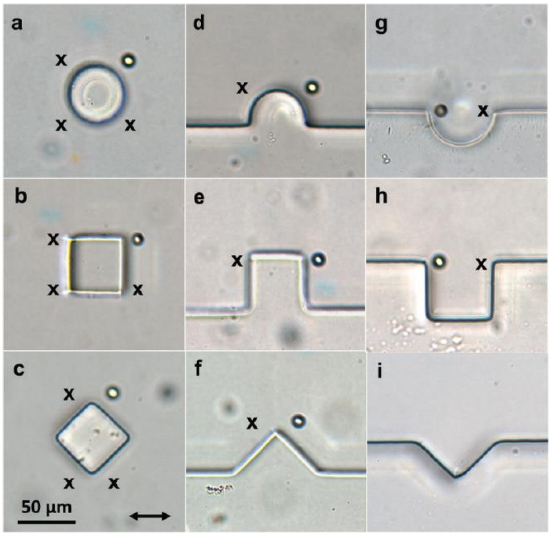

Fig. 1.9 Polystyrene microspheres (10 µm) trapped in steady streaming eddies generated by different geometries. All trapping was performed at very low particle densities, so we show an "×" to indicate symmetric, but unfilled, trapping locations. Image i displayed no stable trapping sites for the range of conditions used here. The arrow denotes fluid oscillation direction. Figure taken from reference [70].

Chemical

Chemical mechanisms are based on lowering the surface tension of the liquid by adding tensoactives, also called surfactants that means surface-active agents. Surfactants, usually organic compounds, are amphiphilic, i.e., formed by both a hydrophobic (water-hating) tail and a hydrophilic (water-loving) head. When there is enough amount of surfactant molecules in the liquid, individual surfactants molecules will aggregate to form a micelle. The hydrophobic tails form the core of the micelle, i.e., the tails are oriented inwards, whereas the hydrophilic heads are in contact with the surrounding liquid. The point at which micelles are formed is called critical micelle concentration. Because of the amphiphilic nature, surfactants molecules are absorbed in the gas-liquid or oil-liquid, and liquid-solid interface. The cohesive forces between the liquid molecules are so strong that the surface tension of the liquid is high. However, as the surfactants molecules are absorbed the surface tension of the liquid tends to decrease, i.e., the surfactants break the cohesive forces. Therefore, the intermolecular forces between the surfactants and the liquid molecules are much lower than two liquid molecules, driving the decrease of the liquid surface tension[71,72].

Magnetic

It is based on the application of a magnetic field over an electrolytic solution. The force induced by the magnetic field produces the movement of the electrolytic solution. So, bubbles inside the electrolytic solution will be dragged by the liquid movement[73,74]. Figure 1.10 shows the displacement of oxygen bubbles into an electrolytic solution[73].

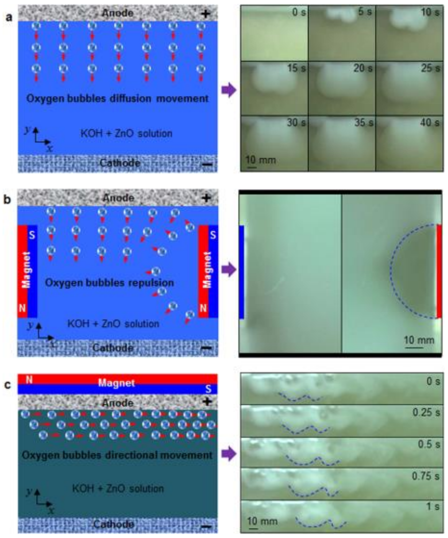

Fig. 1.10 Locomotion of oxygen bubbles in the upright elongated cell. (a) Oxygen bubbles movement perpendicular to the anode surface during oxygen evolution reaction without magnetic field. (b) Oxygen bubbles away from the magnet when the magnet N-pole perpendicular to the electrode. (c) Oxygen bubbles movement parallel to the anode surface during oxygen evolution reaction when the magnet S-pole faced with the anode. Figure taken from reference [73].

Optics

Optics mechanism is based on optical tweezers. Contrary to the dielectric or metallic particles, even biological matter, the refractive index of vapor bubbles is smaller than their surrounding medium (the refractive index of vapor or gas is < 1), so the light pushed the bubbles out of the high-intensity region of the laser beam. Nevertheless, several optics approaches have been proposed to trap and manipulate microbubbles such as using Laguerre-Gauss beams[44], also known as Bottle beams[75], by fast scanning Gaussian-based optical tweezers[76] that play a role as bottle beams and using ultrashort laser pulses at a high repetition rate. Despite these remarkable efforts, the optics mechanism is still limited to trap microbubbles with radii < 10 µm.

Figure 1.11 shows the optical trapping of microbubbles of 3.6 µm of radius (suspended in water) in inverted optical tweezers employing a fast-scanning Gaussian beam, i.e., a scanning ring-shaped trap.

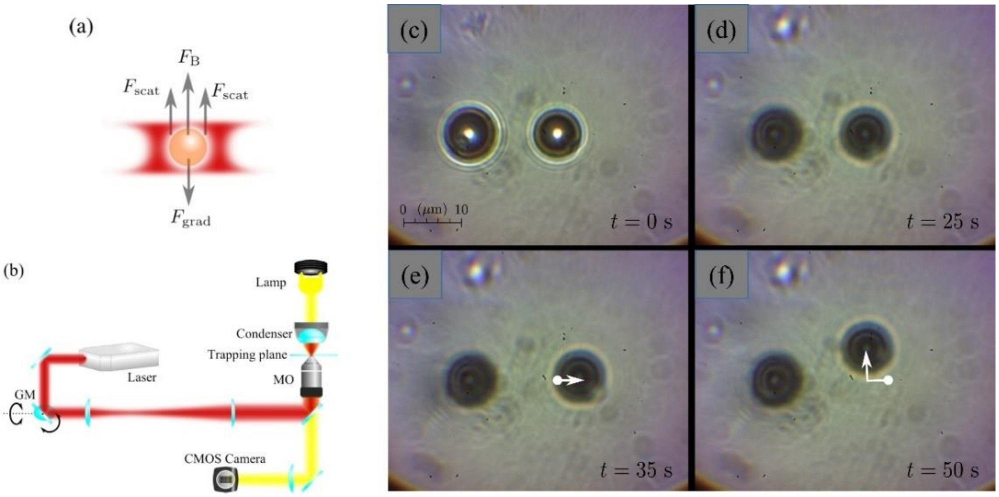

Fig. 1.11 Demonstration of three-dimensional optical trapping of a microbubble in the inverted scanning optical tweezers (a) Direction of forces on a microbubble in the inverted optical tweezers. (b) Experimental set-up for optical trapping of microbubbles. (c-f) Demonstration of microbubbles manipulation by optical trapping in the inverted scanning optical tweezers. Figure taken from reference[77].

Optothermal effects

Optothermal effects can be described as the set of thermodynamics and optics forces. The laser radiation incident on absorbing liquids (bulk absorption) or in metallic thin-film/suspended metallic particles immersed in water is absorbed by nonradioactive process, heat them up. In heated liquids, the density decreases setting up convective currents.

Specifically, in liquids, we may decompose the optothermal effects into its three main components:

a. *Thermal*: the thermal part plays a key role in optothermal effects because of triggers the phenomenon of thermophoresis (either positive or negative) and the Marangoni force.

b. *Hydrodynamic*: it produces convective currents that can exert a drag force over suspended particles on the liquid, besides, the upward buoyancy force is present.

c. *Optics*: it induces both the gradient and scattering force. i.e., optical tweezers.

Recently, optothermal effects generated in liquids have been proposed for both trapping and non-contact manipulation. Several experimental and theoretical works have extended the landscape of the optothermal effects applications. Particularity, our *Biophotonics Research Group* has proved the trapping and non-contact manipulation of microparticles at low CW-power[78], also the stacking of up to four polystyrene particles with one single focused beam at 3.5 mW of CW laser[79], besides, we have demonstrated the self-assembly of dielectric particles driven by optothermal effects without any surfactant[80].

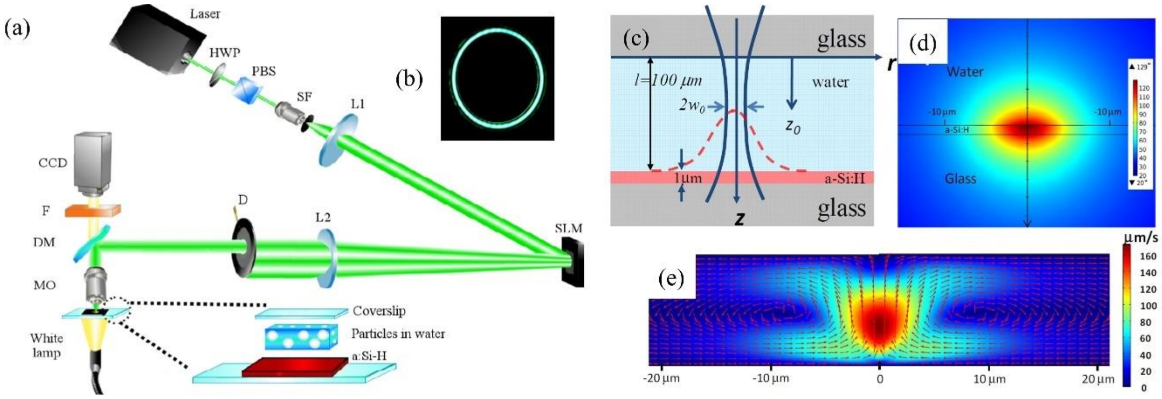

Fig. 1.12 Trapping and manipulation of microparticles by optothermal effects. (a) Optical set up. A 1W, 532 nm laser is focused onto a 1μm a-Si:H film. (b) Experimental image of the ring projected on the sample. (c) Schematic of the model. The z = 0 plane is placed at the glass-water interface and the beam waist is placed at a distance z0 = - 95 μm. (d) Temperature profile and (e) convective currents field obtained from COMSOL Multiphysics simulations. Figure taken from reference[78].

Application of the microbubbles

At the present, bubbles play a key role in many fields such as thermodynamics for heat transfer[53,81]; microfluidics for flow control[82], micromotors due to an oscillated bubble[83], boosting/driving fluids[84,85]; trapping and manipulation for trap and transport of organic matter (DNA)[86,87], and lithography[6], among others. In addition, we can be in touch with bubbles through biomedical devices like a needle-free injector for drug delivery[4,5], in lithotripsy[88,89], recently for liposuction, and ultrasonic imaging[1,3].

Thesis structure

This thesis work explores the performance of the optothermal effects induced by laser radiation as a 3D trapping and manipulation mechanism for low index refractive particles, i.e., vapor bubbles, mainly focused on the Marangoni force. Each chapter can be outlined as follows:

Chapter 2

In this chapter, a brief description of the phase changes in liquids, nucleation theory, and the generation of vapor microbubbles is presented. In addition, we are going to discuss about the superheated liquids and thermodynamics parameters under which the superheated state is present. Then, the dynamics involved in the vapor bubble trapping and its manipulation is presented. Finally, the dynamics of spherical bubble collapse are presented.

Chapter 3

In this chapter, we are going to discuss about the dynamics behind the trapping and manipulation of vapor microbubbles, i.e., optothermal effects are decomposed in their main components for understanding the role of each one and how they are interconnected. A brief description of the forces involved (surface tension, cohesive forces, Stokes law, buoyancy force, optical forces, Marangoni force, and inertia force) is presented. After that, we are going to discuss the performance of the optical forces over vapor microbubbles.

Chapter 4

In this chapter, we present the generation and manipulation of microbubbles by means of temperature gradients induced by low power laser radiation. A laser beam (λ = 1064 nm) is divided into two equal parts and coupled to two multimode optical fibers. The opposite ends of each fiber are aligned and separated a distance D within an ethanol solution. Previously, silver nanoparticles were photo deposited on the optical fibers ends. Light absorption at the nanoparticles produces a thermal gradient capable of generating a microbubble at the optical fibers end in non-absorbent liquids. The theoretical and experimental studies carried out showed that by switching the thermal gradients, it is possible to generate forces in opposite directions, causing the migration of microbubbles from one fiber optic tip to another. Marangoni force induced by surface tension gradients in the bubble wall is the driving force behind the manipulation of microbubbles. We estimated a maximum Marangoni force of 400 nN for a microbubble with a radius of 110 μm.

Chapter 5

The most common approach to optically generate and manipulate bubbles in liquids involves temperature gradients induced by CW lasers. In this thesis, we present a method to accomplish both the generation of microbubbles and their 3D manipulation in ethanol through optothermal forces. These forces are triggered by light absorption from a nanosecond pulsed laser (λ = 532 nm) at silver nanoparticles photodeposited at the distal end of a multimode optical fiber. Light absorbed from each laser pulse quickly heats up the silver-ethanol interface beyond the ethanol critical-point (~ 243 °C) before the heat diffuses through the liquid. Therefore, the liquid achieves a metastable state and owing to spontaneous nucleation converted to a vapor bubble attached to the optical fiber. The bubble grows with semi-spherical shape producing a counterjet in the final stage of the collapse. This jet reaches the hot nanoparticles vaporizing almost immediately and ejecting a microbubble. This microbubble-generation mechanism takes place with every laser pulse (10 kHz repetition rate) leading to the generation of a microbubbles stream. The microbubbles' velocities decrease as they move away from the optical fiber and eventually coalesce forming a larger bubble. The larger bubble is attracted to the optical fiber by the Marangoni force once it reaches a critical size while being continuously fed with each bubble of the microbubbles stream. The balance of the optothermal forces owing to the laser-pulse drives the 3D manipulation of the main bubble. A complete characterization of the trapping conditions is provided in this chapter.

Chapter 6

In this chapter, we present an experimental and theoretical study on the 3D trapping and manipulation of microbubbles by means low power laser-induced temperature gradients induced in ethanol by bulk light absorption (λ = 1550 nm). Two optical fibers were used: One for bubble generation (OF_G) and the other for both trapping and manipulation (OF_T). Light from a Q-switched pulsed laser (λ = 532 nm and pulse width τ_p = 5 ns) propagates in fiber OF_G and gets absorbed at silver nanoparticles (AgNPs), previously photodeposited, at the distal end of a fiber optic core, generating the microbubbles. In the fiber OF_T, light of low power CW laser was used to trap and manipulate the bubbles by thermocapillary induced by light bulk absorption in ethanol. The microbubble generated on OF_G migrates toward the fiber OF_T. The equilibrium between the buoyancy force $\boldsymbol{Fb}$, drag force $\boldsymbol{F_d}$ and the Marangoni force (also known as thermocapillary force) $\boldsymbol{F_M}$ gives rise to a 3D stably trapping and manipulation of the microbubble for the best time to our best knowledge.

Chapter 7

In this chapter, we show 3D steady-state trapping and manipulation of vapor bubbles in liquids employing a low power continuous-wave laser using the Marangoni effect. Light absorption from photodeposited silver nanoparticles on the distal end of a multi-mode optical fiber is used to produce bubbles of different diameters. The thermal effects produced by either the nanoparticles on the fiber tip or the light bulk absorption modulate the surface tension of the bubble wall and creates both longitudinal and transversal forces just like optical forces, effectively creating a 3D potential well. Using numerical simulations, we obtain expressions for the temperature profiles and present analytical expressions for the Marangoni force. In addition, using an array of three fibers with photodeposited nanoparticles is used to demonstrate the transfer of bubbles from one fiber to another by sequentially switching on and off the lasers.

Chapter 8

In this chapter, we present both the general conclusion and the futures avenues of this research.

Chapter 9

Finally, we present the academic production development throughout the P.h.D, i.e., list of publications and proceedings.

Chapter 2. Phase changes and nucleation

In this section, we will to discuss about the thermodynamics phases changes that lead to bubble generation and the temperatures at which they occurs under continuous radiation and pulsed radiation. Besides, we will emphasize the differences between continuous and pulsed radiation. Finally, we are going to examine the dynamics of spherical bubble collapse near a solid wall.

Phase changes in liquids

According to Oxtoby[90], we can define *nucleation* as the first-order phase transition. In this change of phase, the molecules of the liquid have enough kinetic energy to surpass intermolecular forces. Particularly, the phase change from liquid to vapor is called *boiling* and occurs when the temperature is increased over the saturated liquid/vapor temperature[54]. In addition to boiling, *cavitation* is another mechanism to induce phase change from liquid to vapor[91]. Cavitation, can be achieved by either isothermal conditions by reducing the pressure below the vapor pressure or isobaric conditions by increasing the temperature up to the spinodal limit[91–93].

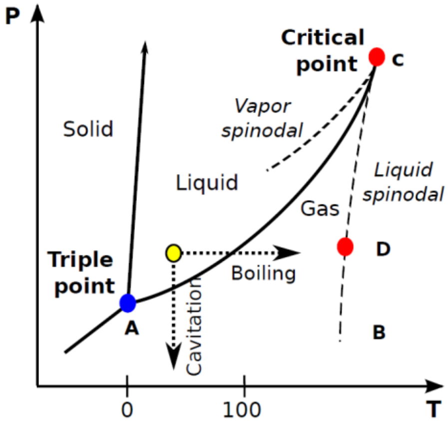

Fig. 2.1 Phase diagram of water (pressure P versus Temperature T). The yellow dot represents the ambient pressure at room temperature, whereas the arrows indicate the paths to induce either boiling or cavitation[91,92].

Figure 2.1 shows the phase diagram of water pressure P versus temperature T). The triple point, indicated by the blue dot and marked by the letter **A**, represents the point at which the solid, liquid, and vapor phases coexist (T = 0.01 °C and P = 611.65 Pa). As we can infer, at this point one can obtain ice, liquid, and vapor of water by making small and random changes in pressure and temperature. The line **AC**, called binodal, represents the separation limit between liquid and vapor phases, i.e., is the saturated liquid/vapor line. The vapor spinodal line represents the threshold at which metastable vapor can be subcooled. On the other hand, the liquid spinodal line indicates the threshold at which metastable liquid can be superheated. Point **D** represents the equilibrium point at which both the vapor pressure and specific volume for saturated liquid correspond to the spinodal temperature (T = 305 °C and P = 9.2 MPa). It is at this point that the cavitation process begins[91–93].

As it was pointed out above, there are two mechanisms to induce phase change from liquid to vapor; boiling and cavitation. Even though both mechanisms seem to be similar for bubbles generation, they emerge from a different thermodynamic paths. The former nucleation mechanism, boiling, lies on the increment of the liquid temperature up to the saturated vapor/liquid temperature, whereas cavitation is triggered by the falls below the vapor pressure[92]. Moreover, boiling is a process much slower than cavitation.

The nucleation process can be divided into two categories, homogeneous and heterogeneous nucleation[90]. In the former, the inherent thermal fluctuations present in the liquid can produce microscopic voids, i.e., temporary voids formed the nucleation spots required for the generation of macroscopic bubbles[93,94]. In the latter one, heterogeneous nucleation, the nucleation spots are impurities or little voids on the container´s wall. Therefore, heterogeneous nucleation is more common than homogenous one because it is hard to avoid impurities on the liquid or voids in the walls of the liquid cell[93,94].

Commonly there are imperfections in the container or impurities present in the liquid that act as nucleation points around which a bubble can begin to form. Nevertheless, under specific conditions: a perfectly smooth container and liquid without stirring, it is possible to superheat the liquid above its boiling point. This superheated liquid may undergo an e*xplosive phase transition* and occurs near the spinodal temperature (305 °C for water)[10,93,94], i.e., producing a fast-expanding bubble.

Nucleation theory

Nucleation theory addresses the generation of bubbles in thermodynamics equilibrium within a liquid (see Fig. 2.2). The interior pressure of the bubbles can be related to the pressure of the surrounding liquid by surface tension. Surface tension plays a major role in the bubbles generation because it represents the macroscopic manifestation of the intermolecular forces that tend to hold the molecules together and prevent the creation of large holes/voids.

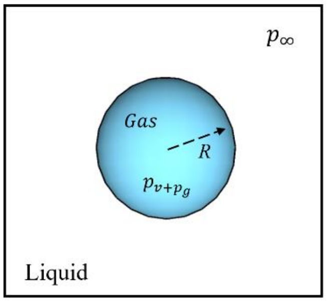

Fig. 2.2 Spherical vapor bubble of radius R in an equilibrium within a liquid. p_∞ *represents the pressure of the surrounding liquid,* p_v *is the vapor pressure, and* p_g *is the partial pressure of the gas within the bubble.*

The pressure, p, exerted over the bubble of radius R, will be related to the interior pressure in the bubble, p_B, by:

$$p_B = \frac{2S}{R}, \tag{2.1}$$

where S is the surface tension. If the temperature, T, is uniform and the bubble contain only vapor, the bubble interior pressure will be the saturated vapor pressure $p_{sat}(T)$. Nevertheless, in order to produce equilibrium conditions, the exterior liquid pressure $p = p_{sat} - 2S/R$ will have to be less than p_{sat}. Subsequently, if the exterior liquid pressure is maintained at a constant value just slightly less than $p_{sat} - 2S/R$, the bubble will grow, thus R will increase, the excess pressure causing growth will increase, and rupture will take place[57]. It follows that if the maximum size of the vacancy present is R_c (termed the critical radius or cluster radius), then the tensile strength of the liquid, Δp_c, will be given by:

$$\Delta p_c = \frac{2S}{R_c}. \tag{2.2}$$

On the other hand, considering a superheated liquid at a constant pressure, p, at a temperature, T, above the boiling temperature, T_b, or, equivalently, at a constant temperature, T, at a pressure below the saturation pressure, $p_{sat}(T)$, the minimum work required to induce a vapor bubble of radius R_c within the liquid is given by:

$$W_c = 4\pi R_c^2 S - \frac{4}{3}\pi R_c^3 \Delta P_c, \tag{2.3}$$

where W_c indicates the energy that must be deposited in order to form the critical size bubble. As we noted, W_c expressions consist of two terms, the former means both the energy that must be deposited and stored in the bubble surface. The latter represents the liquid amount that was displaced outward to create the bubble, therefore, this implies work done on or by the system.

The difference of the pressure involved in this energy increment is the difference between the inner pressure and the outer pressure of the bubble. Thus, the work done by the system is the volume of the bubbles times the pressure difference, ΔP_c. So, the critical deposited energy required becomes:

$$W_c = 4\pi R_c^2 S = \frac{16}{3}\frac{\pi S^3}{\Delta p_c^2}. \tag{2.4}$$

Most of the homogenous nucleation theory relate W_c to the typical kinetic energy of the molecules, called kT (where k is the Boltzmann´s constant) and the relationship is expressed in terms of the Gibbs number, G_b, given by:

$$G_b = \frac{W_c}{kT}. \tag{2.5}$$

Nucleation theory offer us information about the nucleation of critical bubbles under ideal conditions, i.e., steady-state nucleation. However, several expressions have been proposed for the precise form of the relationship between the nucleation rate, J, and the Gibbs number. Nucleation rate represents the number of nucleation events appearing in a unit volume per unit time, it is given by:

$$J = N\left(\frac{2S}{\pi m}\right)^2 exp\left[-\frac{16\pi}{3}\frac{S^3}{\Delta \mathrm{P}_c^2 kT}\right], \tag{2.6}$$

$$J = J_0 exp[-G_b], \tag{2.7}$$

where N represents the number density of the liquid (molecules/m^3), and m indicates the mass of the molecule, and J_0 is a proportionally factor. Therefore, nucleation rates is proportional to $exp[-G_b]$; it will be likely when E_c becomes comparable to the thermal fluctuations. Even though the nucleation theory predicts the superheat limit of liquids, does not provide any information concerning the intensity of evaporation at the limit. Deeply studies have shown that the cavitation probability reaches ½ when:

$$\frac{W_c}{kT} = ln\left(\frac{\Gamma_0 V\tau}{ln2}\right), \tag{2.8}$$

where Γ_0 represents a kinetic prefactor that can be estimated by the thermal frequency ${}^{kT}/_{h}$ times the density of independent nucleation sites ${}^{1}/_{R_c^3}$, V and τ indicates the volume and duration of the experiment, respectively. Specifically, water is a strongly cohesive liquid due to hydrogen bonding between its molecules. It drives to the water surface tension S to be unusually high, allowing a high degree of metastability, at least theoretically.

Superheated liquid

As we pointed out in previous sections, liquids can be heated beyond its boiling points and beyond, this condition is known as superheated of liquid.

Laser heating

Shortly after the invention of the laser, light-induced cavitation was demonstrated which is a powerful tool that has gained relevance with the advancement of technology[95,96]. Light-induced cavitation plasma formation, generally indicated by a visible flash or spark in the medium is based on the process of liquid breakdown[97]. However, the mechanism that triggers liquid breakdown depends on the features of the radiation source employed, i.e., laser pulse duration, pulse intensity, wavelength, polarization, among others. Focusing on laser pulse duration; an ultrashort-pulsed laser (100 fs $< \tau <$ 1 ns) induces what is known as the optical breakdown, whereas a continuum laser or even short-pulsed laser ($\tau >$ 1 ns) generates the process called laser-induced thermal breakdown[98].

The optical breakdown is a nonlinear absorption process that ionizes the incident media, usually in nominally transparent liquids, leading to plasma formation. This process demands high energy densities to reach the liquid breakdown threshold I_{th}[97]. Plasma formation takes place in distilled water at irradiances $I_{th} > 10^{10}$ W/cm^2 [97]. There are two mechanisms of optical breakdown: avalanche ionization *AI*, also known as cascade ionization *CI*, and multiphoton ionization *MPI*[99]. Both ionization mechanisms must exceed the critical density of ionized electrons, ρ_{cr}, during the laser pulse[100]. On one hand, *AI* requires a few seed electrons, also known as free electrons or lucky electrons. These seed electrons, which are already present in the focal volume before the arrival of the laser pulse, are accelerated by the laser electric field. The increased kinetic energy of the electrons is transferred to the atoms/molecules through collision and realizing more electrons. These seed electrons can be produced either by the *MPI* process itself or by the heating of linearly absorbing impurities present in the liquid. Besides, the impurities heating can decrease the optical breakdown threshold. On the other hand, *MPI* does not require these seed electrons, however, *MPI* does both require a pure liquid and demands higher energies. The *MPI* rate is proportional to I^k, where k is the number of photons needed to achieve the ionization potential ($\bar{\Delta}$), i.e, the photons required to cross the bandgap. The *AI* mechanism rate is proportional to the incident irradiance. Due to the *MPI* mechanism rate is highly depends on irradiance; the *MPI* process becomes more relevant as the duration of the laser pulse decreases[101]. Therefore, the interplay between *AI* and *MPI* has been elucidated as the cornerstone for optical breakdown.

On the other hand, the laser-induced thermal breakdown is a linear absorption process that induces thermal effects by either CW or long-pulsed laser, also called thermocavitation[102,103]. This process entered the cavitation world through the pioneering work of Rastopov and Sukhodolsky earlier 1990[102,104]. The laser radiation is focused on absorbing liquids. The absorbed light quickly heats the liquid up beyond its thermodynamic critical temperature T_C (spinodal limit) at a time from µs to ms, i.e., $T_{C\,water} \sim 647\ K$[105]. As the liquid temperature reaches its spinodal limit, the liquid enters into a metastable state. Therefore, the superheated liquid turns unstable to random density fluctuations and the liquid undergoes an explosive phase transition to vapor. A fast-expanding vapor bubble is generated, whose radius goes from the sub-millimeter range up to 5 millimeters[106]. However, as Padilla *et al.*[105] and Ramirez-San-Juan *et al.*[106] reported, the shockwave amplitude of thermocavitationally-induced bubbles is, at least, 3 orders of magnitude smaller than the shockwave produce by the optical breakdown. In fact, thermocavitation process exhibits an input energy conversion of around 20 % into mechanical energy[105], contrary to the optical breakdown, where close to 10 – 30 % of the input energy is lost[107]. Nevertheless, thermocavitation can be induced at an irradiance threshold around $I_{th} \approx 10^3$ W/cm^2, i.e., at least 7 orders of magnitude less than optical breakdown[44,105]. Moreover, this I_{th} can be lowered by matching/tunning the wavelength used with the liquid absorption coefficient, i.e., maximizing the input energy absorption.

Besides, one remarkable feature concerning thermocavitation is the fact that the bubble induced with the lowest optical power generates the largest radius, therefore, the highest pressure shock waves[106]. It is supported by the fact that usually the thermal diffusion time τ_{dif} for absorbing liquids is less than the cavitation time τ_{cav}, i.e., $\tau_{dif} \ll \tau_{cav}$. So, more liquid is ready to be evaporated because the heat generated can be transferred to a larger volume, consequently, larger bubbles are generated. Moreover, thermocavitation exhibits the advantage of inexpensive energy sources.

Boiling crisis

Boiling crisis is described by a very large rate of heat transfer from the heating interface to the fluid bulk. If the heating energy is increased, the temperature of the heating interface boosts with the heat flux. If the heat flux from the heating source achieves a threshold value, the vapor bubbles generated suddenly will turns into vapor films. This films will cover the heating surfaces, playing as a insulate mechanism, so the bulk fluid will be isolate from the heating source[108,109].

Figure 2.3, taken from Cengel[110], shows different boiling regimes in pool boiling for water.

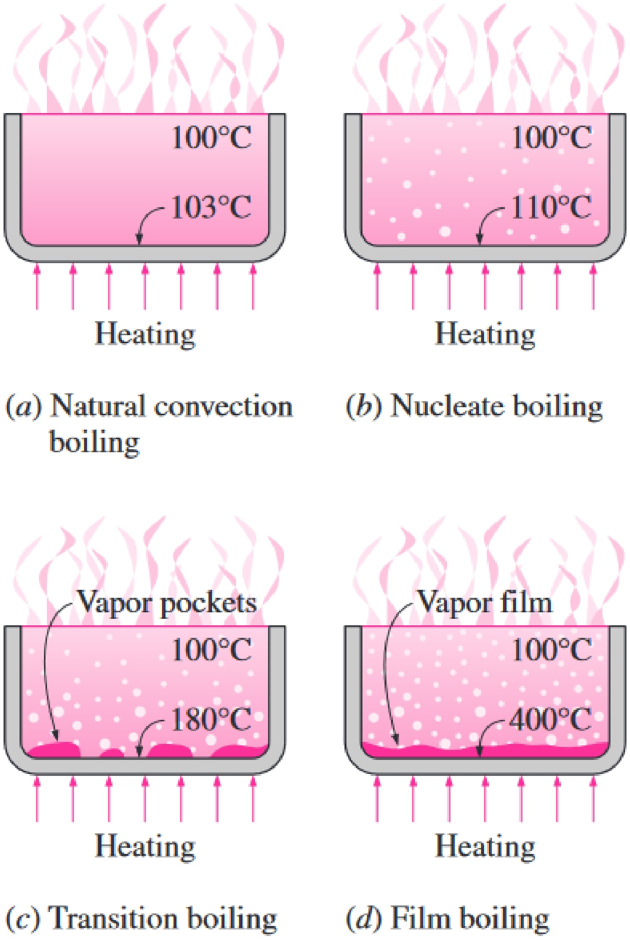

Fig. 2.3 Different boiling regimes in pool boiling for water. (a) Natural convection boiling. (b) Nucleate boiling. (c) Transition boiling. (d) Film boiling, also called boiling crisis[110]*.*

Dynamics of spherical bubbles

In this section, we are going to discuss the dynamic of spherical bubbles focusing on their collapse: spherical and non-spherical collapse.

Bubble collapse

Once the nucleation theory was mentioned, it is time to focus on the bubble dynamics, i.e., bubble growth and its collapse. In addition, we are discussing the differences between the symmetric and asymmetric bubble collapse, i.e., when the bubble is far away from an interface/wall and when the bubble is near or attached to a wall/solid boundary.

Rayleigh-Plesset equation

The simple case, asymmetric spherical bubble, is useful to derive the Rayleigh-Plesset equation that governs the spherical bubble dynamic in a liquid infinite body. This equation is going to be derived under the following assumption (the simplest conditions):

a. The bubble is present in an infinite incompressible liquid that is either Newtonian or inviscid.

b. The bubble remains spherical at all times.

c. The liquid density surrounding the bubble is greater than the gas density of the bubble.

d. The gravitational force will not take into account.

e. The gas content is constant.

These assumptions are taken only as a first approximation, in real life both the exchange of energy and the mass transfer between the bubble and its surrounding liquid are present. Here, we will determine the functions of velocity $u(r,t)$ and the pressure $p(r,t)$ in the liquid domain $r \geq R(t)$. The equation of the mass conservation for an incompressible liquid is given by[93]:

$$u(r,t) = \dot{R}\frac{R^2}{r^2}. \tag{2.9}$$

The viscous term of the Navier-Stokes equation is zero just in this simple and particular case. Therefore, for both a vicious and non-viscous liquid, the equation of momentum is given by:

$$\frac{\partial u}{\partial t} + u\frac{\partial u}{\partial r} = -\frac{1}{\rho}\frac{\partial p}{\partial r}, \tag{2.10}$$

Taking equation 2.9 into account, one can infer:

$$\ddot{R}\frac{R^2}{r^2} + 2\dot{R}^2\left[\frac{R}{r^2} - \frac{R^4}{r^5}\right] = -\frac{1}{\rho}\frac{\partial p}{\partial r}. \tag{2.11}$$

Integrating for r and contemplating the pressure conditions at infinity, $p_\infty(t)$, one obtains:

$$\ddot{R}\frac{R^2}{r} + 2\dot{R}^2\left[\frac{R}{r} - \frac{R^4}{4r^4}\right] = \frac{p(r,t) - p_\infty(t)}{\rho}. \tag{2.12}$$

Equation 2.12 is equivalent to the Bernoulli equation for a variable unsteady flow of non-viscous liquid. At the bubble wall, i.e., $r = R$, Eq. 2.12 turns into:

$$\frac{p(R,t) - p_\infty(t)}{\rho} = R\ddot{R} + \frac{3}{2}\dot{R}^2. \tag{2.13}$$

Considering that the pressure of the bubble interface is given by:

$$p(r,t) = p_b + p_i\left(\frac{R_0}{R}\right)^{3\gamma} - \frac{2S}{2R} + 2\mu\frac{\partial u}{\partial r}|_{r=R}, \tag{2.14}$$

where p_i is the initial pressure, γ represents the ratio of heat gas capacities, μ is the kinematic viscosity. Considering $\frac{\partial u}{\partial r}|_{r=R} = -\frac{2\dot{R}}{R}$, Eq. 2.13 turns into the following equation:

$$\rho\left[R\ddot{R} + \frac{3}{2}\dot{R}^2\right] = p_b + p_\infty(t) + p_i\left(\frac{R_0}{R}\right)^{3\gamma} - \frac{2S}{R} - 4\mu\frac{\dot{R}}{R} \tag{2.15}$$

This expression, called the Rayleigh-Plesset equation, lets us estimate both the temporal evolution of a bubble of radius R and the pressure field surrounding the bubble when the law $p(t)$ is given, i.e., liquid pressure.

Considering the ideal case, a bubble containing just vapor without condensable gases, a non-viscous liquid ($\mu = 0$) and neglecting the surface tension ($S = 0$), Eq. 2.15 becomes:

$$\dot{R} = -\sqrt{\frac{2}{3}\left[\frac{p_\infty - p_b}{\rho}\right]\left[\frac{R_0^3}{R^0} - 1\right]}. \tag{2.16}$$

This expression determines the bubble interface velocity, $(\dot{R})$, at the bubble collapse. As we can infer, bubble collapse requires an external pressure greater than the bubble inside pressure, i.e., $p_\infty > p_b$. The interface velocity is negative $(\dot{R} < 0)$ and the initial radius is greater than the bubble radius, i.e., $R_0 > R$ at any moment.

The bubble collapse time, also known as the Rayleigh time is given by:

$$\tau_c \approx 0.915\sqrt{\frac{\rho}{p_\infty - p_b}}R_0, \tag{2.17}$$

where R_0 is the maximum radius before the collapse and p_v is the vapor pressure (bubble pressure).

Bubble collapse near a solid wall

The presence of a solid wall at the spherical bubble collapse disrupts the symmetric collapse, i.e., the solid wall near the bubble will induce an asymmetric bubble collapse. Besides, the presence of a solid wall near the bubble can induce changes in the bubble morphology, i.e., bubble not completely spherical. In the last decades, the dynamics of a bubble near or attached to a solid surface (or interface) have been studied by both high-speed photography and acoustic means. It is well known that the asymmetric bubble collapse will produce a counter jet explained by the non-spherical bubble collapse theory developed by Rattray in his Ph.D. thesis[111–113]. Before the collapse, the semi-spherical bubble takes a toroidal shape due to the formation of a counter jet directed towards the wall/interface. This counter jet is capable to penetrates the bubble, hitting the wall/interface. In the case of heated walls/substrates, the counter jet is immediately vaporized after hit the substrate, producing a secondary bubble.

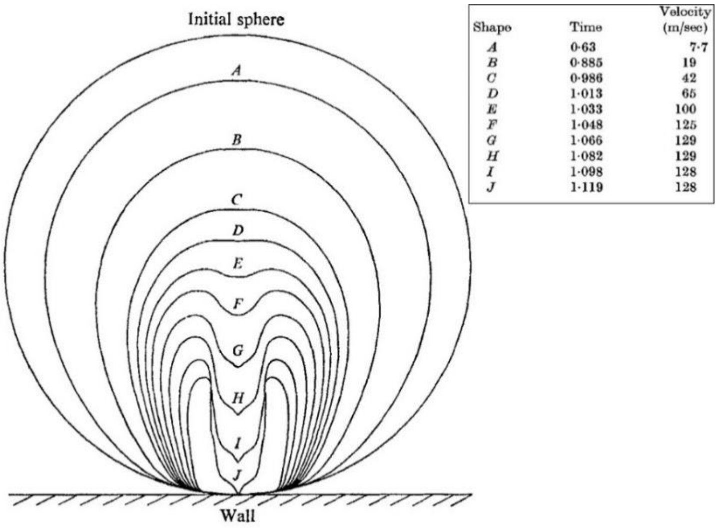

Shape	Time	Velocity (m/sec)
A	0·63	7·7
B	0·885	19
C	0·986	42
D	1·013	65
E	1·033	100
F	1·048	125
G	1·066	129
H	1·082	129
I	1·098	128
J	1·119	128

Fig. 2.4 Non-spherical bubble collapse at $\gamma = 1$. Figure taken from reference[112].

The bubble life time, τ_r, near a solid wall is given by:

$$\tau_r \approx \tau_c \, (1 + 0.205\gamma) \tag{2.18}$$

where $\gamma = {}^{H}\!/_{R_0}$ is the standoff parameter, H represents the distance between the wall and the center of the bubble , and τ_c is the collapse time for a spherical bubble (see Eq. 2.17).

Figure 2.4 shows a numerical simulation concerning collapse of a bubble near a solid wall/interface developed by Plesset and Chapman[112], i.e., non-spherical bubble collapse. As the bubble collapse progresses, the penetration velocity of the counter jet is greater, as we can notice in the inset of Fig. 2.4 Once the counter jet is formed, the speed of its tip remains fairly constant[112].

Chapter 3. Dynamics of the trapping and 3D manipulation of microbubbles

In this section, we will to discuss the environment of conditions and forces that are present in both trapping and manipulation of vapor microbubbles i.e., optothermal effects. A brief description of the forces involved is presented. After that, we will to discuss the performance of the optical forces over vapor microbubbles.

Surface tension

We can define the surface tension as a property of the liquid surfaces that allows them to resist external forces over them. Surface tension force is a vector that exhibits a tangential direction to the free surface of the liquid and is driven by cohesive forces. Moreover, surface tension is driven by the inhomogeneous force over each liquid molecule at the liquid interface. At this liquid interface, the net force is directed towards the interior of the liquid, simulating an elastic film, as is shown in Fig. 3.1.

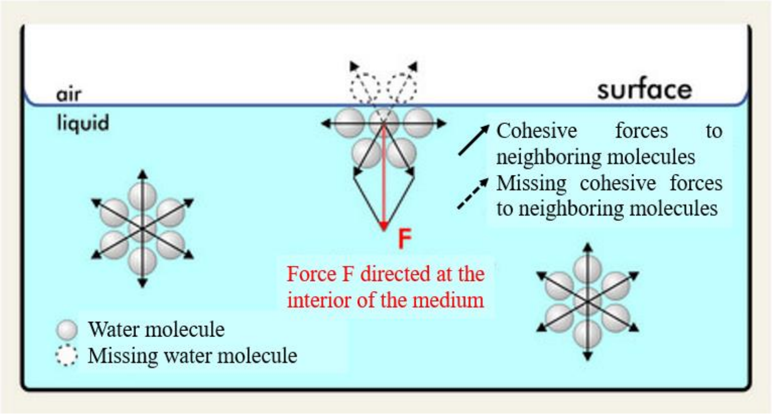

Fig. 3.1 Sketch of the cohesive forces between liquid molecules.

Cohesive forces

Cohesion is the intermolecular attractive force acting among adjacent molecules of the same substance; allowing matter to be together. The physical properties of melting point, boiling point, vapor pressure, evaporation, density, viscosity, surface tension, and solubility are dependent on the cohesive force.

Cohesive forces are divided into:

a. *Coulomb force*: It emerges from the electrostatic force that holds the ions together, i.e., opposite charges attract each other. Coulomb force is the strongest intermolecular force.

b. *Hydrogen bond*: It is the attractive force between the hydrogen atom attached to an electronegative one (usually nitrogen, oxygen, and fluorine) of one molecule and an electronegative of a different molecule.

c. *Dipole force*: Polar covalent molecules are something described as "dipoles", meaning that the molecules have two poles.

d. *Dipole-dipole interactions*: When a polar molecule encounters another polar molecule, the positive end of the molecule is attracted to the negative end of the other polar molecule.

e. *Ion-dipole interaction*: It emerges from the interaction between an ion and a polar molecule.

The term Van der Waals forces emerge as the result of the sum of the cohesive forces. So Van der Waals forces is an attractive force. On the other hand, electrostatic force, also known as Coulomb force, can be both attractive or repulsive force. Generally, electrostatic force is a repulsive force and operates closer to the particle than the Van der Waals force, as is illustrated in Fig. 3.2.

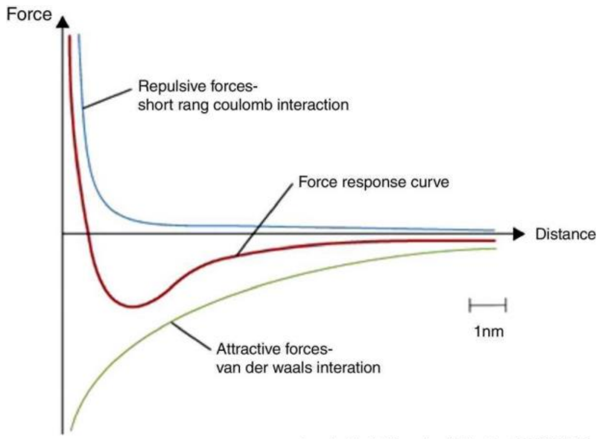

Journal of Applied Research and Technology 2016;14:375–82

Fig. 3.2 Operation range of intermolecular forces. Repulsive forces are the ones that operate closest to the particle.

Stokes law

A body, immersed in a fluid in movement, will be exposed to forces induced by the action of the fluid itself, i.e., the body will be dragged by the fluid. This drag force, also known as Stokes law, F_d, is exerted by the fluid in opposite direction to the force exerted by the body in movement. Drag force is given by[11,114]:

$$\boldsymbol{F_d} = -6\pi\mu R\boldsymbol{u}, \tag{3.1}$$

where μ represents the dynamic viscosity of fluid and $\boldsymbol{u}$ is the velocity of the body (particle, bubble). The negative sign indicates that the displacement velocity of the body is contrary to the convective currents.

Buoyancy force

A body immersed in a fluid is subjected to the gravitational pull that is given by the principle of Archimedes[11]:

$$\boldsymbol{F_b} = \frac{4}{3}\mu R^3\boldsymbol{g}(\rho_l - \rho_v), \tag{3.2}$$

where $\boldsymbol{g}$ represents the gravitational acceleration, ρ_l and ρ_v are the density of the liquid and the vapor of the fluid, respectively.

Optical forces

Light pressure was initially suggested by Johannes Kepler in his explanation of comets' tails. However, light pressure was correctly explained by the theory of electromagnetism of James Clerk Maxwell[115]. It was up to Arthur Ashkin[7] that light pressure was successfully demonstrated by experimentally showing dielectric particle levitation (trapping) by slightly focusing a Gaussian laser beam (TEM $_{00}$). A. Ashkin reported that the dielectric particles, semitransparent to the wavelength used, were attracted to the beam center and accelerated in the direction of the beam propagation axis. A. Ashkin explained the behavior of these particles by employing rays optics to describe the particles´ interaction with the incident light[22], as is depicted in Fig. 3.3.

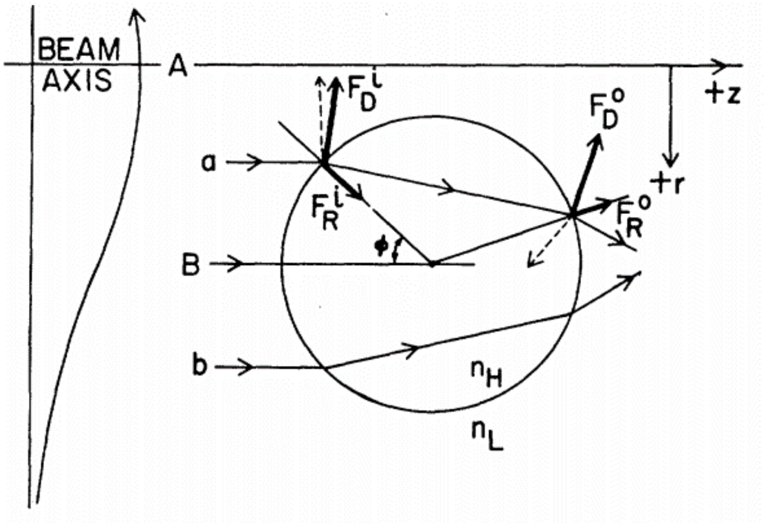

Fig. 3.3 Optical forces on a dielectric particle. Figure taken from reference[7].

Considering a dielectric particle with refractive index n_H immersed in water, with refractive index $n_L = 1.33$, such as $n_H > n_L$, and taking two light rays. The ray (a), is closest to the beam center, i.e., the most intense ray, while the ray (b), is the farthest ray to the beam center. These rays enter and exit the dielectric particle, this particle-light interaction induces changes in the pathway of the light, i.e., reflection and refraction. As a result, inner (F_R^I) and outer reflection force (F_R^O) takes place. In addition, inner (F_D^I) and outer (F_D^I) deflection forces are present. The axial components of these forces, for both rays, are canceled, so the result net force points in $+z$ direction, inducing particle movement. A Ashkin, motivated by the discovery of particle movement driven by light pressure, Ashkin delved into the optical manipulation by means of two opposing identical laser beams, i.e., particle trapping by a stable optical potential well, called optical tweezers.

Optical tweezers are a wonderful tool for both trapping and manipulate particles. It is usual to theoretically split the optical forces as:

$$\boldsymbol{F} = \boldsymbol{F_g} + \boldsymbol{F_s}, \qquad (3.3)$$

where $\boldsymbol{F_g}$ is the conservative force, called gradient force and $\boldsymbol{F_s}$ is the non-conservative force that involves the scattering and absorption force.

Gradient force

Gradient force, F_g, according to electric dipole approximation is proportional to the intensity of the laser beam employed, and is given by[116]:

$$\boldsymbol{F_g} = \frac{1}{2}\alpha'(\omega)\nabla \boldsymbol{E}^2, \tag{3.4}$$

where $\alpha(\omega) = \alpha'(\omega) + \alpha''(\omega)$ is the particle complex polarizability. Gradient force is linearly dependent on the real component of the polarizability, $\alpha'(\omega)$.

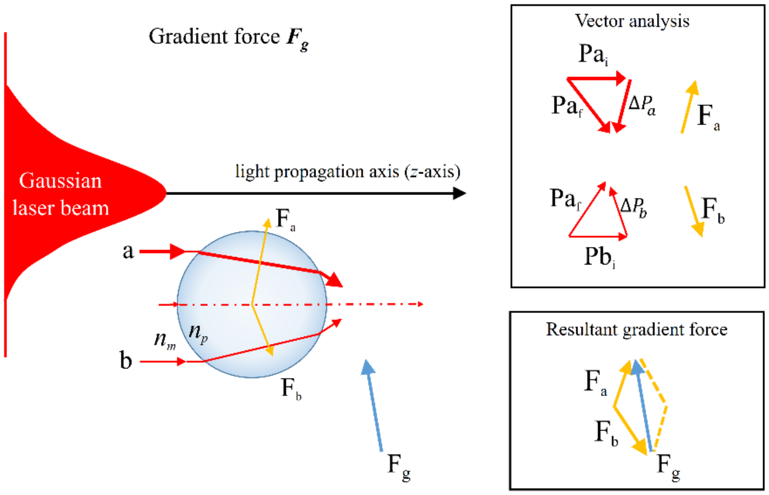

Fig. 3.4 Gradient force on a particle whose size is comparable with the wavelength used and refractive index $n_p > n_m$.

On the other hand, when the diameter of the particle is comparable to the wavelength used and the refractive index of the particle (n_p) is greater than the refractive index of the medium (n_m), i.e., $n_p > n_m$, gradient force can be described using ray optics, as is depicted in Fig. 3.4. The vectorial analysis shows the momentum changes of the rays (a) and (b), ΔP_a and ΔP_b, respectively, due to the light reflection. From this vectorial analysis, one can notice that the resultant gradient force, $\boldsymbol{F_g}$, points to the laser beam center, i.e., attracting the dielectric particle to the region of greater laser beam intensity[16].

Scattering force

Scattering force, F_s, according to electric dipole approximation is given by[116]:

$$\boldsymbol{F_s} = \frac{n}{c}\boldsymbol{I}(r)C_{scat}, \tag{3.5}$$

where n is the refractive index of the host medium, c represents the speed of light, $\boldsymbol{I}(r)$ is the beam intensity, and C_{scat} represents the scattering cross-section, and may be determined by Mie or Rayleigh theory depending on the particle´s size[116].

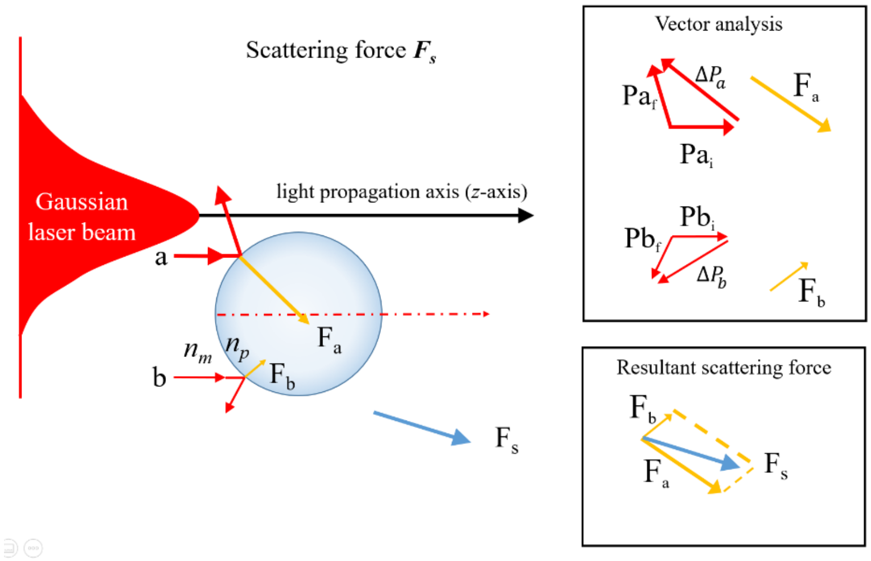

Fig. 3.5 Scattering force on a particle whose size is comparable with the wavelength used and $n_p > n_m$.

Similar to gradient force under the ray optics regime, scattering force is depicted in Fig. 3.5. The vectorial analysis shows the momentum changes of the rays (a) and (b), ΔP_a and ΔP_b, respectively, due to the light reflection. From this vectorial analysis, one can notice that the resultant scattering force, $\boldsymbol{F_s}$, points out the laser beam region, i.e., pushing the dielectric particle out of the laser beam direction (*z*-axis)[16].

Absorption force

Absorption force, F_{abs}, according to electric dipole approximation is given by[116]:

$$\boldsymbol{F_{abs}} = \frac{n}{c}\boldsymbol{I}(r)C_{abs}, \tag{3.6}$$

where C_{abs} represents the absorption cross-section, and may be determined by Mie or Rayleigh theory depending on the particle´s size.

Optical forces on a vapor bubble

Contrary to dielectric particles, bubbles composed of vapor usually exhibit a lower refractive index than the medium, i.e., $n_B < n_m$. This change in the refractive index relationship induces that the bubble is not going to be attracted towards the region of greater laser beam intensity[16,117], i.e., the vapor bubble is pushed out of the laser beam, as is depicted in Fig. 3.6.

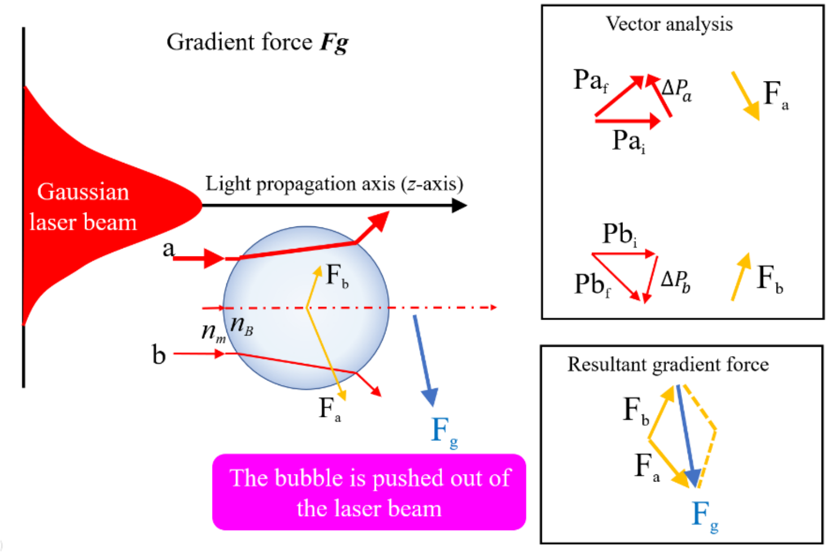

Fig. 3.6 Gradient force on a vapor bubble, $n_B < n_m$.

Marangoni force

The Marangoni force, also known as thermocapillary force, lies in the dependency of the surface tension force on temperature, i.e., an increment in the liquid temperature will provoke a decrease in the surface tension force of the liquid (Eötvos´ law)[64]. A bubble, immersed in an infinite liquid and under the action of a temperature gradient, will experience a tangential stress on its wall driven by the surface tension variations[46,91]. The bubble will move towards the heat source while the liquid flows to the colder regions, as is depicted in Fig. 3.7.

Marangoni force is given by[35,42]:

$$\boldsymbol{F_M} = -2\pi R^2 \boldsymbol{\nabla T}\frac{d\sigma}{dT}, \tag{3.7}$$

where $\boldsymbol{\nabla T}$ indicates the temperature gradient and σ is the surface tension of the host liquid.

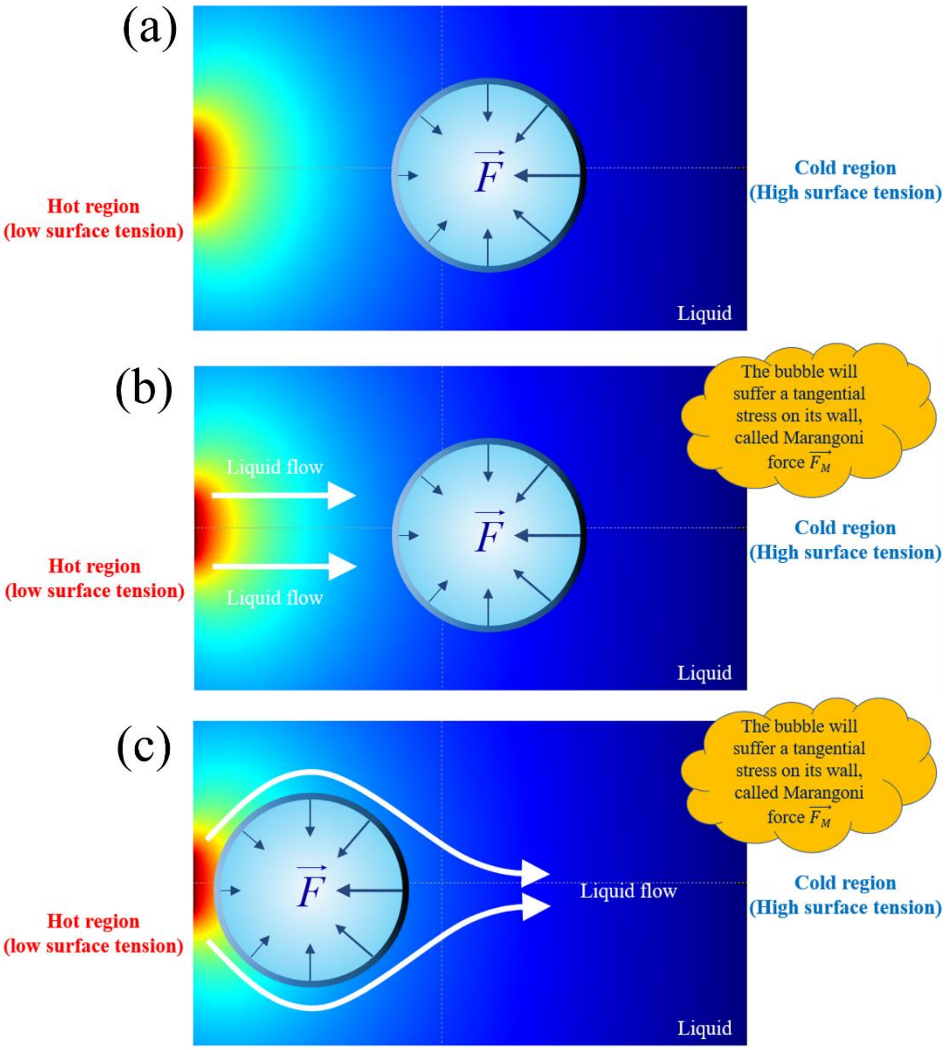

Fig. 3.7 Marangoni force over a vapor microbubble.

Inertia force

Inertia force, $\boldsymbol{F_i}$, also called added mass, lies on the Newton´s second law, i.e., it states that the acceleration of an object is dependent on the net force acting upon the object/particle and the mass of the object/particle[118].

Specifically for bubbles immersed in liquids, the inertia force of the fluid surrounding an accelerating bubble is characterized by an added mass, and is given by[118–120]:

$$\boldsymbol{F_i} = m\boldsymbol{a} = \frac{4}{3}\pi R^3 \rho_l C_b \frac{d\boldsymbol{u}}{dt}, \tag{3.8}$$

where $C_b = 1/2$ is the bubble-shape coefficient[119].

Chapter 4. Trapping and 2D manipulation of microbubbles by low power CW laser

The manipulation of gas and vapor microbubbles inside aqueous solutions has attracted attention because of their applications in the industry as actuators, micro-valves[41,121], manipulation of micro-objects[122,123], development of micro-motors[83,124], ink printers[125], lithography[6], among others. The main mechanism used for the manipulation of microbubbles are based on thermal[12,42,62], optical[44,126], and acoustic phenomena[14,127]. Thermal techniques based on decrement of surface tension, also called thermocapillary, produce a tangential stress at the vapor-liquid interface called Marangoni force[41,42] . Optical techniques are based in transfer of linear momentum, need a special beam profile produced by beam shaping; while acoustic techniques based on Bjerknes forces employ ultrasonic waves generated by piezoelectric micro-materials[127]. The study of thermal gradients for the generation and migration of microbubbles has been proposed using Joule heating in electrical devices[67]. X. Qu *et al*.[65] investigated the dynamics of microbubbles using a horizontal array of electric micro-heaters fabricated using standard micromachining technique. The voltage applied to the array is modulated by a signal generator and amplified for the generation of a thermal gradient. The results showed that the microbubbles can be periodically displaced by the Marangoni force between two heaters separated ~23 μm. By using a laser focused on 50 μm thick cell filled with an absorbing solution, manipulation of microbubbles was also possible without the need of complex microfabrication techniques for the generation of thermal gradients[47]. In this report, the bubbles were already present in the solution with diameters of 0.2-1.2 mm (in fact the bubbles adapted a cylindrical shape) and were attracted towards areas of higher radiation intensity. Recently, Angelsky *et al*.[128]reported the generation and manipulation of microbubbles based on Marangoni force using a nanocolloidal solution and a CW laser at 980 nm and 2 W of power. Light absorption by the nanoparticles dispersed in water generated a thermal gradient of ~$2\text{x}10^5$ K m^{-1} resulting in an array of microbubbles with radii up to 130 μm at the beam spot. The array of microbubbles could be manipulated in 2D by displacement of the laser beam.

In this chapter, we report the photothermal generation of vapor microbubbles in ethanol due to the radiation absorption from the immobilized silver nanoparticles at the core of an optical fiber. Once the microbubble is created it can be manipulated in 2D and 3D using a low power CW laser at 1064 nm.

Experimental description

In our experimental arrangement, silver nanoparticles (AgNPs) were immobilized on the two multimode optical fibers ends (50/125) using the photodeposition technique[129–131]. A colloidal suspension was made by mixing 0.3 mg of Sigma-Aldrich silver nanopowder (particle size <100 nm) in 2 ml of ethanol, which was mixed in a 4.5 ml capacity polystyrene cuvette. The mixture was homogenized using an ultrasonic bath for 5 minutes. The photodeposition was performed using a IPG Photonics continuous wave laser (CW) model

YLR-5-1064-LP that emits at 1064 nm with a maximum power of 5 mW. The laser beam was divided by a 50/50 infrared beam splitter and each beam coupled to the optical fiber terminals using two 10x microscope objectives as shown in Fig. 4.1.

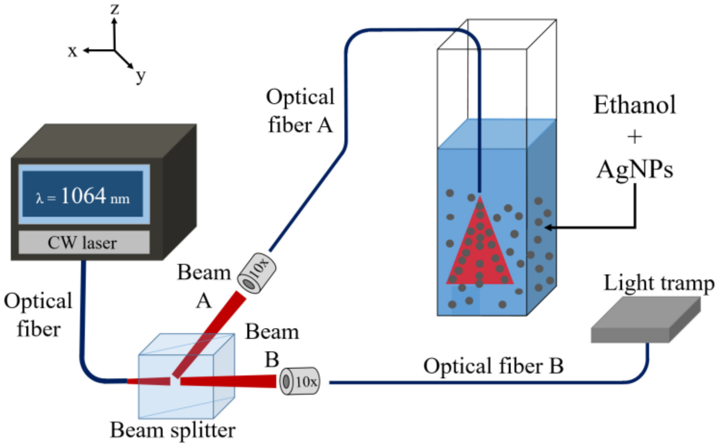

Fig. 4.1 Experimental setup for photodeposition AgNPs at the core of the optical fibers.

The photodeposition of the AgNPs on the core of the fibers was carried out by submerging each tip of the optical fiber inside a cuvette filled with a colloidal suspension of alcohol and AgNPs. The rate of photodeposition was monitored using a power meter to achieve an output power of 23 mW (input power 120 mW) corresponding to 7.0 dB attenuation.

Visualization of the generation and manipulation of microbubbles was performed using a 50x microscope objective with NA = 0.26 and a Phantom high-speed video camera model v7.3 operating at 6600 fps (~151 μs between frames) and illuminated with 12V/20W halogen lamp. The tips of the optical fibers with the photodeposited AgNPs were introduced vertically and horizontally into a cuvette filled with ethanol as shown in Fig. 4.2(a) and 4.2(b), respectively.

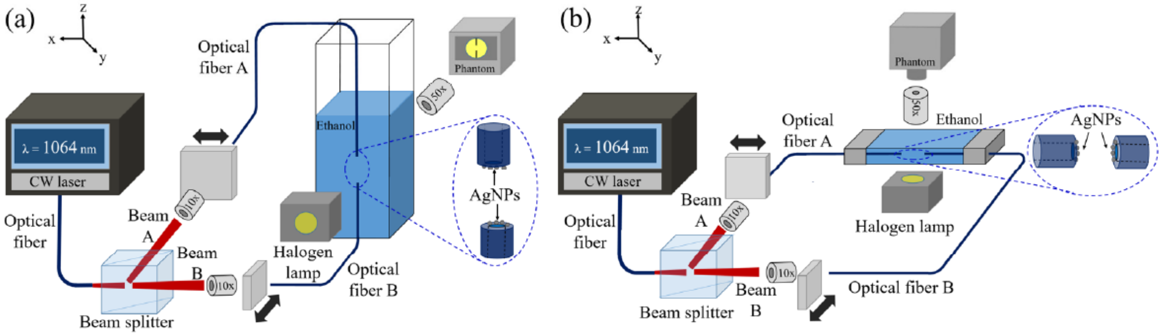

Fig. 4.2 Experimental setup for the generation and manipulation of microbubbles. (a) Optical fibers vertically opposed. (b) Optical fibers horizontally opposed.

The generation of a microbubble on the fiber tip was carried out by allowing the passage of beam B(A) while beam A(B) is obstructed. The AgNPs deposited at the core of the fiber were heated up by light absorption and then heat is transferred to the surrounding liquid. Depending on the incident power a bubble may be created. Once the bubble is created, beam B(A) is obstructed and beam A(B) is allowed to pass. Thus, the bubble stops growing but maintains its size on the time scale of the experiments. The bubble is affected by the temperature gradient on the opposite fiber tip and is attracted towards it. It should be mentioned that the power used to produce the temperature gradient opposite to the bubble is slightly below (5% less) of that needed for the generation of microbubbles.

Experimental results

Figure 4.3 shows typical snapshots of the microbubble evolution on the tip of the optical fiber considering the experimental setup showed in Fig. 2(a) and laser power of 16 mW. The bubble's radius grows over time due to the continuous ethanol vaporization reaching a radius of 63 μm in 50 ms. The rate of expansion obviously depends on the beam power, however, it should not increase over certain value because cavitation may be produced. The violent collapse of the cavitation bubble may detach the AgNPs until eventually no bubble could be created.

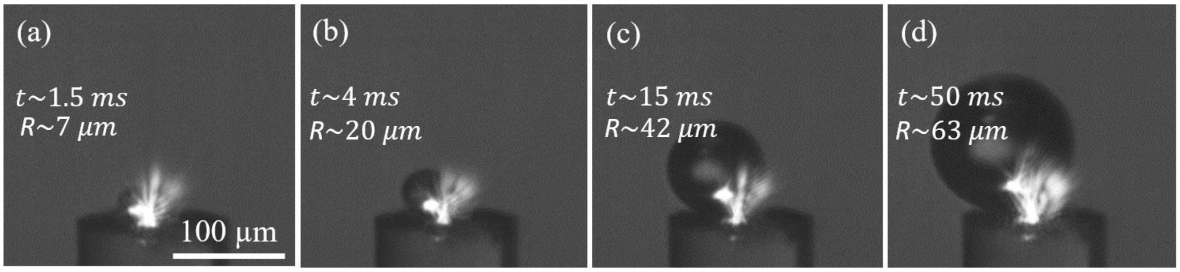

Fig. 4.3 Sequence of formation (a) and growth of a microbubble (b-d) adhered to the tip of an optical fiber. Bright areas represent scatter light picked up by the camera.

Once the bubble has achieved its desired size, laser beam B(A) is obstructed and beam A(B) is allowed to pass, heating up the other fiber tip. The image sequence shown in Fig. 4.4 corresponds to vertical ($+z$ direction) displacement of the microbubble between the two tips separated by ~480 μm and where only the beam on the upper fiber is on. It can be observed that the microbubble (115 μm radius) covers the distance in 3.5 ms with a maximum velocity of 238 mm/s while maintaining its spherical shape. It is important to mention that the velocity of the microbubble is not constant and it increases when it approaches the heat source.

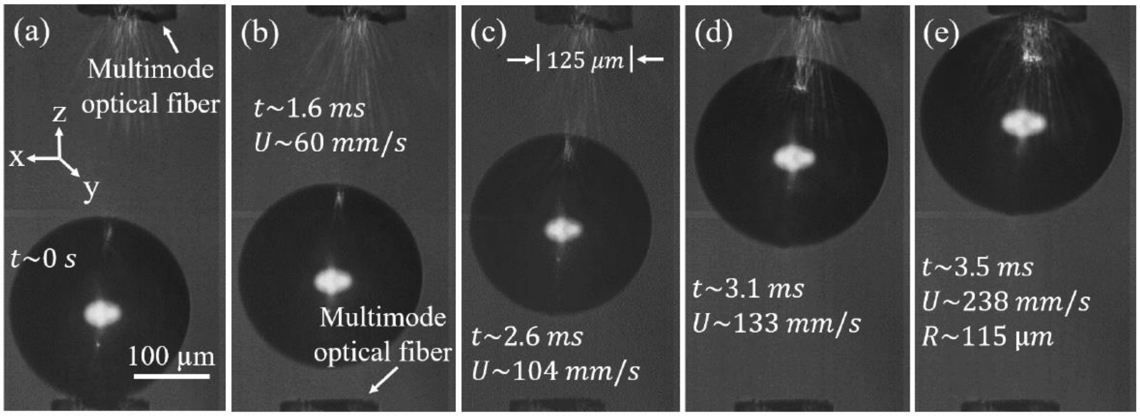

Fig. 4.4 Snap shots of a travelling microbubble in the + z direction between two opposed optical fibers. The bubble is generated in the lower fiber and attracted towards the upper fiber.

In order to assess the effect of convective currents and buoyancy on the bubble displacement, the bubble was created on the upper fiber and displaced downwards as shown in Fig. 4.5. The temperature gradient was generated at the lower tip inducing the manipulation of the microbubble in the -*z* direction. It can be observed that the microbubble (115 µm radius) covers the distance in 5.3 ms with a maximum velocity of 154 mm/s. Note that the downwards velocity is slower than the upwards.

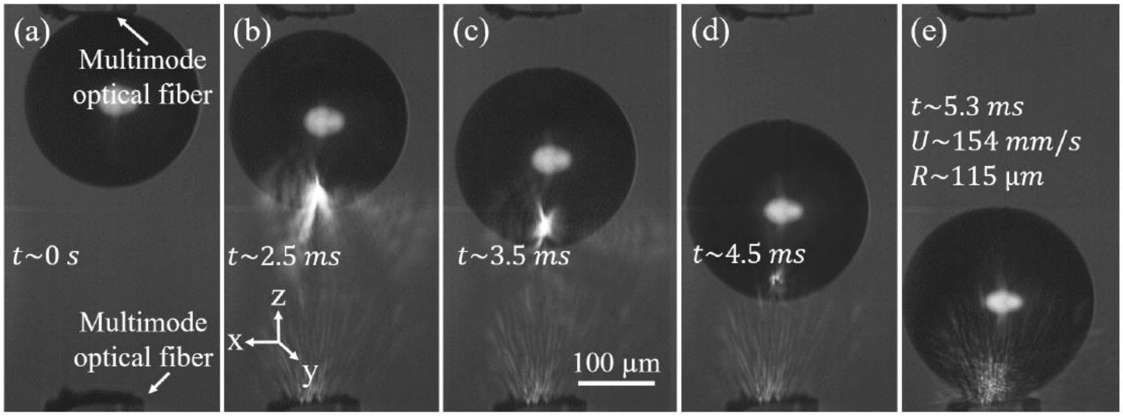

Fig. 4.5 Snap shots of a travelling microbubble in the -z direction between two opposed optical fibers. The bubble is generated in the upper fiber and attracted towards the lower fiber.

Figure 4.6(a) shows a frame of Visualization 4.1 of the periodical manipulation in 2D of a microbubble between two horizontally placed fibers separated by ~1 mm as shown in Fig. 4.2(b). It is important to note that in this configuration the buoyancy, gravity and drag force do not exist as the height cell is approximately equal to the microbubble size. Furthermore, it can be seen that by switching the position of the temperature gradient it was possible to carry out the horizontal manipulation of a 300 µm radius microbubble (on *y*-axis). It is also possible to manipulate microbubbles when the ends of the fibers are off-axis, as shown in Fig. 6(b) Visualization 4.2. In the Fig. 4.6(b) it can be observed that the two fiber tips are spaced 485 µm apart and misaligned 33° with respect to normal. The temperature gradient was generated at the upper tip, producing the upwards displacement (+*z*) of the 90 µm radius microbubble. Figure 4.6(c) shows a frame of Visualization 4.3 of the manipulation of a microbubble with a radius of 80 µm between two vertically opposed optical fibers, spaced apart 560 µm and misaligned 43° with respect to normal. This time the temperature gradient was generated in the lower fiber, displacing the microbubble in the *-z* direction, as shown in Visualization 4.3. Both Visualization 4.2 and Visualization 4.3 were record at 6,688 fps for 21 ms.

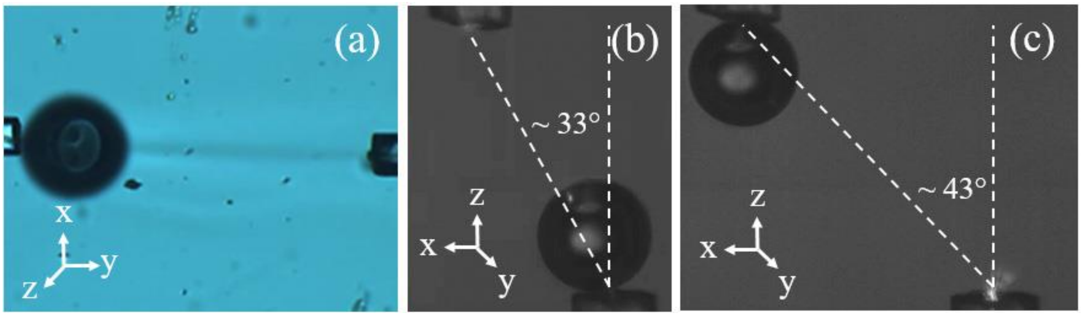

Fig. 4.6 Manipulation of a microbubble between two horizontally opposed optical fibers (a) due to the switching of the temperature gradients (see Visualization 1). Manipulation of a microbubble in the + z and -z direction between two vertically opposed and off-axis optical fibers (a) 33 ° (see Visualization 2) and (b) 43 ° (see Visualization 3) respectively.

Discussion

The results show that microbubbles can be generated by heating due to light absorption by the AgNPs deposited at the fiber end submerged in ethano[132–134]. Here we show the calculations of the temperature spatial distribution produced by light absorption by the deposited nanoparticles. The steady-state solution for the temperature increase due to a single nanoparticle of radio R in an homogeneous media is given by $\Delta T(r) = \delta_{abs} I/(4\pi\kappa r)$ for $r > R$, where I is the light intensity illuminating the AgNP, δ_{abs} is the absorption cross-section of the AgNP, and κ is the thermal conductivity of the surrounding medium[135]. For a single nanoparticle, the temperature beyond its diameter decays as $1/r$, but for a collection of nonuniform (both in diameter and spatial distribution) or even for uniform closely packed nanoparticles, these temperature decays may be completely different. Thus, calculation and measurements of the temperature profile are difficult to perform given the small dimensions of the volume and time scales involved. However, we can numerically estimate the spatial temperature distribution making reasonable assumptions. First, we simulate the deposited layer as uniform sized nanoparticles having homogenous spatial distribution, so we can assume a uniform temperature distribution and then solve the heat diffusion equation in steady-state coupled to the Navier-Stokes equations using COMSOL Multiphysics. The configuration is quite simple: 50 µm diameter fiber optic is inserted in ethanol and the fiber core-ethanol interface is set to a fixed temperature as shown in Fig. 4.7. The 2D spatial temperature distribution is shown in Fig. 4.7(a) and it is possible to observe that this distribution has spherical symmetry while Fig. 4.7(b) shows the temperature profile along a particular direction r. The continuous line represents the fit to an exponential decay function. Therefore, the temperature function in the radial direction is given by:

$$T(r) = T_0 + \Delta T exp\left(-\frac{r}{r_D}\right), \tag{4.1}$$

where T_0 is the ambient temperature, ΔT represents the temperature difference between the fiber core-alcohol interface and ambient temperature, and $r_D \approx 534$ µm represents the heat diffusion length. Although the fitting is not perfect, it can be taken as a good approximation. The achieved temperature depends on the beam power. In order to produce nucleation in ethanol (temperature for vaporization ~78 °C) and therefore bubble formation, a threshold power of 16 mW is needed. In fact, Fig. 4.3(a) shows the bubble formation obtained with the threshold power. Around time t = 1.5 ms the bubble is clearly noticeable.

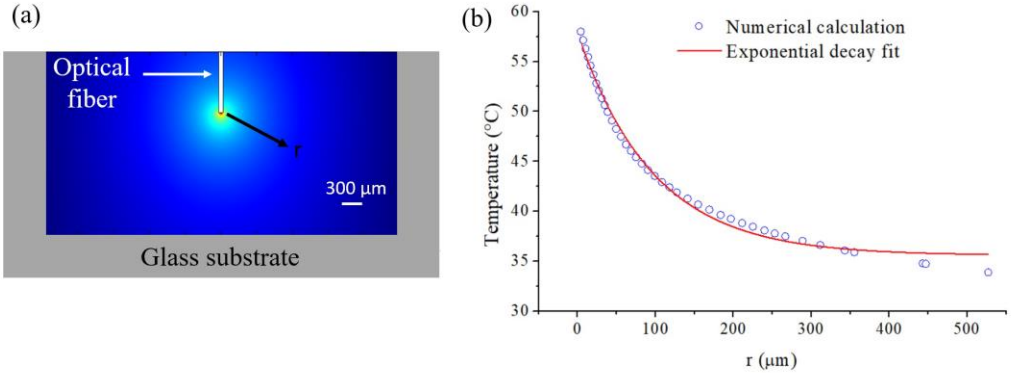

Fig. 4.7 (a) Configuration used to calculate the temperature spatial distribution using COMSOL. The fiber is placed into the cell containing ethanol. (b) Temperature profile from the fiber to the bottom of the cell which in this case r coincides with the z axis.

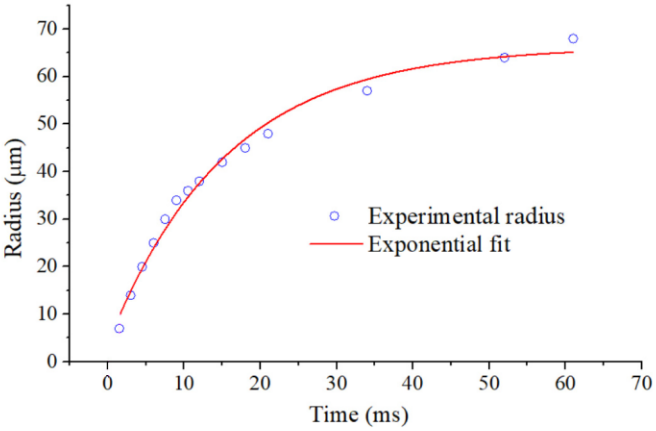

Fig. 4.8 Microbubble radius as function of time.

Figure 4.8 shows the bubble radius dependence on time. The curve fitting was obtained using the equation $R(t) = R_{max}\left(1 - exp\left(-t/\tau_0\right)\right)$ where the maximum bubble radius for this particular power is R_{max} = 66 µm and formation time τ_0 is 15 ms. For this reason, it is difficult to obtain bubbles of the same size (< 60 µm) unless a precise control on the opening time is achieved; however, in our case the control is manual. Previous studies have shown that it is possible to generate microbubbles with low-power continuous-wave lasers in a relative short time[128,136,137].

A microbubble located in the vicinity of the temperature gradient as seen Fig. 4.7(a) will experience the so called Marangoni force F_M which moves the bubble towards the hot region[91,138,139]. This force arises by the temperature dependent surface tension differential along the bubble's surface. Due to a tangential stress on the surface tension of the microbubble, the liquid will flow from the lower surface tension (higher temperature) region to the higher surface tension (lower temperature) region as seen Fig. 4.9. The Marangoni force $\boldsymbol{F_M}$ is given by[91]:

$$\boldsymbol{F_M} = -2\pi R^2 \boldsymbol{\nabla T} \frac{d\sigma}{dT}, \tag{4.2}$$

where R is the radius of the microbubble, $\boldsymbol{\nabla T}$ is the temperature gradient in the direction of the radiation source and $d\sigma/dT$ is the temperature derivative of liquid (ethanol) surface tension σ ($-0.1\text{x}10^{-3}$ $\text{Nm}^{-1}\text{K}^{-1}$) which is practically constant from room temperature up to 70 °C[11]. In addition to the Marangoni force, the microbubble immersed in a liquid also experiences the $\boldsymbol{F_b}$ buoyancy, gravity $\boldsymbol{F_G}$, and drag forces $\boldsymbol{F_d}$ [11,114,140]. Radiation pressure is negligible given the low power of the beam and the large divergence angle of the light leaving the optical fiber, in addition, light scattering by the nanoparticles contributes to decrease the radiation pressure on the bubble surface[129]. So the buoyancy, gravity and drag forces are given by:

$$\boldsymbol{F_b} = \frac{4}{3}\mu R^3 \boldsymbol{g}(\rho_l - \rho_v), \tag{4.3}$$

$$\boldsymbol{F_G} = \frac{4}{3}\mu \rho_l \boldsymbol{g} R^3, \tag{4.4}$$

$$\boldsymbol{F_d} = -6\pi\mu R\boldsymbol{u}, \tag{4.5}$$

where $\boldsymbol{g}$ is the gravitational acceleration, $\boldsymbol{u}$ is the velocity of the microbubble, $\mu = 1.071\text{x}10^{-3}$ Pa·s is the dynamic viscosity of ethanol, $\rho l = 789$ kg/m^3 and $\rho b = 3.4$ kg/m^3 are the density of liquid and the vapor of ethanol, respectively. So, the total force $\boldsymbol{F_T}$ acting on the microbubble traveling between two opposed optically optical fibers is:

$$\boldsymbol{F_T} = \boldsymbol{F_b} + \boldsymbol{F_G} + \boldsymbol{F_d} + \boldsymbol{F_M}, \tag{4.6}$$

The direction of the forces involved in the displacement of a microbubble due to the presence of a temperature gradient generated at the top tip of the optical fiber is shown in Fig. 4.9. The buoyancy force $\boldsymbol{F_b}$ always points upwards while the gravity force $\boldsymbol{F_G}$ always acts downwards. Since the vapor density is two orders of magnitude smaller than the density of liquid, gravity forces will not be considered. The Marangoni force always is directed to the heat source and its direction can be reversed, as one can observe in Fig. 4.9.

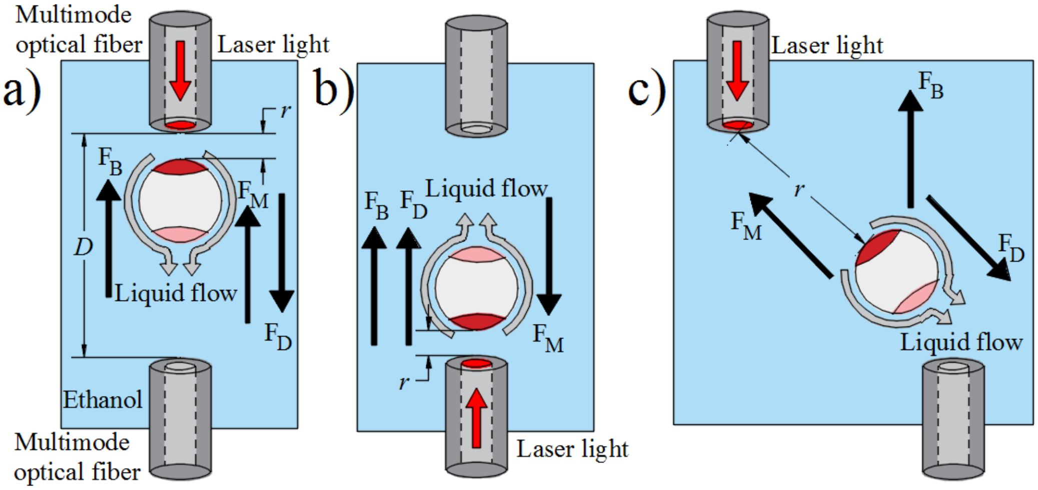

Fig. 4.9 (a) Displacement of a microbubble in the + z direction, (b) displacement of a microbubble towards –z direction and (c) displacement of microbubble when the optical fibers are off-axis.

Figure 4.10 shows the Marangoni force and the total force as a function of the distance r between the microbubble and the heat source considering the optical fibers are placed as in Fig. 4.9(b). In the graph, it can be observed that $\boldsymbol{F_M}$ increases when the microbubble approaches the heat source and reaches a magnitude of 400 nN for a 110 µm radius microbubble. Once the bubble reaches the heat source (optical fiber tip) comes to a complete stop. The magnitude of the buoyancy force is 43 nN for a 110 µm radius microbubble. Note that when r is larger than 798 µm, the net force changes sign since buoyancy and drag force overcomes the Marangoni force. The maximum magnitude of Marangoni force for a 110 µm particle radio is one order of magnitude larger than both drag and buoyancy force and is five orders larger than typical gradient optical forces in optical tweezers[141].

The total velocity $\boldsymbol{u}$ of a microbubble immersed in a liquid and under the presence of a temperature gradient is given by:

$$\boldsymbol{u} = \boldsymbol{u_M} + \boldsymbol{u_T}, \tag{4.7}$$

where $\boldsymbol{u_T}$ is the bubble terminal velocity[114] and $\boldsymbol{u_M}$ is the Marangoni velocity, given by[11]:

$$\boldsymbol{u_T} = \frac{2\boldsymbol{g}R^2}{9\mu}(\rho_b - \rho_l), \tag{4.8}$$

$$\boldsymbol{u_M} = -\frac{d\boldsymbol{\sigma}}{dT}\frac{R}{2\mu}\Delta T. \tag{4.9}$$

Using Eq. (4.1), Eq. (4.9) becomes:

$$\boldsymbol{U_M} = \frac{d\boldsymbol{\sigma}}{dT}\frac{R}{2\mu r_D}\Delta T\left(-\frac{r}{r_D}\right). \tag{4.10}$$

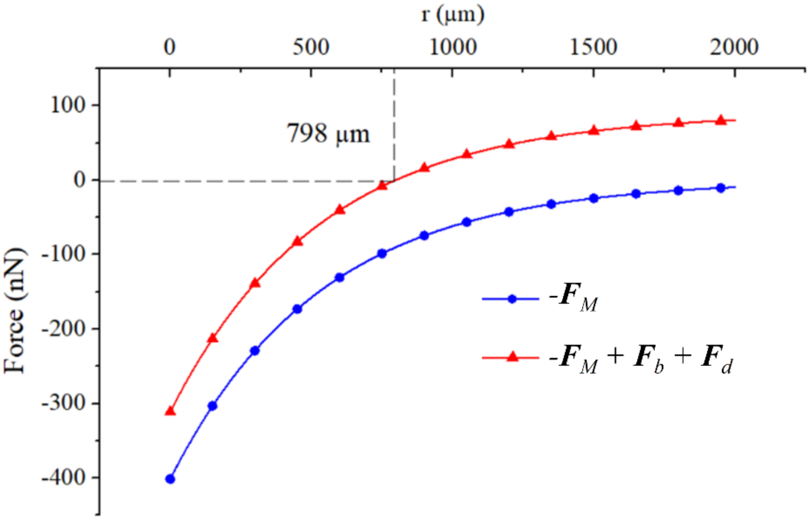

Fig. 4.10 Marangoni force on a microbubble (with radius R = 110 μm, heat source is placed at r = 0) as a function of the distance (r) between heat source and the microbubble when the heat source is placed at the lower fiber.

The Marangoni velocity acts in the same direction as the temperature gradient while the terminal velocity always is directed along the +*z* direction. For such reason, one should expect a difference in the velocities of the bubble when it moves downwards or upwards as shown in Fig. 4.11. The results show that for a microbubble of 115 μm radius, the net maximal velocity moving upwards along the *z* direction reaches 238 mm/s, while the maximal velocity downwards reaches only 155 mm/s. According to Eq. (4.10), as the bubble approaches the heat source its velocity increases exponentially, which agrees well with experimental measurements shown in Fig. 4.11(a).

Combining the upwards and downwards velocity bubble we can obtain that $\boldsymbol{u_T} = (\boldsymbol{u}^{+} - \boldsymbol{u}^{-})/2$ and $\boldsymbol{u_M} = (\boldsymbol{u}^{+} + \boldsymbol{u}^{-})/2$, where the super indices indicate the direction of the travelling bubble. Calculating the terminal velocity using Eq. (4.8) one obtain $\boldsymbol{u_T}$ = 19.65 mm/s while from experimental data shown in Fig. 4.11(b), the terminal velocity is ~20 mm/s, which agrees quite well with the theoretical predictions.

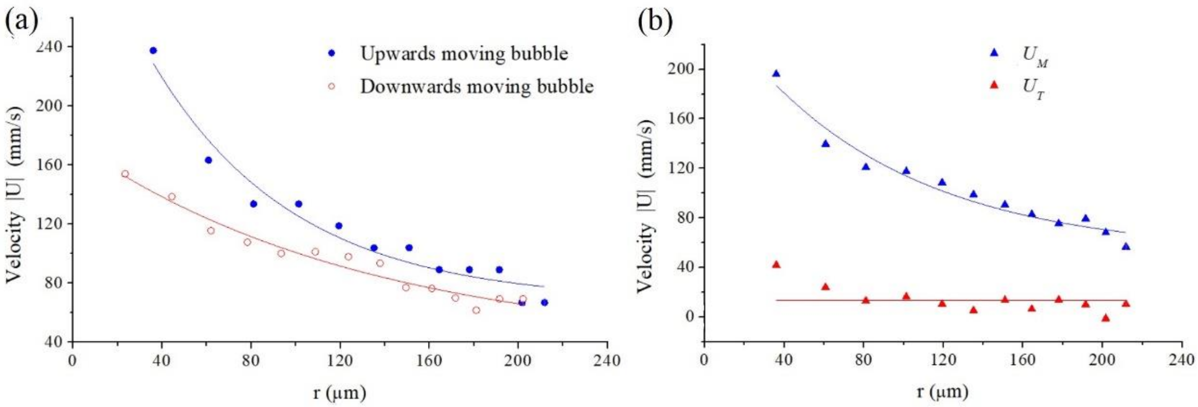

Fig. 4.11 Microbubble displacement velocity as a function of the distance between the heat source and the microbubble. (a) Dots correspond to experimental data and continuous line corresponds to fittings. (b) Triangles correspond to Marangoni and terminal´s velocities as a result to combining experimental results and continuous lines correspond to fitting of $\boldsymbol{u_M}$ *and* $\boldsymbol{u_T}$*.*

Conclusions

It was shown that the generation and 2D manipulation of microbubbles in a non-absorbent liquid can be carried out through by Marangoni forces activated by light absorption at photodeposited metal NPs on the tip of an optical fiber. Thus, gradient temperature modulates the surface tension of the bubble wall producing a force directed towards the heat source. The temperature gradient allowed the manipulation of microbubbles even when the optical fibers are laterally displaced. Numerical simulations indicate that the temperature gradient is described by an exponential function. Thus, an expression for the Marangoni velocity was obtained. We find that the bubble velocity can be decomposed in two components: constant velocity (terminal velocity) and an accelerated one (Marangoni). Comparison with experiment and theory shows good agreement. The manipulation of a microbubble in 2D depends on the gradient temperature, microbubble size and the separation distance between the optical fiber tips, whilst the buoyancy force also is present. The use of optical fibers provides precise spatial control to generate localized temperature gradients; allowing to generate and manipulate microbubbles in areas of difficult access, increasing its accessibility due to the low equipment requirement for its implementation. The generation and manipulation of microbubbles can be used to generate rotary motion in micromotors, directing and controlling flows, transporting particles in MEMS (micro-electro-mechanical-system), among others.

Chapter 5. Trapping and 3D manipulation of microbubbles by pulsed laser

Bubbles are a key role in fields such as thermodynamics[142,143], microfluidics[144–146], biomedical[4,88], hydraulics[83,121] but is also relevant in applications such as valves[86,124], motors[83,147], needle-free injectors[4], optical trapping and sorting[6,86,148,149] among others. These applications require extreme spatial control of bubbles position to accomplish their purposes; however, this is quite difficult to achieve because many dynamic processes are involved. A great deal of both experimental and theoretical works have been carried out to fully understand the dynamics of the bubbles allowing their 2D manipulation based on acoustic, thermal, and optical phenomena[11,42,46,128,150]. The combination of these last two, also called optothermal effect, has shown to have several advantages at the microscale regime[132,136]. On the other hand, optical phenomena provide both noncontact and noninvasive approaches of bubbles manipulation while thermal phenomena can provide forces many orders of magnitude larger than optical ones[9,42,46]. So, optothermal phenomena offers the best of the two worlds.

Optical generation of microbubbles in liquids is typically achieved by laser radiation with either CW[42,46,128,150] or pulsed lasers[151–153]. The former one needs an absorbent medium to convert the incident light into heat[132–134], whereas the latter one occurs in highly transparent media through means of multiphoton absorption leading to optical breakdown[154–156]. Optical manipulation of microbubbles is not an easy task since the refractive index of vapor is smaller than the surrounding liquid; however, “bottle” beams, i.e., donuts-shape beams with a dark center allows manipulation of low refractive index particles[141,157,158]. Optical trapping of large bubbles cannot be achieved with optical means; however, recently it was reported an optothermal method[150] for the generation and 2D manipulation of microbubbles by Marangoni force[11,42,46,128,150].

In this chapter, we present both experimental and theoretical results of 3D manipulation of microbubbles generated by light-absorption from a nanosecond pulsed laser at silver nanoparticles (AgNPs) photodeposited onto the core of a multimode optical fiber. Each laser-pulse generates a small bubble by the explosive phase transition, which later ejects microbubbles into the liquid, forming a microbubbles-stream that moves away from the tip of the optical fiber until they coalesce, forming a large microbubble. This bubble is eventually attracted to the optical fiber by the Marangoni force while it is continuously hit and fed by the microbubbles-stream. The balance of the involved forces drives the 3D manipulation of the large bubble.

Experimental description

In our experimental setup, a nanosecond laser pulse (Spectra Physics Q-Switch at 532 nm, τ_p=5 ns & 10 kHz repetition rate) is coupled to a multimode optical fiber (50 μm core diameter) by a 10x microscope objective (MO). At the distal end of the optical fiber, AgNPs (Sigma-Aldrich, particle size < 100 nm) were photodeposited following the procedure reported in[129,130] until 3.5 dB of attenuation was achieved. After that, the fiber end with the photodeposited nanoparticles was submerged vertically (z-axis) in a glass cuvette containing pure ethanol. For visualization of the bubble dynamics, a 50x microscope objective (Mitutoyo, NA = 0.26) is coupled to a high-speed camera Phantom v7.3. A halogen lamp, as depicted in Fig. 5.1, supplies the illumination.

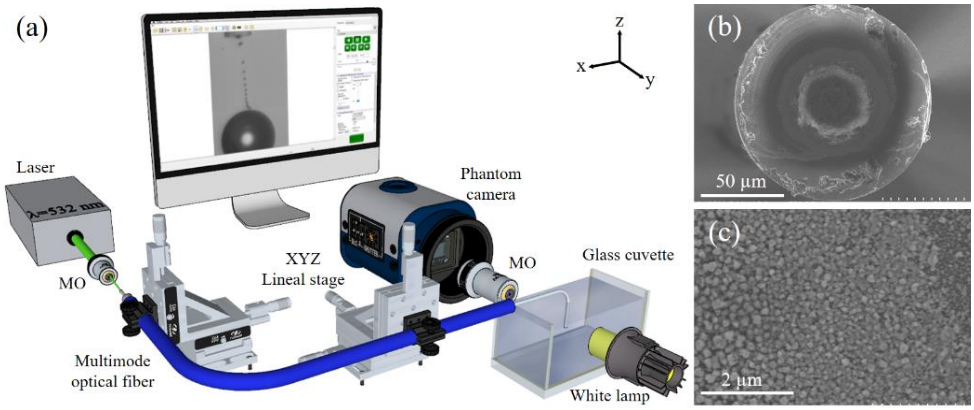

Fig. 5.1 (a) Experimental setup for the generation and 3D manipulation of microbubbles. A pulsed laser is coupled to the multimode optical fiber using a microscope objective (MO). Bubbles dynamics are viewed with a fast Phantom camera. (b) Image of the distal end of the multimode optical fiber obtained with a SEM after 3.5 dB of attenuation was achieved. (c) Closer view of the optical fiber core showed on (b).

It is important to clarify that no bubbles are produced when no nanoparticles are photodeposited at the energy levels reported in this work. So, the driving mechanism of microbubble generation is thermal effects produced by light absorption by the nanoparticles.

Experimental results

Figure 5.2(a) shows snapshots of the bubble growth dynamics using 2.1 µJ per pulse laser energy. With each laser pulse, a bubble is detached from the fiber end forming a long column of bubbles with an increasing diameter (and decreasing velocity) as they move away. A similar phenomenon was reported by Ohl *et al*.[53,81] but, they employed a CW laser source or Joule heating. Besides, they do not report the formation of a larger bubble or its trapping and manipulation. As the bubbles speed decreases, they catch up and eventually coalesce forming a larger bubble, called hereafter, as the main-bubble (125 µm of radius after t ~1.6 s). According to our experimental results, it was noticed that the main-bubble approaches the fiber end (heat source) as it grows. In fact, it can be trapped and manipulated in 3D as shown in **Visualization 5.1**. Figure 5.2(b) shows the time dependence of the main-bubble radius measured from the video and the calculated one by adding the ejected small bubbles with an average radius of 5.5 µm. The growth rate of the main-bubble is faster at the beginning because the contribution of each small bubble to the volume of the main one is significant but eventually, its contribution becomes less significant for such reason the dynamics of the radius of the main-bubble is better described as with a double exponential function, $r(t) = r_{max}\left[1 - r_1 exp\left({}^{-t}/_{t_1}\right) - r_2 exp\left({}^{-t}/_{t_2}\right)\right]$, where r_{max} is the maximum bubble radius, r_1,

r_2, t_1, and t_2 are radius and time constant fast and slow contribution to the bubble growth, respectively (see Fig. 2 for its values). The disagreement between both curves is because the coalescent bubble radius is larger at the beginning of the video but as the main-bubble is attracted towards the fiber the coalescent bubbles become smaller, i.e., the radii of the coalescent bubbles are spatially and temporarily varying, however, our approaches gives a good estimate of the final main-bubble radius. It is important to notice that for >13 000 bubbles, its radius does not change appreciably, and thus quasi-stable trapping and manipulation can be achieved.

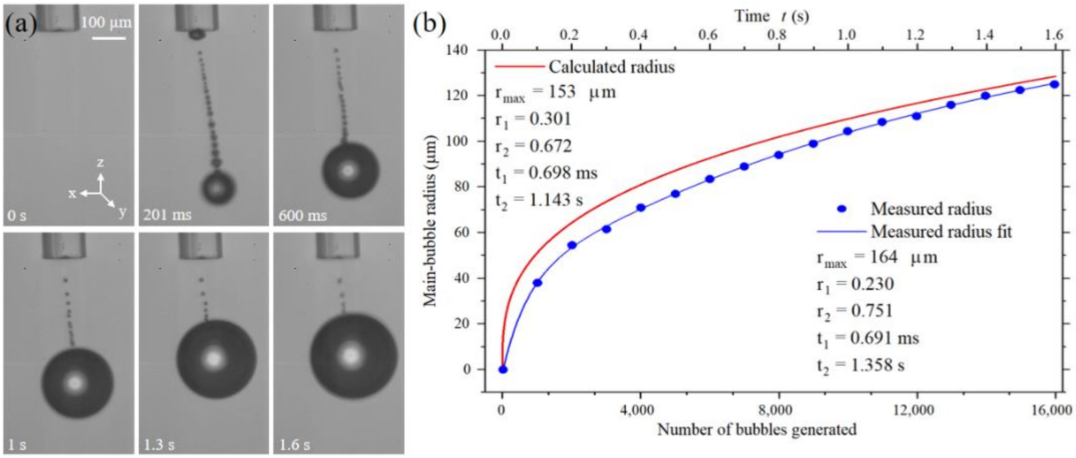

Fig. 5.2 Growth of the main-bubble as a function of time. (a) Snapshots of the temporal evolution of the main-bubble radius recorded at 6,600 fps. (b) Blue dots correspond to the measured from the video main-bubble radius. The continuous blue line is fit to a double exponential function. The lower horizontal axis represents the number of coalesced bubbles and the upper one the corresponding elapsed time. The red solid line indicates the calculated radius of the main-bubble as a function of microbubbles generated at 2.1 µJ per pulse-energy at a repetition rate of 10 kHz.

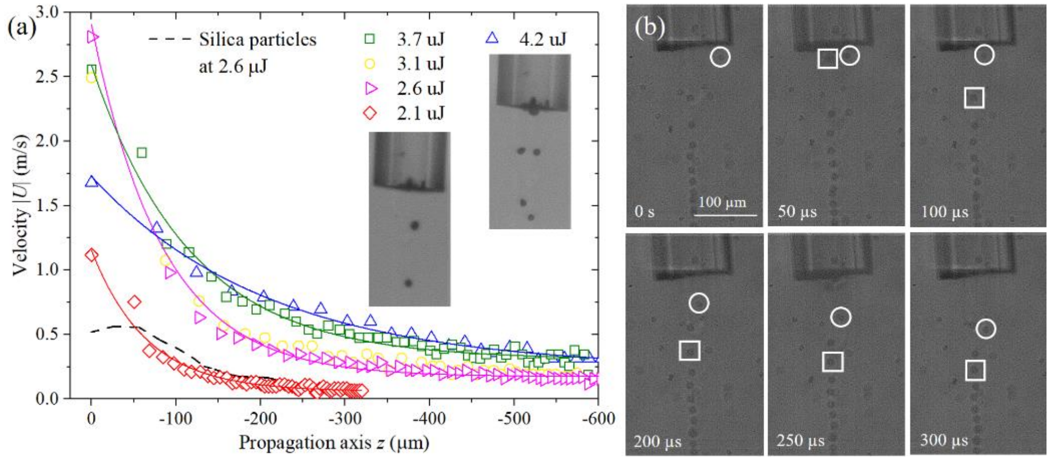

Fig. 5.3(a) Profile of the bubble's velocity as a function of the laser energy, extracted from recorded images at 43,000 fps. Continuous lines are fit to an exponential function. (b) Snapshot of the tracers and bubbles when a 2.6 µJ of laser energy was used. White circles and white squares indicate the tracer and bubble displacement, respectively. Both the bubble and the tracer start from the same position at t = 50 µs, however, the bubble moves faster as time goes on.

Figure 5.3(a) shows the velocity U of the ejected bubbles from the tip of the optical fiber along the light propagation (z-axis) at different laser pulse's energy. The bubbles´ velocity was extracted from the recorded video at 43,000 fps using the Phantom control camera software. The frame rate provides information of the temporal dynamics while the spatial information was obtained from the diameter (125 µm) of the optical fiber. In all cases, the velocity of the ejected bubbles is faster around the fiber end and then decreases exponentially with the distance. As the laser energy increases, the velocity also increases. For pulse energy < 2 µJ no bubbles were formed and for pulse energy > 4.2 µJ, two bubbles were expelled but with lower velocity, as it is shown in the inset of Fig. 5.3(a). The thermal gradient produced by the nanoparticles at the fiber end also produces convective currents. In order to measure the velocity of the convective currents, silica microparticles (3 µm) were added as tracers to the solution and by video-analysis, its velocity ($velocity_{max}$ ~0.5 m/s) was determined (broken line). The microparticles tracers stops around 300 µm and then they are dragged out of the field of view by the convective currents. Figure 5.3(b) is a closed-up around the fiber end where a microparticle (enclosed by a circle) is tracked along with a bubble (enclosed by a square). Notice that the bubble velocity is always faster than the tracer one and travel longer along the propagation distance. This distance is determined by the laser pulse energy.

Figure 5.4(a) shows snapshots of the bubbles temporal evolution generated with 3.1 µJ per pulse energy, i.e., single bubble generation regime. With each laser pulse, a semi-spherical shape bubble is created that rapidly grows up to its maximal radius R_{max} while remains attached to the fiber, this is the typical behavior of thermocavitation bubbles[105,106]. After that, the bubble collapses taking a mushroom-shape form and a small bubble is expelled from the fiber end. However, if the pulse energy is increased beyond 4.2 µJ, as shown in Fig. 5.4(b), the bubble is larger, and its collapse is more complex since two or even three bubbles are created, and a smaller bubble always remains on the fiber. Detailed time evolution of the bubble dynamics was not possible with our fast camera, so only snapshots were captured.

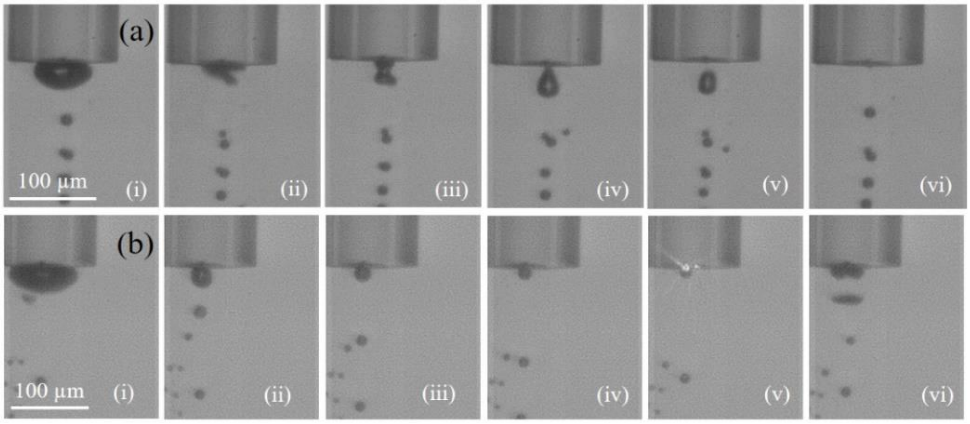

Fig. 5.4 (a) Snapshot of the optothermal generation of microbubbles: (i) maximum bubble size, (ii) bubble collapse, (iii) bubble ejection, (iv-vi) bubble moves away from the optical fiber. (b) 4.2 µJ of laser-pulse energy. (i) Maximum cavitation bubble. (ii-iv) Temporal evolution of the remaining bubble. (v) Bright spots represent scatter laser-light due to AgNPs picked up by the video-camera. (vi) Bubble ejection due to the counterjet. The frame rate in all cases was 43,000 fps

Discussion

As pointed out above, no bubbles were produced in the absence of nanoparticles at the fiber end, so the driving mechanism of bubble generation is of thermal origins due to the light absorption by the nanoparticles. Heat is transfer to ethanol from the irradiated zone due to diffusion. The diffusion time is given by[159] $\tau_{diff} = d^2/4D_t$, where d is the thickness of the absorbing medium and D_t is the thermal diffusivity (171.92x10^{-6} m^2/s for silver[160] and 85.19x10^{-9} m^2/s for ethanol[161]). For silver nanoparticles and a thickness of d =100 nm, τ_{diff} ~ 15 ps, which means that within the pulse the films radiate efficiently but ethanol is a bad radiator, so its temperature will increase. It is crucial to determine the temperature increase at the AgNPs-ethanol interface; however, it is quite difficult to perform a direct measure because to our best knowledge, there is no thermal sensor capable of operating at the times scales involved (τ_p <10 ns) in a small heated volume. However, let us take some reasonable assumptions to numerically (COMSOL Multiphysics) estimate both the temperature-induced and its spatial distribution. First, the incident laser pulse has a Gaussian profile and the photodeposited film is assumed to be a homogenous thin-film of constant thickness. The generated heat per unit volume is calculated as $Q = \alpha I$, where α is the absorption coefficient (7.2086x10^6 m^{-1} for silver [161] and 6.8x10^{-2} m^{-1} for ethanol[162]) and I is the optical intensity of the Gaussian beam defined as $I = \left(2E/\pi\tau_p w_0^2\right)\exp\left(\alpha_{Ag} d\right)\exp\left(-2r^2/w_0^2\right)\exp\left(-t^2/\tau_p^2\right)$ where E is the pulse energy, τ_p is the pulse duration and w_0 is the optical fiber core radius. The ethanol´s absorption coefficient is very small in comparison to the silver one; therefore, the silver film is the only heat source. Figure 5.5 shows the temperature profile induced by a single laser pulse at the AgNPs-ethanol interface at different laser pulse’s energy. The energy pulses correspond to the ones used on the experiment. In all cases, the temperature rises quickly beyond the ethanol boiling point [163] T_b = 78.24 °C without boiling and reaching the thermodynamic critical temperature of ethanol [163] T_c = 243°C, i.e., the temperature of the film is so hot that a vapor film is created between film and the liquid limiting further increase on vaporization. Beyond this metastable state, ethanol undergoes an explosive phase transition to vapor, producing a fast-expanding bubble (not included in our simulation). Once the vapor phase is achieved no further heating of the ethanol is possible due to the well-known boiling crisis[94]. On the other hand, once the laser pulse is off, the temperature slowly decreases $T(t) = T_0 + \Delta T exp(-t/\tau_0)$ where T_0 is the ambient temperature, ΔT is the maximum temperature reached by the pulse and τ_0 is characteristic time (~ 55 ns). When the next pulse arrives, 100 μs later, time the film has reached a steady-state temperature, and the whole process repeat again. Thus, with each laser pulse a bubble is produced, and a train of bubbles are expelled from the fiber end. It is important to mention that no phase transition was included in our simulation, so the actual liquid temperature could not be determined.

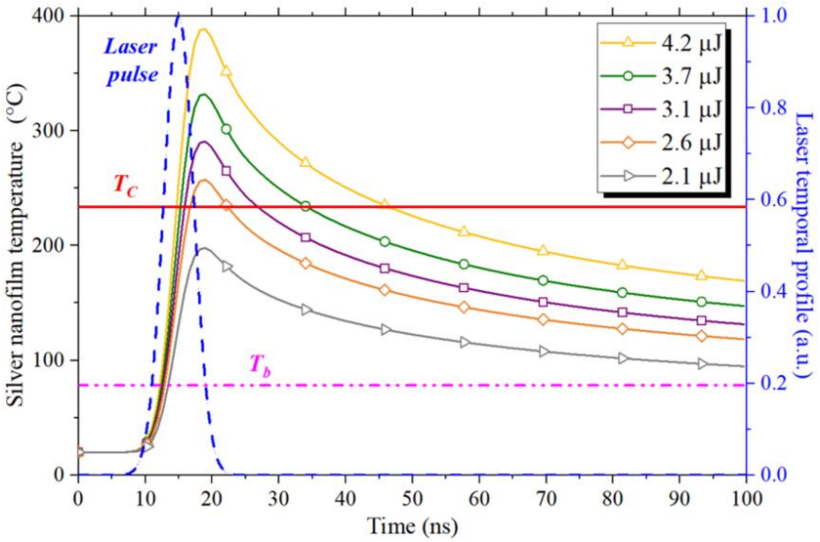

Fig. 5.5 Temperature profile at the AgNPs-ethanol interface obtained by solving the heat diffusion equation coupled to the Navier-Stokes equations using COMSOL Multiphysics. The phase explosion is more likely to occur around T_c ~243 °C (continuous red line). The temperature increase at the interface is a linear function of the laser energy. Color solid lines represent the temporal profile of the temperature at the AgNPs-ethanol interface due to light absorption. The blue broken line represents the temporal profile of one laser pulse. The pink double-dot line represents the pure ethanol boiling temperature T_b ~ 78 °C.

The generation of the column of bubbles just described here was also recently reported using CW lasers and electrical microheaters[53,81]. In their studies, they heat (optically or electrically) a homogenous metallic thin-film and observed rising bubbles at a very high repetition rate ~100 kHz. Upon heating, the liquid in contact with the metallic film is explosively evaporated and after some transient regime, a stable bubble generation is observed. It is well known that a cavitation bubble collapsing near a solid substrate will produce a counterjet explained by the non-spherical collapse theory developed by Rattray[111–113]. Before the collapse, the semi-spherical bubble takes toroidal shape due to the formation of a counterjet directed towards the substrate. In the case of heated substrates, the counterjet hits the film and is immediately vaporized producing a secondary bubble while the vapor film keeps attached to the fiber end and this process repeats with each laser pulse. However, in Ref. 47,144 they neither observe the coalescence nor the trapping of bubbles (probably they occurred outside the field of view), given the smaller bubbles (R ~ 2 μm) and the velocity at which the bubbles are expelled.

In our experiments, we could not observe details of the bubble dynamics because of the limited temporal resolution of our camera. The bubble lifetime τ_r in close proximity to a substrate[113,153,164] is given by[111]:

$$\tau_r \approx \tau_c(1 + 0.205\gamma), \tag{5.1}$$

where $\gamma = H/R_{max}$ is standoff parameter, H is the distance between the wall, the center of the bubble, R_{max} is the maximal semi-spherical radius and τ_c is the collapse time for a spherical bubble, also called the Rayleigh collapse time[91], given by:

$$\tau_c \approx 0.915\sqrt{\frac{\rho_l}{P_\infty - P_v}}R_{max}, \tag{5.2}$$

where ρ_l = 789 kg/m^3 is liquid ethanol density[163], P_∞ = 101.33 kPa and P_v = 7.87 kPa are the pressure in the liquid[165] away from the bubble ($P_\infty = P_{atm}$) and the vapor pressure of ethanol[91], respectively. According to Eq. (5.1), the non-spherical collapse time for the bubbles reported here is τ_r ~ 6 µs, which is smaller than the temporal resolution of our video-camera, τ_{frame} ~ 23 µs. This explains why we cannot record both the counterjet and the bubble collapse dynamics.

As shown in Fig. 5.3(a), the bubbles are expelled from the optical fiber reached velocities of up to 2.5 m/s, much larger compared to those reported in Ref. 47,144, and decrease as they move away from the AgNPs-ethanol interface and eventually they coalesce at a certain distance along the propagation axis producing a larger bubble, which is eventually trapped when it reaches a critical size. An estimate of the critical size is not an easy task, but we can estimate the quasi-steady-state trapping by analyzing the forces involved in its trapping. Two of them are of thermal origin produced by light absorption on the nanoparticles: the Marangoni force and drag force due to convective currents. There are two additional forces: one due to the momentum's transfer to the main-bubble by the continuous coalescence of bubbles and buoyancy force. A bubble immerse into a temperature gradient, as the one produced by the nanoparticles on the fiber end, will suffer a tangential stress on its wall owing to the temperature dependence of the surface tension; the bubble will move towards the heat source while the liquid flows to the colder regions, this is called Marangoni force $\overrightarrow{F_M}$ or thermocapillary force[11,42,150], which is given by:

$$\boldsymbol{F_M} = -2\pi R^2 \boldsymbol{\nabla T}\frac{d\sigma}{dT}, \tag{5.3}$$

where R is the microbubble radius, $\boldsymbol{\nabla T}$ is the temperature gradient in the propagation axis and $d\sigma/dT$ is the derivative of the surface tension of ethanol with respect to temperature σ (-0.1x10^{-3} Nm^{-1}K^{-1}). The drag force[129] due to the convective currents can be written as $\overrightarrow{F_d} = 6\pi\mu RU$. The column of bubbles moves in opposite direction to the main-bubble, as it shows in Fig. 5.2(a). So, the main-bubble suffers an impact from the bubbles-stream, called inertia force[118–120] $\boldsymbol{F_i} = m\boldsymbol{a} = {}^4/_3\,\pi R^3\rho_l C_b\,{}^{\boldsymbol{du}}/_{dt}$, where $C_b = 1/2$ is the bubble-shape coefficient[119]. In addition, once the bubble is created the buoyancy and gravity force appear. These forces are given by[11] $\boldsymbol{F_b} = \frac{4}{3}\pi\rho_l\boldsymbol{g}R^3$ and $\boldsymbol{F_G} = \frac{4}{3}\rho_v\boldsymbol{g}R^3$, respectively, where $\boldsymbol{g}$ is the gravitational acceleration, $\boldsymbol{u}$ is the microbubble velocity, μ = 1.17x10^{-3} Pa·s is the dynamic ethanol viscosity[163], ρ_v = 1.43 kg/m^3 is the vapor ethanol density[163]. However, since the liquid density is two orders of magnitude greater than the vapor density, gravity force will be neglected. On the other hand, since the vapor refractive index (~ 1) is smaller than the liquid one, the bubble will be pushed away from the beam. Actually, given the large size of the beam and optical power, the gradient optical force [129] in this case is five orders smaller than both the drag and buoyancy force[9,141]. The radiation pressure is also negligible small since only the beam leaving the fiber rapidly diffracts [129], so all optical forces are negligibly small and will not be taken into account in the following analysis. In addition, since Marangoni force scale ~ R^2, it means that only the large bubble will be under the effect of this force, for example, a bubble of R = 5 µm near the fiber end will experience $\boldsymbol{F_M}$~ 20 nN while large bubbles of R > 100 µm will experience a force > 400 times larger. Small bubbles cannot be attracted towards the fiber end since the drag force for small bubbles is larger. For example, using the velocity data for small bubbles (Fig. 5.3(a)) moving away from the fiber we calculated drag force $\boldsymbol{F_d}$ ~ 190 nN, i.e., the drag force is almost 20 times larger than the Marangoni force for the small bubbles. On the other hand, a bubble of R = 125 µm close to the fiber end will feel $\boldsymbol{F_M}$ ~ 15 µN and $\boldsymbol{F_d}$ ~ 0.190 µN; therefore, the bubble will be attracted to the fiber end. Hence, the total force $\boldsymbol{F_T}$ acting over the main-bubble moving in the propagation axis ±z used in this study is:

$$\boldsymbol{F_T} = \boldsymbol{F_b} \pm \boldsymbol{F_M} \mp \boldsymbol{F_d} \mp \boldsymbol{F_i}, \tag{5.4}$$

Where the $\pm$ sign indicates the direction of light propagation along ±z, as sketched in Fig. 5.6(a).

Figure 5.6(b) shows the total force over a main-bubble of R = 131 µm versus the distance along the z-axis. When the total force is equal to zero, the bubble will stop, so, $\boldsymbol{F_M} + \boldsymbol{F_b} = \boldsymbol{F_d} + \boldsymbol{F_i}$. Thus, the main-bubble will reach a theoretical quasi-steady-state at z_{crit} = - 439.7 µm, as it is shown in Fig. 5.6(b) inset. Notice that the dominant force near to the fiber is the Marangoni one but the other forces become important, as the main bubble is farther away. If the laser is continuously on, the bubble will continue growing until it touches the fiber and eventually leaves the fiber due to buoyancy force.

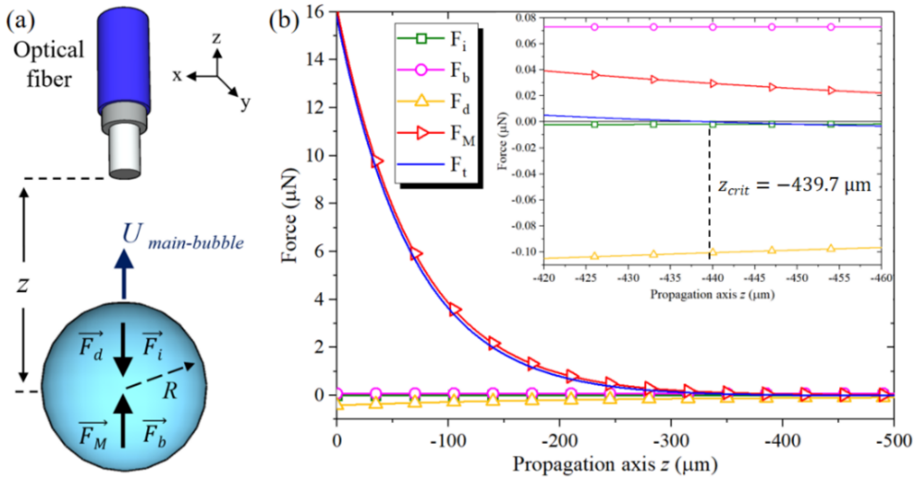

Fig. 5.6 (a) Free-body diagram of the forces involved in the main-bubble manipulation. (b) Total force over a main-bubble of R = 131 µm illuminated with pulses of 3.7 µJ of energy as a function of the propagation axis.

Figure 5.7(a) shows snapshots of a main-bubble of radius R = 131 µm approaching the optical fiber illuminated with pulses of 3.7 µJ of energy. The complete temporal evolution of the main-bubble radius is not shown because it occurred out of the field of view, nevertheless, one can observe the main-bubble displacement in +*z* direction while the bubbles-streams move along the -*z* direction; quasi-steady-state trapping of the main-bubble trapped occurs at z_{exp} = -437.8 µm. However, this position is continuously changing since the main-bubble is continuously growing, as it is shown in Fig. 5.7(b). In this figure, the theoretical-quasi-steady-state is obtained from the total force around the equilibrium position. Although, the rate of change of the bubble is not negligible ~ 30 µm/s, as it is shown in Fig. 5.2(b).

The quasi-steady trapping can be maintained from microseconds to milliseconds, as it is shown in **Visualization 5.1**. In fact, for the case of Fig. 5.7(b) a change in the bubble ratio of 3 µm (occurs in 100 ms) it means a change of ~30 µm in the trapping distance or just above 5% variations. The bubble can be trapped around 20 seconds (as it is shown in **Visualization 5.1**), but it continuously approaches the fiber and eventually leaves the trap since the buoyancy force dominates over all others forces. Nevertheless, these results give us the confidence to predict the trapping distance as a function of pulse-energy and to achieve quasi-steady-state 3D trapping.

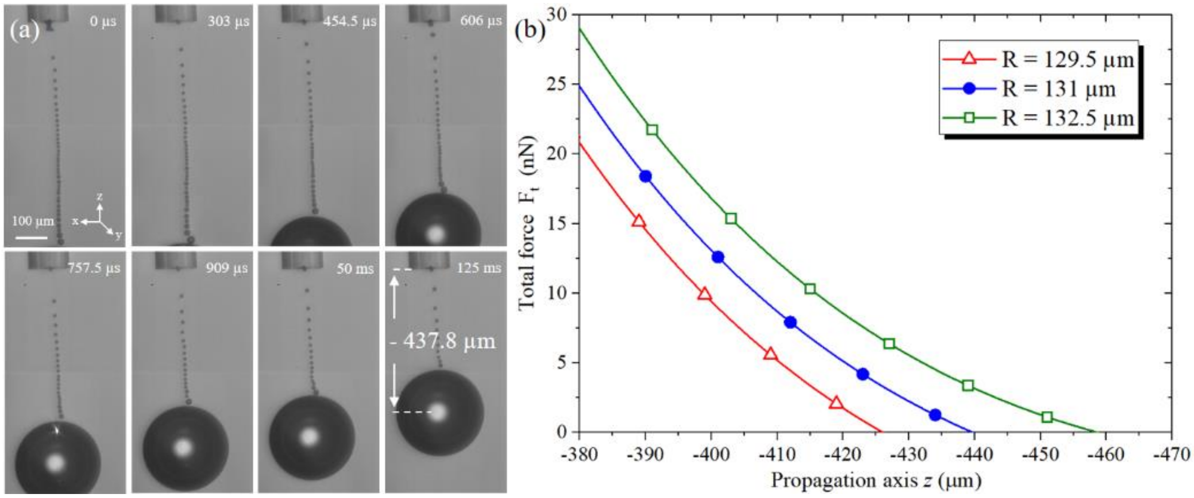

Fig. 5.7 . Spatial displacement of the main-bubble Visualization 5.2. (a) The main-bubble moves in +z direction whereas the bubble stream does it in -z direction. (b) Total force over a main-bubble around the quasi-steady-state trapping distance for particles of different radii. Total force over a bubble of 129.5 µm of radius (red triangles), 131 µm of radius (blue dots) and 132.5 µm of radius (green squares) obtaining quasi-steady-state trapping at -430.2 µm, -439.7 µm and -451.4µm, respectively.

Conclusions

In summary, it was shown both theoretically and experimentally the quasi-steady-state 3D manipulation of vapor bubbles using a nanosecond pulsed laser. Light absorption at silver nanoparticles (AgNPs) photodeposited onto the core of a multimode optical fiber heats the liquid beyond its boiling point. Each laser-pulse generates a small bubble (attached to the fiber end) by the explosive phase transition, which later ejects microbubbles into the liquid, forming a microbubbles-stream that moves away from the tip of the optical fiber until they coalesce, forming a large microbubble. We have shown that those bubbles coalesce at certain distance *z*, generating a large bubble that grows with each coalescence. This bubble is eventually attracted to the optical fiber by the Marangoni force while it is continuously hit and fed by the microbubbles-stream. The balance of the involved forces drives the 3D manipulation of the large bubble. To our best knowledge, this is the first time that both quasi-stable 3D trapping and manipulation of large bubbles are reported.

Chapter 6. Trapping and 3D manipulation of microbubbles by CW laser at low power

Trapping and manipulation of microbubbles have become a very useful tool in various applications such as manipulation of micro-objects[122,123],fabrication of micro-valves[41,121], photolithography[6], among others. There are different techniques for generating, trapping, and manipulating microbubbles in liquids using thermal[12,42,62], acoustic[14,127], and optical effects[7,44,126]. Thermal effects have been considered as an unwanted side effect on optical trapping; however, forces of thermal origin are orders of magnitude greater than optical ones, thus offering plenty of opportunities for the manipulation of micro-objects[122,123]. In fact, generation and 2D trapping of microbubbles using light induced temperature gradient using absorbent thin films deposited on one of the substrates has been demonstrated for several authors[6,166,167]. Later, absorption in the bulk and from nano/microparticles suspended on the liquid were used to achieve thermal trapping and manipulation[12,46,168]. More recently, Benerjee *et al*.[45], reported the trapping and 2D manipulation of bubbles due themal bluming and Marangoni effect triggered by light absorption of a focused CW laser on colloidal particles suspended in isopropanol. However, they require rather large optical powers >100 mW; besides, they did neither show steady-state trapping nor stably manipulation. Recently, our research group has demonstrated both the generation and quasi-steady-state trapping and manipulation of single microbubbles in optical fibers using the Marangoni effect[150,169].

In this chapter, we report the 3D trapping and manipulation of a microbubble through temperature gradients generated by light absorption. Two optical fibers were used: One for bubble generation (OF_G) and the other for trapping and manipulation (OF_T). In the fiber OF_G, light from a Q-switched pulsed laser propagates and gets absorbed at silver nanoparticles, previously photodeposited at the distal end of the fiber optic core, generating the microbubbles. In the second fiber $\mathrm{OF_T}$, the light from a low power CW laser is used to trap and manipulate the bubbles by Marangoni force induced by light absorption in ethanol. The generated microbubble on fiber OF_G migrates toward the fiber OF_T. The equilibrium trapping position around the fiber OF_T is determined by the balance between the buoyancy force ($\boldsymbol{F_b}$), drag force ($\boldsymbol{F_d}$), and the Marangoni force , also known as thermocapillary force ($\boldsymbol{F_M}$). To our best knowledge, this is the first time that 3D stable trapping and manipulation of the microbubble in liquids is reported.

Experimental description

A beam from a pulsed second harmonic laser (λ = 532 nm, τ_p 5 ns, Spectra-Physics Q-switching Model Explorer 532–200-E) is coupled into a multimode optical fiber ($\mathrm{OF_G}$, 50/125 μm), using an aspherical lens with a focal distance of 4.5 mm as shown in Fig. 6.1. Previously, AgNPs were immobilized using the photodeposition technique at the distal end of the fiber OF_G[129,133,170]. The optical power loss caused by AgNPs absorption was approximately 2 dB. When light impinges on the AgNPs, they are heated up well beyond the ethanol's boiling temperature leading to the creation of thermocavitation bubbles[169]. A second laser, continuous wave (CW) laser (λ = 1,550 nm, Thorlabs model SFL1550S, and current controller model CDL1015) with single-mode optical fiber output (OF_T, 9/125 μm) was used for trapping and manipulation of the microbubbles generated at fiber OF_G. No nanoparticles were photodeposited on fiber OF_T; thermal effects were generated by light absorption in the bulk ethanol (ethanol absorption coefficient at λ = 1,550 nm is α ~ 5.63 cm^{-1} or ~166 μm penetration length[163]). The fibers OF_G and OF_T were placed in different configurations inside a 3 ml plastic cuvette.

The visualization of the generation, trapping, and manipulation was done through a 5x microscope objective (Newport M-5X), a white LED, and a Motic3 camera (3 Mpx resolution) connected to a CPU.

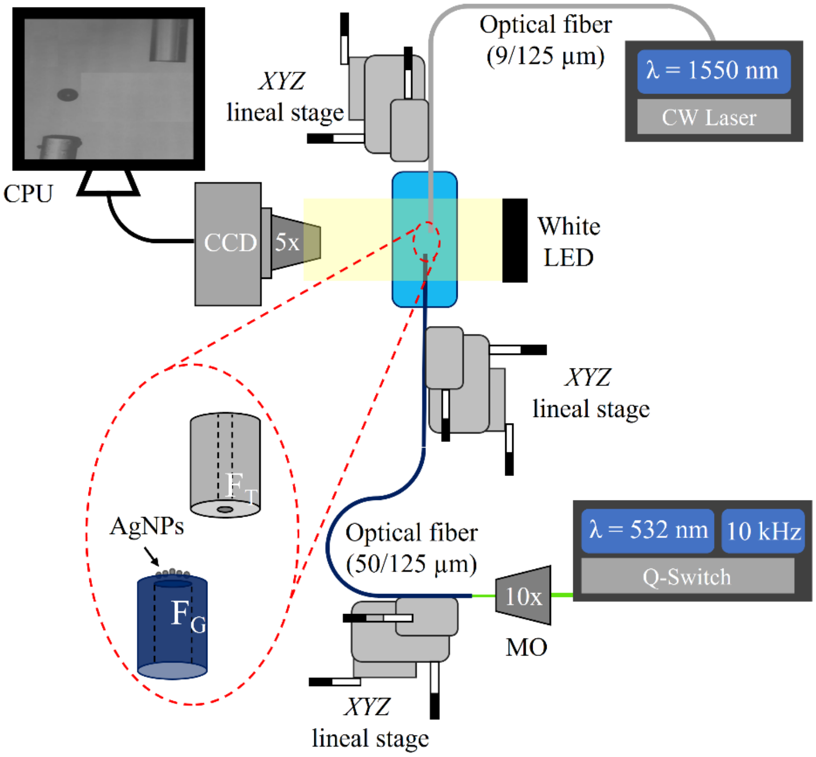

Fig. 6.1 Experimental set up for generation and trapping of microbubbles. The microbubbles are generated at fiber OF_G using a pulsed laser (λ = 532 nm, τ_p = 5 ns) and trapped at fiber OF_T using a CW low power laser (λ = 1550 nm, Power 1–15 mW).

Experimental results

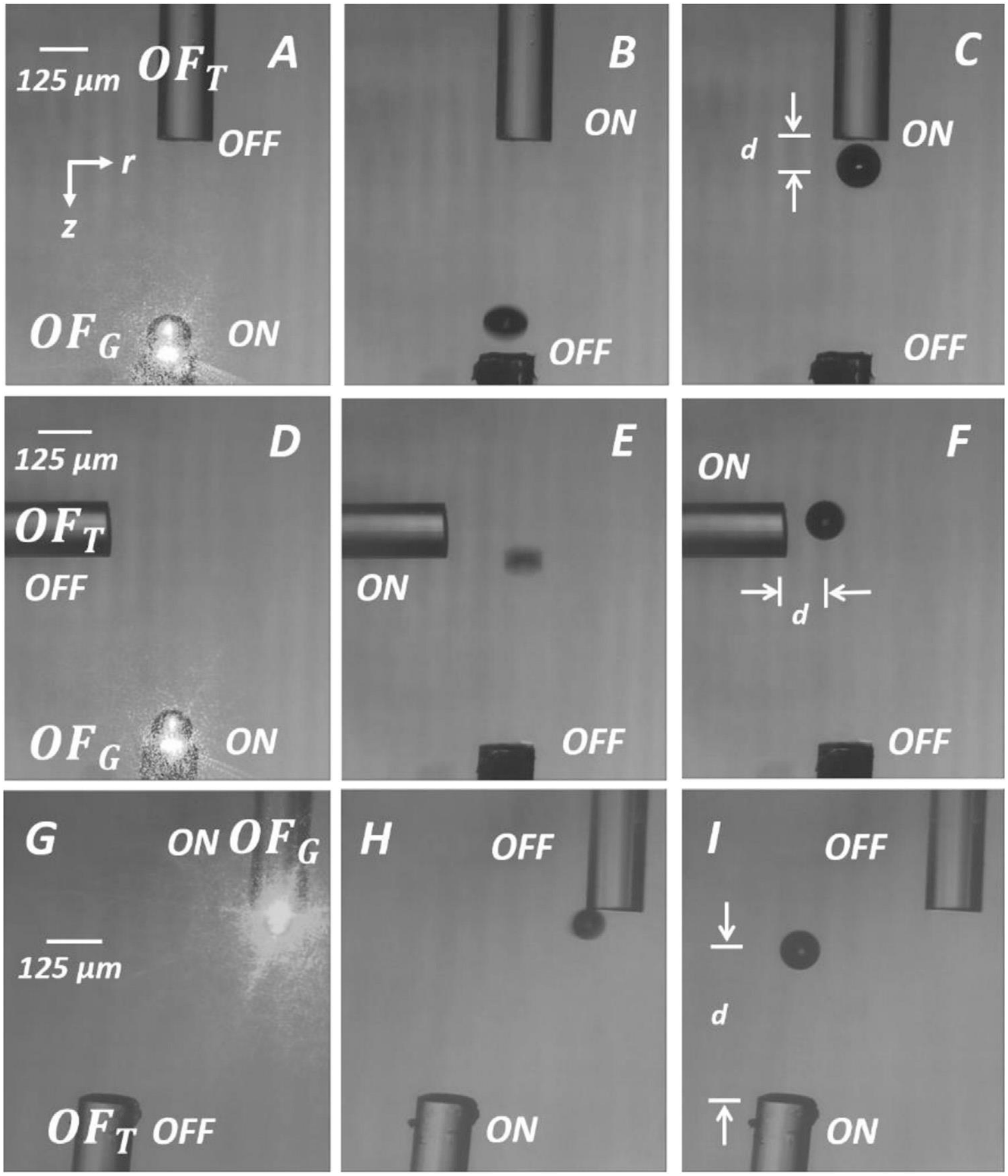

Fig. 6.2 Generation and 3D trapping of a microbubble for different fiber OF_T *positions: facing downwards (A), horizontally 2D, and upwards (G). Bubble release from the fiber* OF_G*: (B), (E), and (H). Bubble trapping (C), (F), and (I). See Visualizations 6.1, 6.2, and 6.3 for more details.*

Figure 6.2 shows the generation and trapping of a microbubble for different fiber OF_T positions (fiber end facing downwards, horizontally, and upwards). The AgNPs strongly absorb light from the laser at 532 nm increasing its temperature. By heat transfer, the surrounding liquid is heated up well beyond its boiling temperature and eventually, evaporates explosively creating a microbubble that is expelled from the fiber end[169]. The longer the pulsed laser is on, the larger the bubble's diameter[169] . In particular, the radius reached by the microbubble was approximately $R \sim 42$ µm for all the cases shown in Figure 6.2. The microbubble ascends through the fluid due to buoyancy, and in minor scale by convective currents, as shown in Figures 6.2(B,E,H). When the bubble leaves the fiber OF_G, the CW laser (λ = 1,550 nm) is turned on heating up the liquid along its propagation path generating a temperature gradient attracting the microbubble toward it. This region is located along the propagation axis of the fiber OF_T, when the forces (Marangoni, drag, and buoyancy) are in equilibrium (see Figures 6.2 (C,F,I)) then the microbubble becomes trapped. The separation distance *d* between the fiber end OF_T and the center of the microbubble when the fiber OF_T was facing downwards, horizontally, and upwards was: ∼75, ∼100, and ∼350 µm, respectively.

The 3D manipulation of a microbubble when the fiber end OF_T was facing downwards, horizontally, and upwards can be seen in **Visualizations 6.1**, **6.2**, and **6.3**, respectively. For each of the cases shown in visualizations, the radius of the microbubble was $R \sim 42$ µm. Note that the bubble follows the fiber OF_T displacements since the temperature gradient moves along with it. When the fiber OF_T is pointing upwards the microbubble is trapped at a greater distance *d*. Trapping is possible for different microbubble radii, as shown in Fig. 6.3.

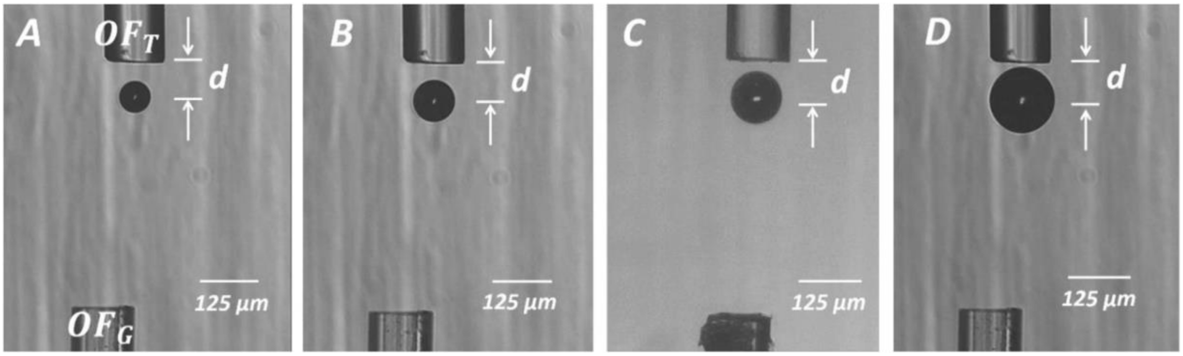

Fig. 6.3 Trapping of microbubbles through a temperature gradient induced with a power of 2 mW for different radii R and its corresponding trapping distance d: (A) R ∼ 32 µm and d ∼ 71 µm, (B) R ∼ 42 and d ∼ 76 µm, (C) R ∼ 50 µm and d ∼ 74 µm, and (D) R ∼ 62 µm and d ∼ 78 µm.

Microbubbles of radius $R \geq 130$ µm get in contact with the fiber OF_T, as one can see in Figures 6.4(A) and 6.4(B). For these large bubbles, trapping becomes unstable and manipulation is not possible. Thus, a good criterion for an upper limit of bubble manipulation is to choose those bubbles whose diameter is comparable with the OF_T's diameter. On the other hand, the lower limit of trapped bubbles size could not determine since bubbles with diameter ≤ 30 µm are very difficult to create as they growths very fast (≤ 100 ms) which comparable to the response time of our mechanical shutter. However, with the proper shutter, the laser could be turned on from µs to ms and, thus, obtaining smaller bubbles.

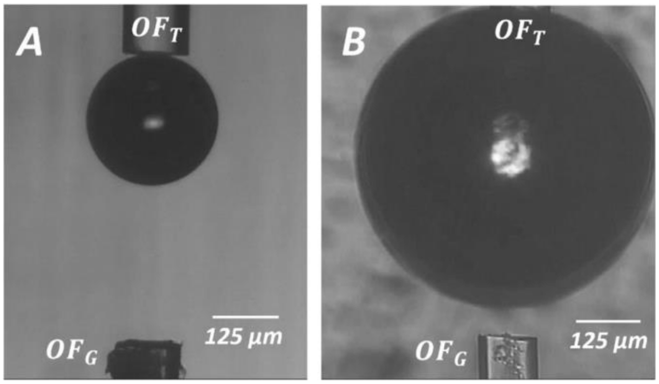

Fig. 6.4 Trapping of microbubbles with a power of 2 mW. Large bubbles touch the optical fiber OF_T (A) R ∼ 130 μm, and (B) R ∼ 333 μm. For microbubbles of radius $R \geq 130$ μm trapping becomes unstable and manipulation is not possible.

Polystyrene microparticles (diameter ∼ 1 μm) were dispersed in ethanol to be used as tracers to measure the velocity of the convective currents induced by light absorption with a power of 2 mW. Figure 6.5 shows the tracking of a cluster of microparticles due to the convective currents and the obtained velocity of these currents along the propagation axis. By video analysis, the velocity of the convective currents around of the optical fiber end (*z* =120 μm) was found to be ~0.64 mm/s in the upward direction. For the largest used power in this work (15mW) and for the same region (*z* = 120 μm), the speed scales almost linearly ~7.7 mm/s.

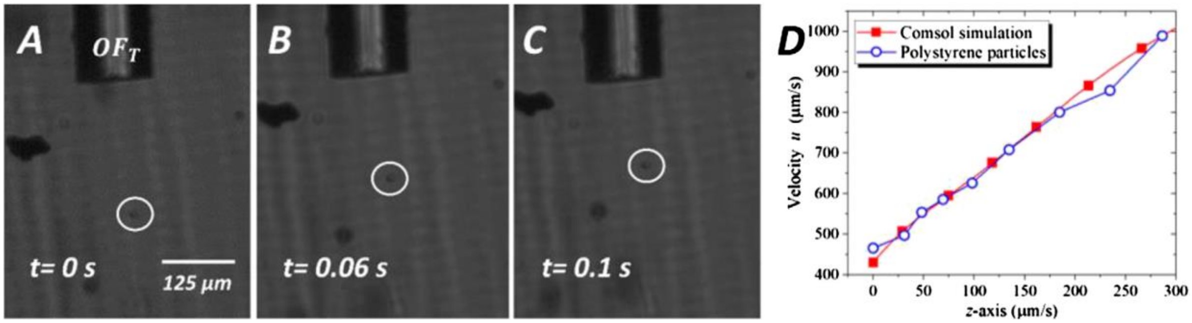

Fig. 6.5 (A–C) Snapshots show that particles move in opposite direction to the beam propagation at a laser power P = 2 mW. White circles indicate the position of a cluster of several polystyrene microparticles. (D) Profile of the convective currents' velocity as a function of propagation distance z measured from the fiber end. Blue dots correspond to the microparticles' velocity whereas red squares correspond to the convective currents obtained from the COMSOL simulation.

Discussion

Experimental results show the trapping and manipulation of microbubbles, previously generated, using optically-induced temperature gradients caused by light absorption in ethanol[163]. Microbubbles are generated in ethanol by thermocavitation, i.e., the explosive phase transition from liquid to vapor around its critical-point (243°C)[105] after light from a pulsed laser is absorbed at AgNPs deposited at the end of an optical fiber. One key characteristic of thermocavitation is that bubbles remain in contact with the interface (in this case fiber end with photodeposited AgNPs) at all times. Upon collapse, the bubble takes a toroidal shape due to a reentrant jet that eventually hits the hot surface and is instantaneously evaporated[105]. This vapor microbubble is expelled from the fiber end with an exponentially decaying velocity as they move away from the fiber. The repetition rate of the laser is 10 kHz, so every 100 μs, a microbubble is expelled from the fiber creating a column of bubbles moving away from the fiber. Since the bubble velocity is continually decreasing, they eventually catch up and coalesce creating a larger continuously growing bubble. Thus, microbubble size, from tens to hundreds of micrometers in diameter, can be precisely generated by controlling the on-time of the laser (or equivalently, the number of pulses)[169]. This continuously growing bubble can be temporally trapped by the same fiber OF_G until it reaches a size such that buoyancy force overcomes the Marangoni force and the bubble leaves the trap. This temporarily trapping last only 55 s. In this work, this bubble is released by turning the pulsed laser off after the bubble reached a certain size and later trapped using another optical fiber with no nanoparticles deposited. This time, the trapping laser is a CW low power laser. The microbubble can be steadily trapped and manipulated for up to10 min. In order to achieve this goal, switch on/off synchronization between the lasers is necessary.

In order to understand the trapping mechanism, we analyze the involved forces using COMSOL Multiphysics 5.2 simulations. Light from the CW laser (λ = 1550 nm) is exponentially attenuated ($\alpha \sim 5.63$ cm^{-1}) inside the ethanol, generating a transversal and longitudinal temperature gradient. Without loss of generalization, we will assume that the trapping fiber is pointing downwards so the microbubble will move up toward the trapping fiber by buoyancy force $\boldsymbol{F_b}$. When it is in close proximity to the temperature gradient, it will experience the Marangoni force $\boldsymbol{F_M}$. Due to the temperature gradient, convective currents are also generated within the fluid creating an additional drag force $\boldsymbol{F_d}$. When the microbubble is trapped, an equilibrium between the buoyancy $\boldsymbol{F_b}$, drag $\boldsymbol{F_d}$, and Marangoni $\boldsymbol{F_M}$ forces is established. The direction of Marangoni's force is always directed toward the heat source while the buoyancy force and drag force, always points upwards. The equilibrium position is located at a distance d, measured from the tip of the fiber OF_T until the bubble geometrical center. Optical forces are not taken into account because their magnitudes are three orders of magnitude smaller than the buoyancy force and six orders of magnitude smaller than the Marangoni force $\boldsymbol{F_M}$[150].

When the light is incident upon the ethanol a portion of it is absorbed by the ethanol, producing a temperature gradient $\boldsymbol{\nabla T}$ that heats the ethanol up according to the heat transfer equation (where a steady-state condition is assumed) is given by[78]:

$$\rho c_p \boldsymbol{u} \cdot \boldsymbol{\nabla T} = \boldsymbol{\nabla} \cdot (\mathrm{K} \boldsymbol{\nabla T}) + Q, \tag{6.1}$$

where ρ is the ethanol density, C_p is the heat capacity, $\boldsymbol{u}$ is the fluid´s field velocity, k is the thermal conductivity, and $Q = \alpha I$ is the heat source per volume unit with α the absorption coefficient and I the optical intensity of the Gaussian beam. To model the fluid´s field velocity, both the heat transfer equation given by Eq. 6.1 and the Navier-Stokes equations for incompressible fluids, given by Eq. 6.2, and Eq. 6.3, are solved by finite element method (Comsol Multiphysics).

$$\rho(\boldsymbol{u}\cdot\boldsymbol{\nabla})\boldsymbol{u} = \boldsymbol{\nabla}\cdot[-pH + \mu(\nabla\boldsymbol{u} + (\nabla\boldsymbol{u})^T)] + \boldsymbol{F}, \tag{6.2}$$

$$\rho\boldsymbol{\nabla}\cdot\boldsymbol{u} = 0, \tag{6.3}$$

where H is the identity matrix, μ is the ethanol viscosity, and $\boldsymbol{F}$ is the volumetric force per volume unit defined as $\boldsymbol{F} = \boldsymbol{g}(\rho - \rho_0)$ where $\boldsymbol{g}$ is the gravitational acceleration, ρ is the ethanol density at temperature T, and ρ_0 = 789 Kg/m^3 is the ethanol density at room temperature.

The simulation was carried out assuming a 2D configuration given the geometry of the problem, non-slip boundary condition, and initial room temperature in all boundaries. We use an inhomogeneous mesh been finer in the vicinity of the optical fiber (element size = 1.5 μm) in order to reduce the computing time. We considered a Gaussian laser beam whose spot corresponds to the fiber core radius ω_0 = 4.5 μm, the absorption coefficient of ethanol of α = 5.63 cm^{-1}, a cuvette with square geometry of width 1 mm, and height 5 mm. The origin of the coordinate system is set at the optical fiber end. The cuvette used in the experiments is much larger than the cuvette used in the simulation but the results (temperature and liquid's velocity) do not change much (~2%) respect to real cuvette. We prefer to keep the small container for the sake of computational time.

Figure 6.6 shows the spatial temperature distribution induced by a 2 mW power laser. As expected, the temperature increases as it travels inside the liquid, reaches a peak, and eventually decreases exponentially according to Beer-Lambert law to room temperature for $z \geq 2$ mm. Figure 6.6(B) shows the temperature distribution along the propagation distance for different optical powers showing the same general behavior. Note the abrupt rise of the temperature from room temperature until the peak one which occurs at a distance $z_{HT} \sim 75.4$ μm independently of the laser power (but determined by the absorption coefficient). Note that the temperature increases linearly with the power from ~3.4 K for 2 mW to ~ 26.8 K for the highest power of 15 mW. Figure 6.6(C) show the transverse temperature profile at the highest temperature (i.e. z_{HT} = 75.4 μm) with a spatial profile much wider than the Gaussian beam one as consequence of heat diffusion. Finally, Figure 6.6(D) shows the velocity of the convective currents generated within the ethanol with an optical power of 2 mW. The convective currents peak velocity is about 0.7 mm/s (around $z \sim 440$ μm) in concordance with the measured velocity (see Figure 6.7). The associated drag force $\boldsymbol{F_d}$ exerted on the bubble is given by:

$$\boldsymbol{F_d} = -6\pi\mu R\boldsymbol{u}, \tag{6.4}$$

where $\mu = 1.17 \text{ x } 10^{-3} Pa\cdot s$ [163]. For an optical power of 2 mW, the peak drag force is ~ 0.1 nN, i.e. an order of magnitude smaller than the buoyancy force. However, when the highest power is used (15 mW), the drag force is comparable to the buoyancy force and cannot longer be neglected.

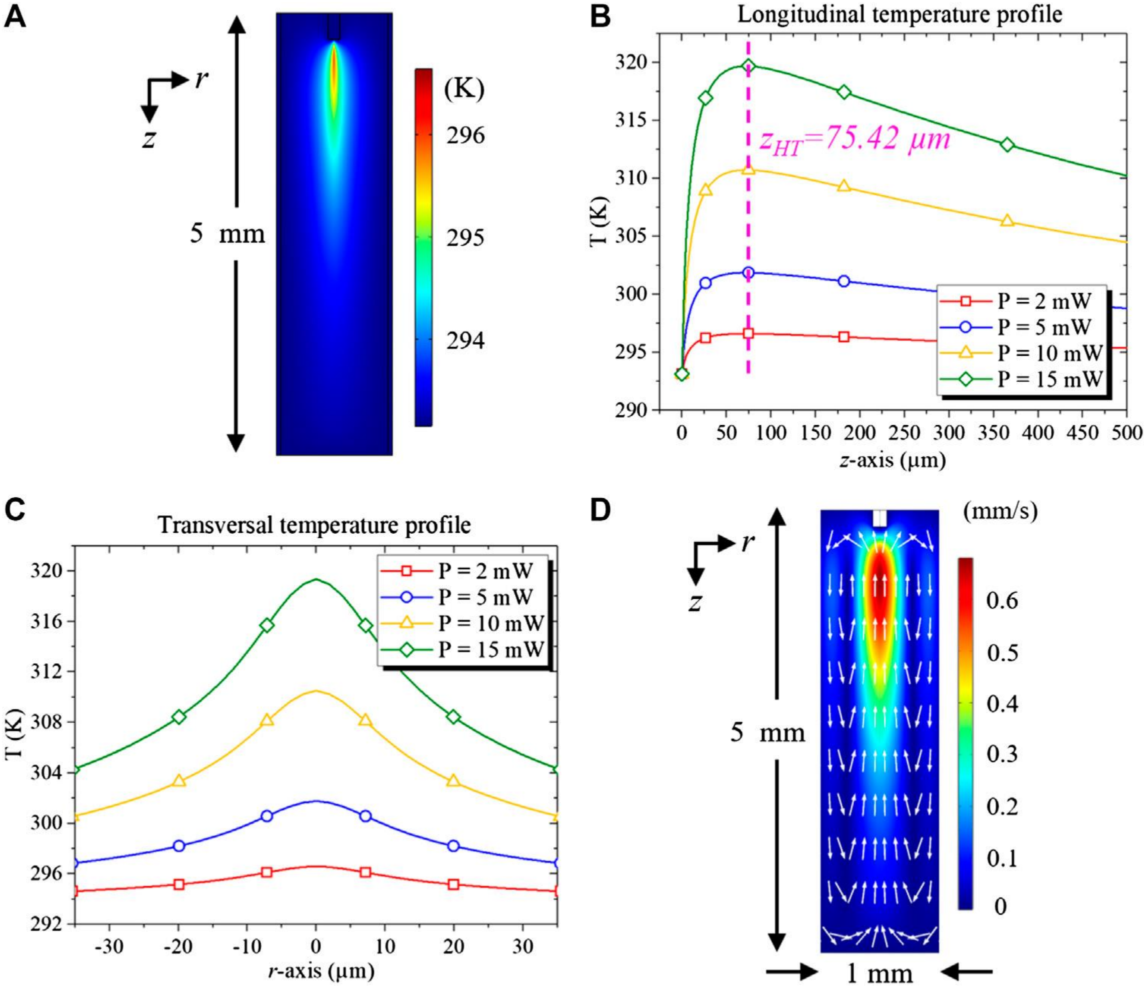

Fig. 6.6 (A) Temperature distribution on ethanol due to light absorption for a power of 2 mW, (B) longitudinal temperature profile on the propagation axis z for several powers, (C) transverse temperature profile on z_{TH} =75.4 μm, and (D) convective currents velocity produced by the temperature gradient with an optical power of 2 mW.

As Fig. 6.7(A) shows, the longitudinal temperature gradient profile obtained from COMSOL Multiphysics is quite steep before ∼75.4 μm and after this point, the gradient is small but sufficiently large as to attract the bubble to the fiber. Note that all temperature gradients change sign at the same distance z_{HT} ∼ 75.4 μm as shown in Fig. 6.7(B). The temperature gradient shows great similarity to the optical gradient present in optical traps. In fact, the transversal and longitudinal temperature gradient result in a Marangoni force that traps the bubble in three dimensions, just as in optical trapping.

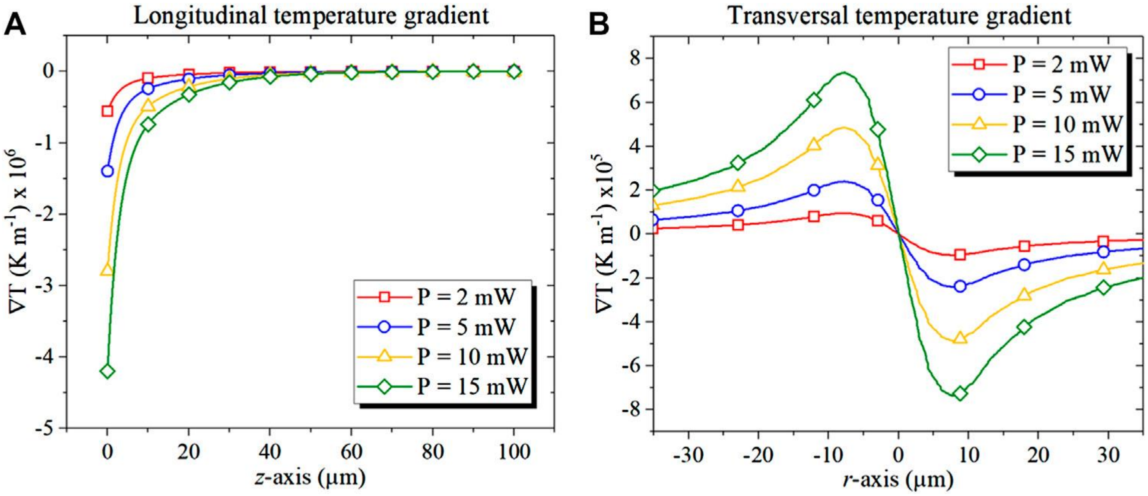

Fig. 6.7 (A) Longitudinal gradient temperature profile along the propagation axis z and (B) transversal gradient temperature profile obtained at $z_{HT} \sim$ 5.4 μm, for 2, 5, 10, and 15 mW obtained through simulation in COMSOL Multiphysics.

In the Marangoni force, a tangential stress on the bubble's wall owing to the temperature dependence of the surface tension is exerted; the bubble will move toward the heat source while the liquid flows to the colder regions with a force given by[11,150]:

$$\boldsymbol{F_M} = -2\pi R^2 \nabla T \frac{d\sigma}{dT}, \tag{6.5}$$

where $\frac{d\sigma}{dT}$ is the temperature derivative of the surface tension of the liquid σ (-0.022 Nm^{-1})[171]. The buoyancy force$\boldsymbol{F_b}$ which is given by:

$$\boldsymbol{F_b} = \frac{4}{3}\pi\rho_0 \boldsymbol{g} R^3, \tag{6.6}$$

where $\rho_0 = 789 Kg/m^3$ is the density of the liquid (ethanol)[171]. The total force $\boldsymbol{F_T}$ experienced by a trapped microbubble used in this study is:

$$\boldsymbol{F_T} = \pm\boldsymbol{F_M} + \boldsymbol{F_b} \mp \boldsymbol{F_d}, \tag{6.7}$$

where the ± sign indicates if the fiber is pointing upwards or downwards, respectively.

From Fig. 6.7(B) and Eq. 6.7 we know that the bubble will be trapped transversally around $r = 0$, so let's analyze where the equilibrium position along z is located. Figure 6.8 shows the longitudinal total force. As expected, the Marangoni force is predominantly close to the optical fiber end where the temperature gradient is larger. When the total force $\boldsymbol{F_T}$ on the microbubble is equal to zero the microbubble will be trapped. The total longitudinal force for an optical power of 2 mW and microbubbles radius of 32, 42, 50, and 62 µm is zero at *z* ~ 77, 73, 70.5, and 68 µm, respectively (see Figure 6.8) which are very close to those measured (71 –78 µm obtained from Fig. 6.3). As the power increases, the contribution of the drag force becomes comparable to the buoyance force and therefore the trapping distance decreases. One possible explanation for the disagreement between theory and experiment, rely on the fact that our simulation did not include the presence of the bubble. In addition, when the microbubble interacts with the beam laser there is an additional temperature profile that appears on the opposite (exit) surface of the microbubble that modifies the net temperature gradient. Since the Rayleigh distance for the trapping beam is ~41 µm, as the beam diffracts, the additional thermal gradient is stronger for smaller than larger bubbles (as seen in Fig. 6.2). Nevertheless, this simple model explains reasonably well all the experiments reported.

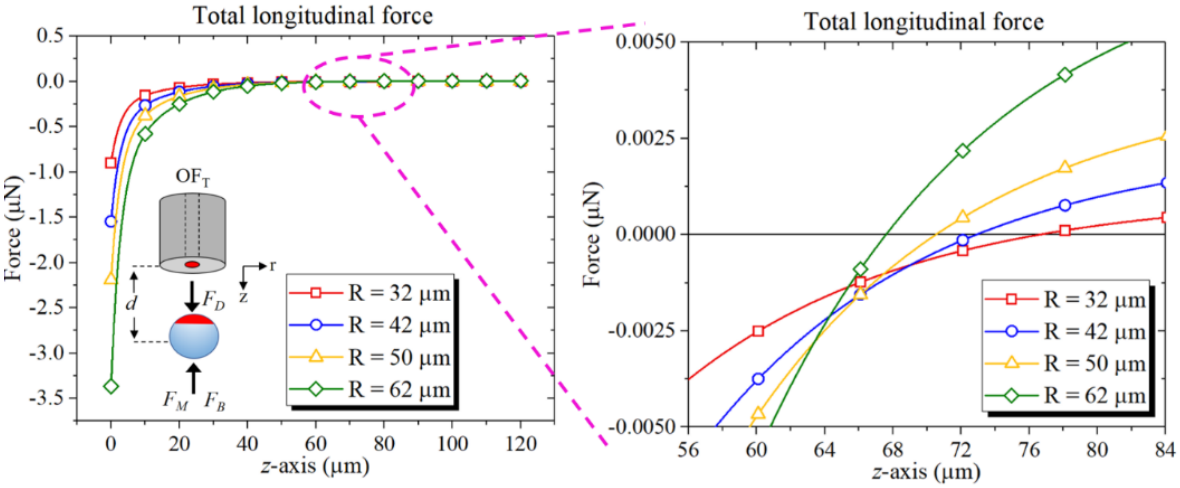

Fig. 6.8 Total longitudinal force using Eq. 6.7 for microbubble with radii ~32, ~42, ~50, and ~62 µm. The zero crossing displaces to the smaller distances z as the convective current increases as discussed in the main text.

In our previous work, we reported quasi-steady-state trapping for milliseconds up to 55 s before the bubble become so large that buoyancy dominates over all forces escaping the trap[169]. Here using CW low power laser, we can extend the trapping time depending on the power used. For example, if a microbubble is trapped with a power 1–2 mW, the rate of vapor condensation exceeds that of evaporation and therefore the bubble will shrink over time. For a power of 1mW, the microbubble decreases at a rate of ~2.3 and ~0.96 µm/s for 2 mW. However, if the microbubble is trapped with a power ~3 mW, it increases its radius overtime at a rate of ~0.53 µm/s. Therefore, by fine-tuning the optical power it is possible to maintain an approximately constant (~>1 µm/min) size microbubble. For instance, in this work was possible to trap a microbubble of *R* ~ 75 µm for an approximately 10 min with an optical power of approximately 2.7 mW. During this time, the microbubble increased in size by 10%. We believe the trapping time can be further extended if the laser beam is intensity-modulated, for example with a square pulse, in order to achieve a balance of the rates of evaporation and condensation.

Conclusions

In summary, we show for the first time, stable 3D trapping and the manipulation of microbubbles in absorbing liquids using a low power CW laser (λ = 1,550 nm). Light absorption activates several phenomena (Marangoni effects, convective currents, and buoyancy), each one producing competing forces: the Marangoni $\boldsymbol{F_M}$, drag force $\boldsymbol{F_d}$, and the buoyancy $\boldsymbol{F_b}$ forces. The large 3D thermal gradient produced by the low power laser but rather modest temperature increase provides the Marangoni force while the others affect the final trapping position along the propagation distance. A careful balance of vapor condensation and evaporation rate induced by the trapping laser produce stably trapping for up to 10 min using an optical power as low as 2.7 mW. The setup could further simplified if the bubbles are generated by Joule heating as it is commonly done in sonocavitation experiments. This work opens up applications for trapping and 3D manipulation of microbubbles using thermal effects in the same way as optical trapping does. We foresee interesting applications in fields such as microfluidics for flow control, nanoparticle trapping, photolithography, among others.

Chapter 7. 3D steady-state trapping and manipulation of microbubbles by the Marangoni force

Since the Nobel laureate Arthur Ashkin introduced optical tweezers[7], it triggered a research race for developing and improving a non-contact/non-invasive mechanisms to trap and manipulate not only dielectric [117] and metallic [21] particles, but also biological matter [17]. Even though optical tweezers have extended their landscape of contactless trapping and manipulation, it remains a challenge to trap particles with refractive index np smaller than the surrounding medium nm, i.e., np/nm < 1, such as microbubbles [9]. This is due to the repelling optical gradient force that pushes the microbubble out of the high-intensity region of the laser beam [16]. However, this challenge has been faced by several trapping approaches where small bubbles have been 3D trapped using Laguerre-Gaussian beams [44], also called bottle beams, by fast scanning Gaussian-based optical tweezers that act as effective bottle beams[77], and using ultrashort laser pulses at a high repetition rate [172]. In addition, 2D trapping approaches using optical, convective, and thermocapillary have been also implemented but are limited to microbubbles/particles with radii < 10-20 µm[75,173,174].

Thermocapillary effects have emerged as an efficient and straightforward tool to accomplish non-invasive trapping and 3D manipulation of microbubbles up to 130 µm of radius[169]. Moreover, the thermocapillary effect can induce larger and long-range forces than the optical ones while maintaining the accuracy of spatial control of microbubbles[42,46,47,150,169,175,17642,45–47,176]. Thermophoresis[177–179], which refers to the motion particles in response to a temperature gradient, has been used to manipulate molecules and even colloidal particles but to our best knowledge do not apply to bubbles. Optical forces magnitude typically lies in the range of fN to pN[173] so trapping large microparticles without damage remains a challenge. In order to trap large objects, several approaches have been demonstrated such as opto-thermally induced forces, which are many orders of magnitude larger than optical ones[87,166,180].

In this chapter, we show both 3D steady-state trapping and manipulation of vapor bubbles in liquids using a low-power CW laser through the Marangoni effect. Using light absorption from photodeposited silver nanoparticles (AgNPs) on the distal end of an optical fiber or light bulk absorption, we created thermal sources that spatially modulate the surface tension of the bubble wall creating a longitudinal and transversal force just like optical forces, effectively creating a 3D potential well. Using numerical simulations, we obtain the expression for the temperature profiles and present an analytical expression for the 3D Marangoni force.

Experimental description

The microbubble was generated by evaporating the ethanol in contact with AgNPs previously photodeposited[129] on one end of the multi-mode optical fiber (OF_1) with an internal and external diameter of 105/125 µm, respectively. Light from a CW laser emitting at 445 nm (BWTEK model BWF1 - 445 - 450) and propagating through the OF_1 was used to heat up the AgNPs and evaporate the liquid. Two additional single-mode fibers (OF_2 and OF_3, 9/125 µm) with also previously photodeposited AgNPs were coupled to two CW lasers emitting 980 nm (Thorlabs model BL976 - SAG300, 5 mW) and 1,550 nm (Thorlabs model SFL-1550S, 4 mW).

The distal ends of the three optical fibers were immersed in a glass cell filled with pure ethanol and separated ~ 800 µm from each other. To visualize the generation and manipulation of the bubble a 5x microscope objective was used and a Motic3 camera (3 Mpx resolution) connected to a computer. The illumination was provided by a white lamp, as depicted in Fig. 7.1.

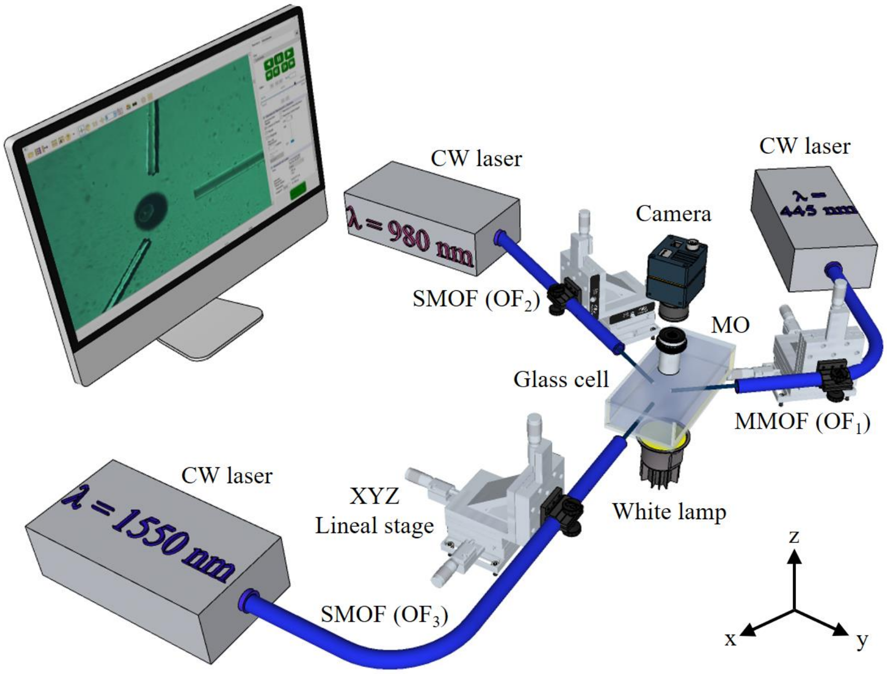

Fig. 7.1 Experimental setup for the generation and manipulation of microbubbles. Three CW lasers with optical fiber output: multi-mode optical fiber (MMOF) for 445 nm and single-mode optical fiber (SMOF) for 980 nm and 1550 nm. The distal ends of the three optic of the three optical fibers are horizontally placed into a glass cell filled with ethanol. Bubbles manipulation is viewed with a Motic3 camera coupled to a 5x microscope objective (MO).

Experimental results

Figure 7.2 shows snapshots extracted from Visualization 7.2 concerning of a vapor microbubble manipulation. The microbubble can be trapped and transferred from one fiber to the next by sequentially switching on and off the CW lasers.

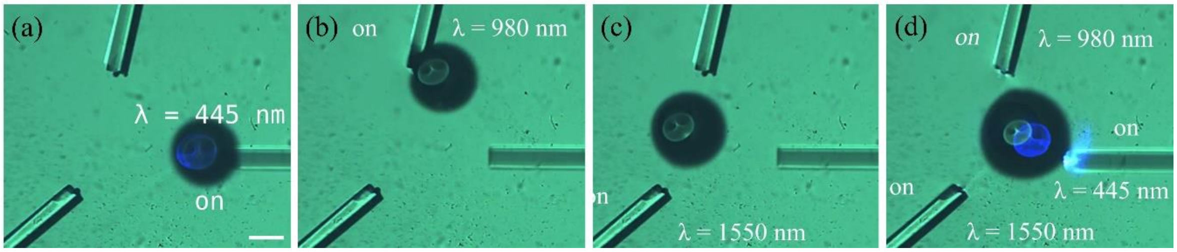

Fig. 7.2 Trapping and manipulation of a microbubble of R = 100 µm by optothermal effects induced at a different wavelength with low optical powers. The microbubble is photothermally generated by the CW laser at 445 nm with 13 mW (not shown). (a) Only the CW laser at 445 mW is turned on, inducing the microbubble trapping by the MMOF (OF_1). The scale bar represents 200 µm. (b) The CW laser at 445 nm is turn off and only the CW laser at 980 nm is turned on, inducing the microbubble displacement towards the SMOF (OF_2). (c) The CW laser at 980 nm is turn off and only the CW laser at 1550 nm is turned on, inducing the microbubble displacement towards the SMOF (OF_3). (d) The three CW lasers are turn on, trapping the microbubble at the center of the optical fiber array (see Visualization 7.1).

Discussion

COMSOL Multiphysics software was used to simulate the light absorption at the AgNPs film previously photodeposited on the distal end of three different optical fibers using three different lasers (α_{Ag}= 638.2 x103 cm^{-1}, 846.3 x103 cm^{-1}, 871.6 x103 cm^{-1} at λ = 445 nm, 980 nm, and 1,550 nm, respectively[181]). Light absorption increases the temperature of the AgNPs and by heat diffusion, it heats up the surrounding liquid (ethanol) according to the heat transfer equation given by[179]:

$$\rho c_p \boldsymbol{u} \cdot \boldsymbol{\nabla T} = \boldsymbol{\nabla} \cdot (\mathrm{K}\boldsymbol{\nabla T}) + Q, \tag{7.1}$$

were ρ is the ethanol density, c_p is the ethanol heat capacity, $\boldsymbol{u}$ is the field velocity of the fluid, K is the thermal conductivity, and $Q = \alpha I_0$ is the heat source per volume unit with α the absorption coefficient and I_0 is the optical intensity of the Gaussian beam. Equation (7.1) assumed a steady-state condition. To model the field velocity of the fluid, i.e., convective currents, the Navier-Stokes equation for incompressible flow, Eqs. (7.2) and (7.3), were coupled to the heat transfer equation and solved by finite element method:

$$\rho(\boldsymbol{u} \cdot \boldsymbol{\nabla})\boldsymbol{u} = \boldsymbol{\nabla} \cdot [-pH + \mu(\nabla \boldsymbol{u} + (\nabla \boldsymbol{u})^T)] + \boldsymbol{F}, \tag{7.2}$$

$$\rho \boldsymbol{\nabla} \cdot \boldsymbol{u} = 0, \tag{7.3}$$

where $\boldsymbol{I}$ is the identity matrix, μ = 1.17 x 10-3 Pa·s[169] is the ethanol viscosity, and $\boldsymbol{F}_b = -\boldsymbol{g}(\rho(T) - \rho)$ is the volumetric force per volume unit where $\boldsymbol{g}$ is the gravitational acceleration, $\rho(T)$ represents the ethanol density as a function of the temperature, and ρ =

789 kg/m^3 is the ethanol density at room temperature[169] . The simulation was carried out assuming a 2D configuration given the problem symmetry. The glass cell possesses rectangular geometry (height 5 mm and width 2 mm). The coordinate system origin is set at the center of the distal end of the optical fiber, as shown in Fig. 7.1(a). Besides, initial room temperature (293.15 K) in all boundaries and non-slip boundary conditions were assumed. We model the laser radiation leaving the fiber as a Gaussian beam whose waist ($\omega_0 = 52.5\ \mu m$) corresponds to the core radius of the multi-mode optical fiber (MMOF) with 15 mW of optical power. Let's consider first that no nanoparticles were photodeposited on the fiber tip and that infrared light (λ = 1,550nm) propagates along the fiber.

In this case bulk absorption ($\alpha \sim$ 5.63 cm^{-1}) heats up the ethanol producing a spatially varying temperature distribution. From the COMSOL simulation (see Fig. 7.3(a)), a Gaussian function and a growth/exponential decay function were found to describe very well the transversal and longitudinal temperature distribution profile, respectively. The transversal temperature profile has the form:

$$T_r(r,z,P) = T_0 + \Delta T_r(z,P)\exp\left[-\frac{1}{2}\left(\frac{r}{r_0(z,P)}\right)^2\right], \qquad (7.4)$$

where r is the transversal radial coordinate, z is the axial coordinate, $\Delta T_r(z,P)$ is the temperature difference between the maximum temperature and the offset temperature T_0 (which is approximately the room temperature for mW power levels) and depends on the optical power P and the distance z from the fiber tip, finally, $r_0(z,P)$ is the characteristic distance at which the temperature decays to e^{-1} from its peak.

On the other hand, the longitudinal temperature distribution has the form:

$$T_z(z,P) = T_0 + \Delta T_{z1}(P)\left(1 - exp\left(^{-z}/_{z_1}\right)\right) - \Delta T_{z2}\left(1 - exp\left(^{-z}/_{z_2}\right)\right), \qquad (7.5)$$

where $\Delta T_{z1,2}(P)$ represents the temperature difference between the maximum temperature and the offset temperature T_0, and $z_{1,2}$ are characteristics distances representing the increase and decrease of the temperature profile.

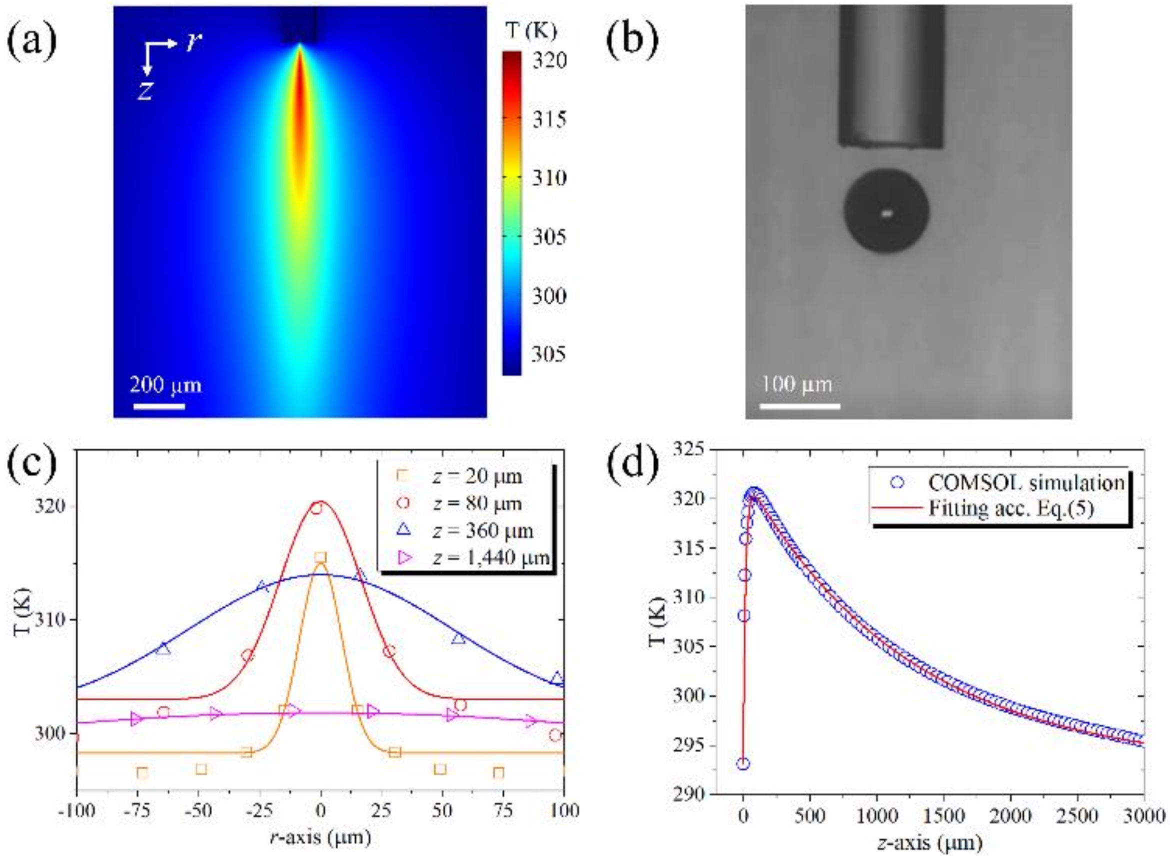

Fig. 7.3 (a) Temperature distribution in ethanol due to bulk absorption extracted from COMSOL simulations (λ = 1,550 nm & 15 mW of optical power). The scale bar represents 200 µm. (b) 3D trapping and manipulation of a bubble of radius R = 50 µm, at λ = 1,550 nm and 15 mW. The scale bar represents 100 µm. See Visualization 7.2. (c) Transversal temperature distribution obtained at different positions along the z-axis. Continuous lines are fits to Gaussian functions Eq. (7.4). (d) Longitudinal temperature profile along the propagation axis z. The red line is fitted to Eq. (7.5).

Figures 7.3(c) and 7.3(d) shows the transversal and longitudinal temperature distribution obtained from COMSOL and the fitting to the Eqs. (7.4) and (7.5). When absorption from the AgNPs is considered, similar expressions are obtained for the transversal temperature but for the longitudinal one, only the decaying exponential function is present. As can be seen, both equations reproduce pretty well the simulated results. The temperature distribution discussed above will affect the surface tension of any bubble in the vicinity of the fiber tip and thus, will be subject to the Marangoni force $\boldsymbol{F_M}$. This force involves tangential stress on the bubble´s wall triggered by the surface tension gradient. The bubble will move towards the zone of the lowest surface tension, i.e., the highest temperature gradient spot. The Marangoni force is given by[169]:

$$\boldsymbol{F_M} = -2\pi R^2 \boldsymbol{\nabla T} \frac{d\sigma}{dT}, \tag{7.6}$$

where $d\sigma/dT = -0.1x10^{-3}\ Nm^{-1}K^{-1}$represents the temperature derivative of ethanol surface tension[169], R is the bubble radius, and $\boldsymbol{\nabla}T$ is the temperature gradient. As Eqs. (7.4) and (7.5) indicates, there is a radial and longitudinal temperature gradient and therefore a gradient and longitudinal Marangoni force on the bubble given by:

$$\boldsymbol{F}_{\boldsymbol{M_r}} = 2\pi R^2 \frac{d\sigma}{dT}\left(\frac{\Delta T_t(z,P)}{r_0(z,P)^2}\right) r exp\left[-\frac{1}{2}\left(\frac{r}{r_0(z,P)}\right)^2\right], \tag{7.6}$$

$$\boldsymbol{F}_{\boldsymbol{M_r}} = 2\pi R^2 \frac{d\sigma}{dT}\left\{\left(\frac{\Delta T_{z1}}{z_1}\right) exp\left(-{}^{z}/_{z_1}\right) - \left(\frac{\Delta T_{z2}}{z_2}\right) exp\left(-{}^{z}/_{z_2}\right)\right\}, \tag{7.7}$$

therefore, 3D trapping of the bubble is expected as shown in Fig. 7.4(b). Figure 4.5(a) shows the transversal Marangoni force $\boldsymbol{F}_{\boldsymbol{M_r}}$ from Eq. (7.7) taken at z = 80 μm, indicating a force profile similar to the optical transversal gradient force, i.e. bubble displacement along ± r will produce a restoring force directed towards $r = 0$.

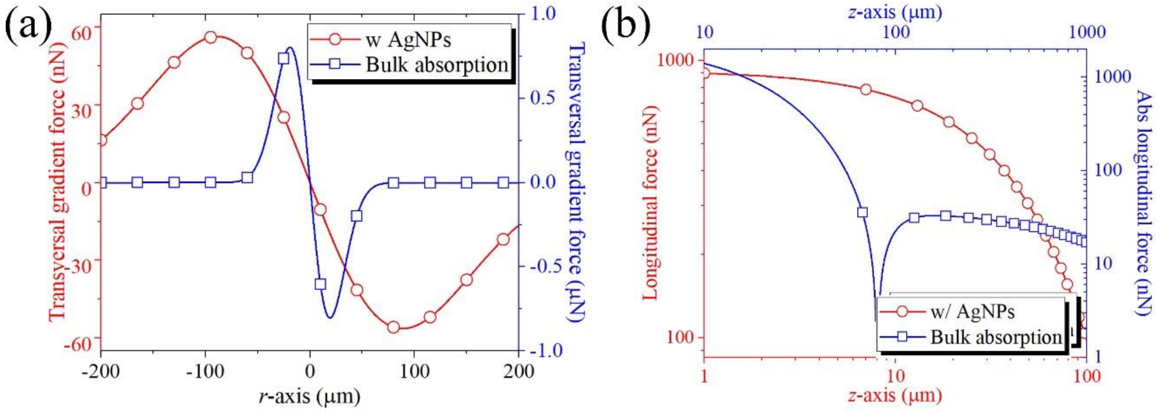

Fig. 7.4 Marangoni force over a bubble of R = 50 μm induced by light bulk absorption of ethanol (blue) and by light absorption from AgNPs photodeposited on the core of an optical fiber (red). (a) Transversal Marangoni force measured at z = 80 μm from the fiber tip. (b) Longitudinal Marangoni force.

Note that the magnitude of both force components depend, among other factors, on the ratio of the temperature increase and the extend of the temperature distribution. Similarly, Fig. 7.4(b) shows the longitudinal Marangoni force. Note that for bulk absorption, the Marangoni force is negative i.e. the bubble is being repelled for z < 80 μm and attracted for z > 80 μ m so the bubble is steadily trapped z ~ 80 μm. On the other hand, for AgNPs deposited on the fiber tip the bubble will always be trapped on the fiber tip. For bulk absorption the distance where bubble will be trapped depends on the absorption coefficient, the larger the absorption coefficient the smaller the distance to the fiber tip. Note that the Marangoni force magnitude lies in the nN- μN range.

The coupling between Eqs. (7.1), (7.2), and (7.3) leads to convective currents as shown in Fig. 7.5(a), which in turn, results in a drag force $\boldsymbol{F_d} = 6\pi\mu R\boldsymbol{u}(r,z)$, where $\mu = 1.071x10^{-3}\ Pa \cdot s$ is the dynamic ethanol viscosity[169] and where we emphasize the spatial dependence of the velocity field. It has been proposed that convective currents may exert an additional force that adds up the trapping force[179]. Similarly, we can decompose the drag force into two orthogonal components: transversal and longitudinal. The transversal force shows similar behavior to the transversal Marangoni force discussed above, so the bubble will be trapped preferably along the propagation distance. Figure 7.5(c) shows the longitudinal drag force along the z-axis due to light absorption from AgNPs for a bubble of R = 50 µm. Notice that although the fluid velocity magnitude is ~2mm/s, the drag force associated with it will produce a maximal force of ~2 nN directed towards the fiber. Figure 7.5(d) shows the longitudinal drag force along the z-axis due to light bulk absorption for the same bubble. Since the longitudinal velocity is directed towards the fiber tip, the drag force will push the bubble towards it.

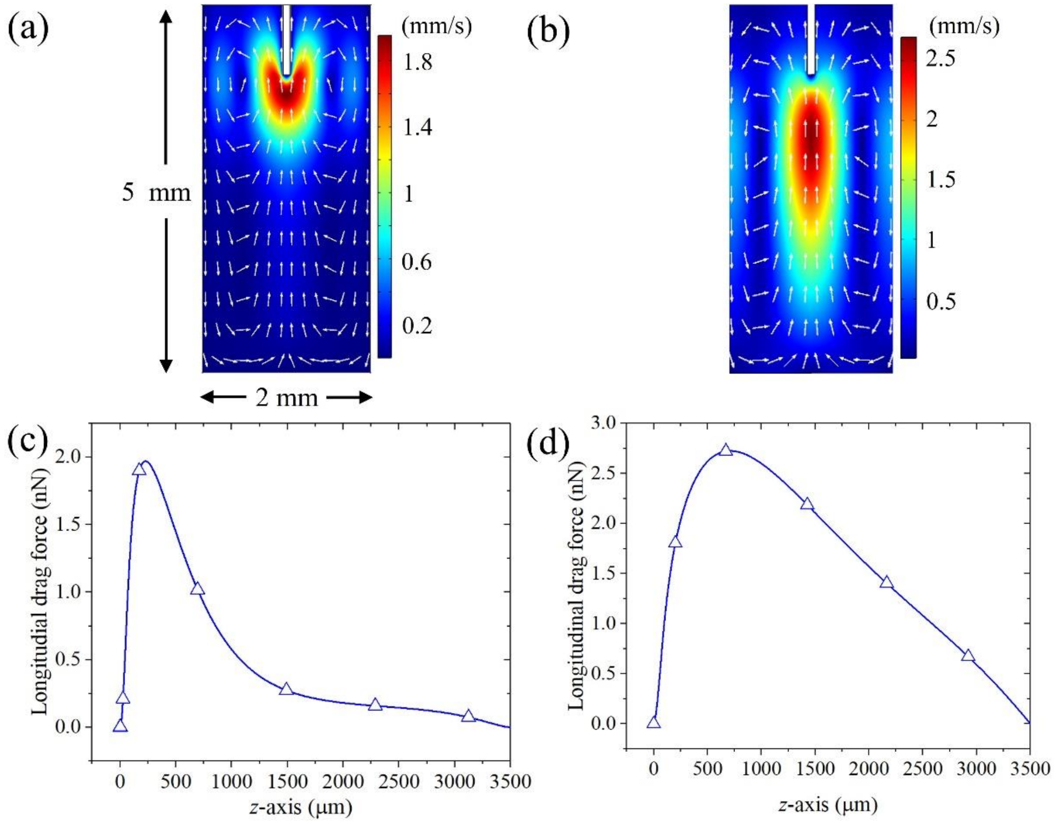

Fig. 7.5 (a) Convective currents velocity profile due to the light absorption at the AgNPs film (λ = 445 nm with 10 mW of optical power) extracted from COMSOL simulations. (b) Convective currents velocity profile due to the light bulk absorption of ethanol (λ = 1,550 nm with 15 mW of optical power) extracted from COMSOL simulations. (c) Transversal drag force along the z-axis due to light absorption from AgNPs for a bubble of R = 50 µm. (d) Longitudinal drag force gradient along the z-axis due to light bulk absorption of ethanol for a bubble of R = 50 µm.

It is well known that a bubble immersed into a liquid will face the buoyancy force $\boldsymbol{F_b} = {}^{4}/_{3}\,\pi\rho_l\boldsymbol{g}R^3$ which always point against the gravity force, in particular for a microbubble of R = 100 µm the buoyancy force is $\boldsymbol{F_b} = 32.4\ nN$. The buoyance force increases rapidly as the bubble radius grows and may eventually overcome the Marangoni force and leave the fiber. However, for the microbubbles generated in these experiments, the buoyancy force is smaller than the Marangoni force. Additionally, optical forces may be present, however, since the beam is not strongly focused (9 µm for single-mode fiber and 105 µm for multi-mode optical fibers), both gradient and the force associated with the radiation pressure lies in the range of pN which is much smaller than the Marangoni, drag, and buoyancy force. For such reasons, optical forces will not be taken into account in this analysis.

Figure 7.6(a) shows the transversal force components at z = 100 µm of the optothermal forces ($\boldsymbol{F_M}, \boldsymbol{F_d}$) acting on a microbubble of R = 100 µm induced by light absorption at the AgNPs. As noted before, the transversal component of both the Marangoni and the drag force acts as an attractive force, endorsing bubble trapping. Besides, the maximal transversal Marangoni gradient force is ~250 times larger than the velocity–associated drag force. Figure 7.6(b) shows the longitudinal components of the Marangoni, drag, and buoyancy force. Likewise, the longitudinal Marangoni force dominates over the other components near the fiber end but far from it, buoyancy force dominates.

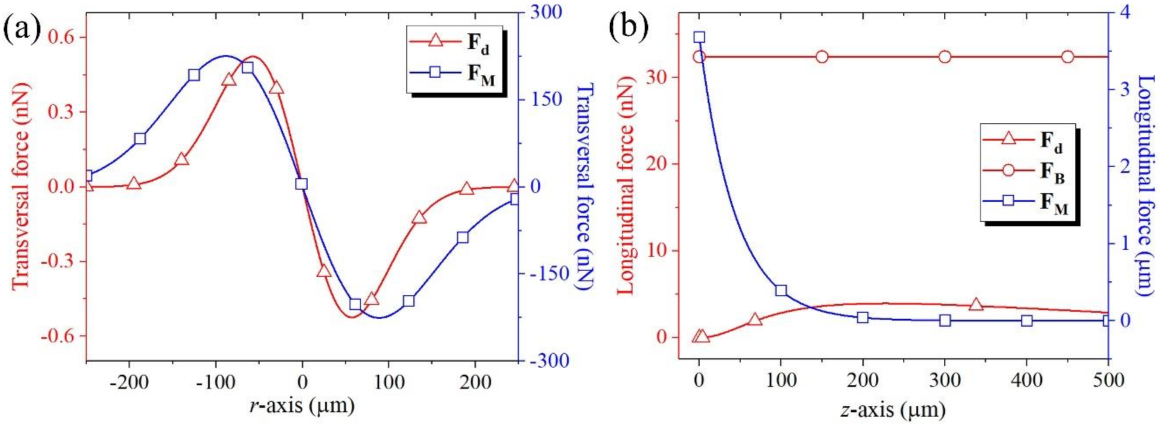

Fig. 7.6 Optothermal forces on a microbubble of R = 100 µm. (a) Transversal components of the gradient forces F_d (red triangles) and F_M (blue squares). (b) Longitudinal component of F_M (blue squares), F_d (red triangles), and F_b (red dots). Since F_M >> F_d and F_b, the microbubble is attracted to the optothermal source, i.e., the distal end of the optical fiber.

Since the Marangoni force is much larger than the buoyancy force, a microbubble can in principle be trapped in a horizontal plane. In fact, we found that by placing 3 different optical fibers (one multi-mode for microbubble generation and two single-mode for trapping) in a horizontal plane, a microbubble can be trapped and transferred from one fiber to the next by sequentially switching on and off the CW lasers as shown in Fig. 7.2 and Visualization 7.1. The temperature reached at the interface is a function of both the laser power P and the silver absorption coefficient α_{Ag} at the wavelength employed, so the interface temperature can be raised beyond the boiling point of ethanol (~ 78 °C) [169]. Note that the bubble is out of focus meaning that the buoyancy force moves the bubble out of the plane of the trapping fibers. The Marangoni force is so strong that one can see the bubble deformation when the laser is turned on. Moreover, since the absorption from the AgNPs is large in the visible and NIR, our experimental results show that there is not spectral selectivity in the trapping and 3D manipulation of microbubbles by the Marangoni effect, i.e., the microbubble is trapped and manipulated by CW lasers emitting at different wavelengths with low optical powers.

Conclusions

In conclusion, we have demonstrated both theoretically and experimentally the 3D trapping and manipulation of photothermally induced microbubbles by the Marangoni force. As in optical tweezers, Marangoni and drag forces can be decomposed in transversal and longitudinal gradient force components. The maximal longitudinal gradient force is achieved on the surface of the fiber if nanoparticles are photodeposited. In the case of light bulk absorption in ethanol, the bubble is trapped at ~ 80 μm from the fiber tip (for λ = 1,550 nm and $\alpha \sim 5.63$ cm^{-1}). Although drag (generated by convective currents) and buoyancy forces are present they are much smaller than the Marangoni one. Finally, we show that a bubble can be displaced from one fiber to another by sequential switching the light sources. 3D trapping of large bubbles opens the opportunity for more complex manipulation configurations.

Chapter 8. General conclusions and future work

Conclusions

In this work, we have demonstrate both theoretically and experimentally the potential of the optothermal effects (induced by both light bulk absorption and nanoparticles absorption) to carry out the quasi-steady-state 3D trapping and manipulation of vapor microbubbles. Optothermal effects are mainly driven by the Marangoni force, whose origin lies in thermal effects and is at least 4 orders of magnitude greater than optical forces. On the other hand, optical phenomena provide both noncontact and noninvasive approaches of bubbles manipulation while thermal phenomena can provide forces many orders of magnitude larger than optical ones. So optothermal phenomena offers the best of the two worlds.

We have demonstrated the controlled generation of microbubbles by both laser-induced thermal breakdown, employing CW laser, and optical breakdown, using a nanosecond pulsed laser, at low power and low energy, respectively. On the other hand, by using a high-speed camera, we have shown both the temporal evolution of the microbubble growth and the microbubble coalescence. This microbubble coalescence leads to the generation of a bigger bubble, called main-bubble, which is steady-state 3D trapping.

We have obtained the temperature distribution and convective currents profiles induced by both CW laser and pulsed laser by solving the Navier-Stokes equations together with the heat transfer equation using Comsol Multiphysics. By numerical simulation, we have presented the time evolution of the interface temperature (AgNPs-ethanol interface) as a function of the Gaussian pulse duration. Moreover, we have presented analytical expressions that allow us to describe the mechanism behind the 3D trapping and manipulation of vapor microbubbles, i.e., we decomposed optothermal forces into their longitudinal and transversal forces just like optical forces, effectively creating a 3D potential well.

Besides, we have showed for the first time, stable 3D trapping and the manipulation of microbubbles in absorbing liquids employing low power CW laser (445 nm), i.e., a careful balance of vapor condensation and evaporation rate induced by the trapping laser produce stably trapping for up to 10 min using an optical power as low as 2.7 mW.

In addition, since the absorption from the AgNPs is large in the visible and NIR, our experimental results show that there is no spectral selectivity in the trapping and 3D manipulation of microbubbles by the Marangoni effect, i.e., the microbubble is trapped and manipulated by CW lasers emitting at different wavelengths with low optical powers.

In general conclusion, the Marangoni force is a topic of great interest to the field of both nano and micromanipulation. Moreover, the Marangoni force have emerged as an efficient and straightforward tool to accomplish non-invasive trapping and 3D manipulation of microbubbles up to 150 μm of radius, maintaining the accuracy of the spatial control of the microbubbles.

Future work

The forthcoming work of this investigation can be divided in two parts:

Now that the potential of the Marangoni force as both trapping and manipulation mechanism of microbubbles have been demonstrated, the next step consist of incorporate this mechanism for transporting matter, i.e., using the bubble surface as a transporting instrument.

Once the controlled bubble generation by both laser pulse and CW laser have been presented, the next phase is integrate this bubble generation mechanism into the microfluidics filed. Bubble can be useful as a control flow in micro-valves, i.e., open-loop and closed-loop. Also, as a pumping system, i.e., boost the liquid by the bubble expansion.

Chapter 9. Productions

List of publications

2021 **3D trapping of microbubbles by the Marangoni effect**
J.A. Sarabia-Alonso, J.G. Ortega-Mendoza, S. Mansurova, F.M. Muñoz-Pérez, and R. Ramos-García. Optics Letters, **46**(23).

2020 **Steady-State 3D trapping and manipulation of microbubbles using thermocapillary**
F.M. Muñoz-Pérez, J.G. Ortega-Mendoza, A. Padilla-Vivanco, C. Toxqui-Quitl, **J.A. Sarabia-Alonso**, and R. Ramos-García. Frontier in Physics, 8, 585590.

2020 **Optical trapping in the presence of laser-induced thermal effects**
J.A. Zenteno-Hernández, J. Vázquez-Lozano, **J.A. Sarabia-Alonso**, J. Ramírez-Ramírez, and, R. Ramos-García. Optics Letters **45**(14), 3961-3964.

2020 **Optothermal generation, trapping, and manipulation of microbubbles**
J.A. Sarabia-Alonso, J.G. Ortega-Mendoza, J.C. Ramírez-San-Juan, P. Zaca-Morán, J. Ramírez-Ramírez, A. Padilla-Vivanco, F. M. Muñoz-Pérez, and, R. Ramos-García. Opt. Express **28**(12), 17672-17682.

2018 **Marangoni force-driven manipulation of photothermally-induced microbubbles**
J.G. Ortega-Mendoza, **J.A. Sarabia-Alonso**, P. Zaca-Morán, A. Padilla-Vivanco, C. Toxqui-Quitl, I. Rivas-Cambero, J. Ramírez-Ramírez, S.A. Torres-Hurtado, and R. Ramos-García. Opt. Express **26**(6), 6653-6662.

Proceedings

2021 **3D trapping of vapor microbubbles: an experimental and theoretical analysis - Presentation**
J.A. Sarabia-Alonso and R. Ramos-García, Mexican Optics and Photonics Meeting.

2021 **Micro-grabado láser sobre nanopelículas de titanio usando láser continuo de baja potencia**
J.A. Ascencio-Rodríguez, **J.A. Sarabia-Alonso**, S. Mansurova and R. Ramos-García, Mexican Optics and Photonics Meeting.

2021 **Behind optothermal trapping of photothermally-induced microbubbles – Presentation**
J.A. Sarabia-Alonso, J.G. Ortega-Mendoza, J.C. Ramírez-San-Juan, and R. Ramos-García, Optical Trapping and Optical Micromanipulation XVIII, SPIE.

2020 **Trapping and manipulation of a microbubble in 3D through temperature gradients – Presentation**
J.A. Sarabia-Alonso, F.M. Muñoz-Pérez, A. Padilla-Vivanco, C. Toxqui Quitl, J.G. Ortega-Mendoza, and R. Ramos-García, Optical Trapping and Optical Micromanipulation XVII, SPIE.

2020 **Enhancement of the stiffness constant in optical tweezers by thermal effects**
J. Vazquez-Lozano, J.A. Zenteno- Hernández, **J.A. Sarabia-Alonso**, J. Ramírez-Ramírez, R. Ramos-García, Optical Trapping and Optical Micromanipulation XVII, SPIE.

2020 **Detrás del atrapamiento optotérmico**
J.A. Sarabia-Alonso and R. Ramos-García, 2do Congreso de Tópicos Avanzados de Óptica y Electrónica.

2019 **3D manipulation of opthothermally-induced bubbles by a nanosecond pulsed laser**
J.A. Sarabia-Alonso, J.G. Ortega-Mendoza, J.C. Ramírez-San-Juan, P. Zaca-Morán, A. Padilla-Vivanco, J. Ramírez-Ramírez, and R. Ramos-García. Optical Trapping and Optical Micromanipulation XVI, SPIE.

2019 **3D manipulation of microbubbles by laser-induced thermal gradients**
J.A. Sarabia-Alonso, J.G. Ortega-Mendoza, J.C. Ramírez-San-Juan, A. Padilla-Vivanco, J. Ramírez-Ramírez, and R. Ramos-García. RIAO-OPTILAS-MOPM 2019.

2018 **Manipulation of photothermally generated microbubbles**

R. Ramos-García, J. G. Ortega-Mendoza, **J. A. Sarabia-Alonso**, P. Zaca-Morán, A. Padilla-Vivanco, C. Toxqui-Quitl, I. Rivas-Cambero, J. Ramírez-Ramírez, and S. A. Torres-Hurtado. Optical Trapping and Optical Micromanipulation XV, SPIE.

Bibliography

1. Marshall, G., Sykes, A., Berry, J. & Jonker, L. The “ humble” bubble: Contrast-enhanced ultrasound. *Radiography* **17**, 345–349 (2011).
2. Datta, S. *et al.* Ultrasound-Enhanced Thrombolysis Using Definity® as a Cavitation Nucleation Agent. *Ultrasound Med. Biol.* **34**, 1421–1433 (2008).
3. Postema, M. & Schmitz, G. Bubble dynamics involved in ultrasonic imaging. *Expert Rev. Mol. Diagn.* **6**, 493–502 (2006).
4. Berrospe C., Visser C. W., Schlautmann S., Rvs D., and R.-G. R. Toward jet injection by continuous-wave laser cavitation. *J. Biomed. Opt* **22**, 105003 (2017).
5. Padilla-Martinez, J. P. *et al.* Towards the enhancement of transdermal drug delivery through thermocavitation. *Photonics Lasers Med.* **1**, 183–193 (2012).
6. Lin L., Peng X., Mao Z., Li W., Yogeesh M. N., Rajeeva B. B., Perillo E. P., Dunn A. K., Akinwande D. and, Z. Y. Bubble-pen lithography. *Nano Lett.* **16**, 701–708 (2016).
7. Ashkin, A., Dziedzic, J. M., Bjorkholm, J. E. & Chu, S. Observation of a single-beam gradient force optical trap for dielectric particles. *Opt. Angular Momentum* **11**, 196–198 (1986).
8. Ashkin, A. History of Optical Trapping and Manipulation of Small-Neutral Particle, Atoms, and Molecules. *IEEE J. Sel. Top. Quantum Electron.* **6**, 841–856 (2000).
9. Takahira H., Shirasawa M., and Y. S. Laser Manipulation of Bubbles and Evaluation of Its Optical Force. *JSME Int. J.* **43**, 393–399 (2000).
10. Li F., Gonzalez-Avila R., Nguyen D. M., and O. C. D. Oscillate boiling from microheaters. *Phys. Rev. Fluids* **2**, 2017 (2017).
11. I., R. J. Lumped models of gas bubbles in thermal gradients. *Appl. Math. Model.* **21**, 371–386 (1997).
12. Miniewicz, A., Bartkiewicz, S., Orlikowska, H. & Dradrach, K. Marangoni effect visualized in two-dimensions Optical tweezers for gas bubbles. *Sci. Rep.* **6**, 1–8 (2016).
13. Gogate, P. R. & Pandit, A. B. A review and assessment of hydrodynamic cavitation as a technology for the future. *Ultrason. Sonochem.* **12**, 21–27 (2005).
14. Xi X., Cegla F. B., Lowe M., Thiemann A., Nowak T., Mettin R., Holsteyns F., and L. A. Study on the bubble transport mechanism in an acoustic standing wave field. *Ultrasonic* **51**, 1014–1025 (2011).
15. Pelekasis, N. A., Gaki, A., Doinikov, A. & Tsamopoulos, J. A. *Secondary Bjerknes forces between two bubbles and the phenomenon of acoustic streamers*. *Journal of Fluid Mechanics* **500**, (2004).
16. Ashkin, A. Forces of a single-beam gradient laser trap on a dielectric sphere in the ray optics regime. *Methods Cell Biol.* **61**, 1–27 (1998).
17. Fazal, F. M. & Block, S. M. Optical tweezers study life under tension. *Nat. Photonics* **5**, 318–321 (2011).

18. Mateu, M. G. *Structure and Physics of Viruses*. (2012). doi:10.1007/978-94-007-6552-

19. Wang, M. D., Yin, H., Landick, R., Gelles, J. & Block, S. M. Stretching DNA with optical tweezers. *Biophys. J.* **72**, 1335–1346 (1997).

20. Smith, D. E. *et al.* The bacteriophage φ29 portal motor can package DNA against a large internal force. *Nature* **413**, 748–752 (2001).

21. Svoboda, K. & Block, S. M. Optical trapping of metallic Rayleigh particles. *Opt. Lett.* **19**, 930 (1994).

22. Ashkin, A. Forces of a single-beam gradient laser trap on a dielectric sphere in the ray optics regime. *Biophys. J.* **61**, 569–582 (1992).

23. Wang, Y., Luo, L., Ke, M. & Liu, Z. Acoustic Subwavelength Manipulation of Particles with a Quasiperiodic Plate. *Phys. Rev. Appl.* **17**, 1 (2022).

24. Nilsson, A., Petersson, F., Jönsson, H. & Laurell, T. Acoustic control of suspended particles in micro fluidic chips. *Lab Chip* **4**, 131–135 (2004).

25. Kayani, A. A., Khoshmanesh, K., Ward, S. A., Mitchell, A. & Kalantar-zadeh, K. Optofluidics incorporating actively controlled micro- and nano-particles. *Biomicrofluidics* **6**, (2012).

26. Gaš, B. Theory of electrophoresis: Fate of one equation. *Electrophoresis* **30**, (2009).

27. Klepárník, K. & Boček, P. Electrophoresis today and tomorrow: Helping biologists' dreams come true. *BioEssays* **32**, 218–226 (2010).

28. Pohl, H. A. Dielectrophoresis: The Behavior of Neutral Matter in Nonuniform Electric Fields. in **55**, 68–69 (Cambridge University Press, 1978).

29. Khoshmanesh, K., Nahavandi, S., Baratchi, S., Mitchell, A. & Kalantar-zadeh, K. Dielectrophoretic platforms for bio-microfluidic systems. *Biosens. Bioelectron.* **26**, 1800–1814 (2011).

30. Thomson, J. On certain curious motions observable at the surfaces of wine and other alcoholic liquors. *Philos Mag* **10**, 330–333 (1855).

31. Maranoni, C. On the expansion of a drop of liquid floating on the surface of another liquid. *Tipographia dei fratelli Fusi, Pavia* (Pavia, 1865).

32. Hadamard, J. S. Mouvement permanent lent d'une sphere liquide et visqueuse dans un liquide visqueux. *C. R. Acad. Sci* **152**, 1735–1738 (1911).

33. Rybczynski, W. Über die fortschreitende Bewegung einer flüssigen Kugel in einem zähen Medium. *Bull. Acad. Sci. Cracovie, A* **1**, 40–46 (1911).

34. Young, N. O., Goldstein, J. S. & Block, M. J. The motion of bubbles in a vertical temperature gradient. *J. Fluid Mech.* **6**, 350–356 (1959).

35. Ramos, J. I. Lumped models of gas bubbles in thermal gradients. *Appl. Math. Model.* **21**, 371–386 (1997).

36. Hershey, A. V. Ridges in a liquid surface due to the temperature dependence of surface tension [3]. *Phys. Rev.* **56**, 204 (1939).

37. Fedosov, A. I. Thermocapillary motion. (1956).

38. Thompson, R. L., DeWitt, K. J. & Labus, T. L. Marangoni bubble motion phenomenon in zero gravity. *Chem. Eng. Commun.* **5**, 299–314 (1980).

39. Wozniak, G., Siekmann, J. & Srulijes, J. Thermocapillary bubble and drop dynamics under reduced gravity-survey and prospects. *Z. Flugwiss. Weltraumforsch.* **12**, 137–144 (1988).

40. Merritt, R. M. & Subramanian, R. S. Migration of a gas bubble normal to a plane horizontal surface in a vertical temperature gradient. *J. Colloid Interface Sci.* **131**, 514–525 (1989).

41. Takahashi, K., Weng, J. G. & Tien, C. L. Marangoni effect in microbubble systems. *Microscale Thermophys. Eng.* **3**, 169–182 (1999).

42. Miniewicz A., Quintard C., Orlikowska H., and B. S. On the origin of the driving force in the Marangoni propelled gas bubble trapping mechanism. *Phys Chem Chem Phys.* **19**, 18695–18703 (2017).

43. Miniewicz, A., Bartkiewicz, S. & Karpinski, P. Optical trapping mechanisms based on optothermal Marangoni effect. 94 (2019). doi:10.1117/12.2529251

44. Prentice, P. A. *et al.* Manipulation and filtration of low index particles with holographic Laguerre-Gaussian optical trap arrays. *Opt. Express* **12**, 593 (2004).

45. Li, Y., Abeywickrema, U. & Banerjee, P. Dynamics of laser-induced microbubbles in an absorbing liquid. *Opt. Eng.* **58**, 1 (2019).

46. Angelsky O. V., Berkshaev A. Ya., Maksimyak P. P., Maksimyak A. P., and H. S. G. Low-temperature laser-stimulated controllable generation of micro-bubbles in a water suspension of absorptive colloid particles. *Opt. Express* **26**, 13995–14009 (2018).

47. Ivanova, N. A. & Bezuglyĭ, B. A. Optical thermocapillary bubble trap. *Tech. Phys. Lett.* **32**, 854–856 (2006).

48. Flynn, H. Physics of acoustic cavitation in liquids. *Phys. Acoust.* **1**, 57–172 (1964).

49. Chandran, P., Bakshi, S. & Chatterjee, D. Study on the characteristics of hydrogen bubble formation and its transport during electrolysis of water. *Chem. Eng. Sci.* **138**, 99–109 (2015).

50. German, S. R. *et al.* Electrochemistry of single nanobubbles. Estimating the critical size of bubble-forming nuclei for gas-evolving electrode reactions. *Faraday Discuss.* **193**, 223–240 (2016).

51. Sadatomi, M., Kawahara, A., Kano, K. & Ohtomo, A. Performance of a new micro-bubble generator with a spherical body in a flowing water tube. *Exp. Therm. Fluid Sci.* **29**, 615–623 (2005).

52. Rodelta Pumps International. Pump Cavitation What Happens and What Causes It? (2019). Available at: https://fluidhandlingpro.com/fluid-process-technology/pumps-pumping-systems/pump-cavitation-what-happens-and-what-causes-it/.

53. Li, F., Gonzalez-Avila, S. R., Nguyen, D. M. & Ohl, C. D. Oscillate boiling from microheaters. *Phys. Rev. Fluids* **2**, 1–9 (2017).

54. S.Incropera, F. P., Dewitt, D. P., Bergman, T. L. & Lavine, A. *Fundamentals of heat and mass transfer*. (John Wiley & Sons, 2007).

55. Xi, X. *et al.* Study on the bubble transport mechanism in an acoustic standing wave field. *Ultrasonics* **51**, 1014–1025 (2011).

56. Lauterborn, W. & Kurz, T. Physics of bubble oscillations. *Reports Prog. Phys.* **73**, (2010).

57. Brennen, C. E. *Cavitation and bubble dynamics*. *Cavitation and Bubble Dynamics* (Oxford University Press, Inc., 1995). doi:10.1017/CBO9781107338760

58. Bjerknes, V. F. K. *Fields of force*. (Columbia University Press, 1906).

59. Jiao, J. *et al.* Experimental and theoretical analysis of secondary Bjerknes forces between two bubbles in a standing wave. *Ultrasonics* **58**, 35–42 (2015).

60. Villanueva, G., Carlos, R., Encinas, L. & Hazalia, B. Dielectroforesis para sistemas. *Cienc. Ergo Sum* **20**, 227–230 (2013).

61. Li, D. *Encyclopedia of Microfluidics and Nanofluidics*.

62. Nelson, W. & Kim, C. Droplet actuation by electrowetting-on-dielectric (EWOD): A review. *ournal Adhes. Sci. Technol.* **26**, 1747–1771 (2012).

63. Chung, S. K., Zhao, Y. & Cho, S. K. On-chip creation and elimination of microbubbles for a micro-object manipulator. *J. Micromechanics Microengineering* **18**, (2008).

64. Palit, S. R. Thermodynamic interpretation of the eötvös constant. *Nature* **177**, 1180 (1956).

65. Qu, X. & Qiu, H. Bubble dynamics under a horizontal micro heater array. *J. Micromechanics Microengineering* **19**, (2009).

66. Bashkatov, A., Hossain, S. S., Yang, X., Mutschke, G. & Eckert, K. Oscillating Hydrogen Bubbles at Pt Microelectrodes. *Phys. Rev. Lett.* **123**, 214503 (2019).

67. Chakraborty, S. Electrocapillarity. in *Encyclopedia of Microfluidics and Nanofluidics* (ed. Dongqing, L.) 460–468 (Springer, Boston, MA, 2008). doi:https://doi.org/10.1007/978-0-387-48998-8

68. Prins, M. W. J., Welters, W. J. J. & Weekamp, J. W. Fluid control in multichannel structures by electrocapillary pressure. *Science (80-.).* **291**, 277–280 (2001).

69. Tanyeri, M., Johnson-Chavarria, E. M. & Schroeder, C. M. Hydrodynamic trap for single particles and cells. *Appl. Phys. Lett.* **96**, 1–4 (2010).

70. Lieu, V. H., House, T. A. & Schwartz, D. T. Hydrodynamic tweezers: Impact of design geometry on flow and microparticle trapping. *Anal. Chem.* **84**, 1963–1968 (2012).

71. Chan, C. L. & Chen, C. F. Salt-finger convection generated by thermal and solutal capillary motion in a stratified fluid. *Int. J. Heat Mass Transf.* **42**, 2143–2159 (1999).

72. Somasundaran, P. & Zhang, L. Surfactants and Interiacial Phenomena In Cosmetics and Detergency. *Ency* **116**, (2001).

73. Wang, K. *et al.* Magnetic field induced motion behavior of gas bubbles in liquid. *Sci. Rep.* **6**, 2–7 (2016).

74. Aliabadi, A. & Taklifi, A. The effect of magnetic field on dynamics of gas bubbles in visco-elastic fluids. *Appl. Math. Model.* **36**, 2567–2577 (2012).

75. Oshemkov S. V., Dvorkin L. P., and D. V. Y. Trapping and Manipulating Gas Bubbles in

Water with Ultrashort Laser Pulses at a High Repetition Rate. *Appl. Phys. Lett.* **35**, 72–79 (2009).

76. Burns, T. M., Preece, D., Niemenen, T. A. & Rubinsztein-Dunlop, H. Optical tweezers for precise control of micro-bubble arrays: in situ temperature measurement. *Opt. Trapp. Opt. Micromanipulation X* **8810**, 88102B (2013).

77. Smart, T. J., Ünlü, M. B. & Jones, P. H. Microbubble trapping in inverted optical tweezers. *Opt. Trapp. Opt. Micromanipulation XIV*, **1034731**, (2017).

78. Flores-Flores E., Torres-Hurtado S. A., Páez R., Ruiz U., Beltrán-Pérez G., Neale S. L., Ramirez-San-Juan J. C., and R.-G. R. Trapping and manipulation of microparticles using laser-induced convection currents and photophoresis. *Biomed. Opt. Express* **6**, 4079–4087 (2015).

79. Zenteno-Hernandez, J. A., Vázquez Lozano, J., Sarabia-Alonso, J. A., Ramírez-Ramírez, J. & Ramos-García, R. Optical trapping in the presence of laser-induced thermal effects. *Opt. Lett.* **45**, 3961 (2020).

80. Ramírez Ramírez, J., Vazquez Lozano, J. I., Ramos-García, R. & Ruiz Corona, U. Assembly and 2D manipulation of colloidal crystal by temperature gradient. **10723**, 103 (2018).

81. Nguyen D. M, Hu L., Miao J., and O. C.-D. Oscillate Boiling from Electrical Microheaters. *Phys. Rev. Appl.* **10**, 044064 (2018).

82. Sung-Yong P., Ting-Hsiang W., Yue Chen, Teitellc M. A., and P.-Y. C. High-speed droplet generation on demand driven by pulse laser-induced cavitation. *Lab Chip* **11**, 1010–1012 (2011).

83. Kao Y., Wang X., Warren J., Xu J., and A. D. Journal of Micromechanics and Microengineering A bubble-powered micro-rotor: conception, manufacturing, assembly and characterization. *J. Micromech. Microeng.* **17**, 2454–2460 (2007).

84. Schonung, B. & Winter, M. Bubble-driven liquid flows. *J. Fluid Mech.* **170**, 53–82 (1986).

85. Torniainen, E. D., Govyadinov, A. N., Markel, D. P. & Kornilovitch, P. E. Bubble-driven inertial micropump. *Phys. Fluids* **24**, (2012).

86. A., R. P. and N. Selective particle trapping using an oscillating microbubble. *Lab. Chip* **11**, 3710–3715 (2011).

87. Li, J. & Zheng, Y. Optothermally Assembled Nanostructures. *Accounts Mater. Res.* **2**, 352–363 (2021).

88. Hardy L.A., Kennedy J.D., Wilson C.R., Irby P.B., and F. N. M. Analysis of thulium fiber laser induced bubble dynamics for ablation of kidney stones. *J. Biophotonics* **10**, 1240–1249 (2016).

89. Kaneko, Y., Takagi, S. & Matsumoto, Y. Renal Stone Comminution Utilizing Cloud Cavitation (1st Report , The Control of Cloud Cavitation). *Japan Sci. Technol. Agency* **70**, 904–911 (2004).

90. Oxtoby, D. W. Nucleation of First-Order Phase Transitions. *Acc. Chem. Res.* **31**, 91–97 (1998).

91. E., B. C. *Cavitation and Bubble Dynamics*. (Oxford University Press, Inc., 1995).

92. Berrospe-Rodriguez, C. Towards needle-free injection by thermocavitation in microfluidic devices. (INAOE, 2017).

93. Juan, B. M. S. *et al*. Thermocavitation: A novel optical cavitation method. (INAOE, 2013).

94. Lloveras, P., Salvat-Pujol, F., Truskinovsky, L. & Vives, E. Boiling crisis as a critical phenomenon. *Phys. Rev. Lett.* **108**, 25–28 (2012).

95. Yan, G. A. A., Prokhorov, A. M. & Shipulo, G. P. THE EFFECTS OF A LASER BEAM IN A LIQUID. *Sov. Phys. JETP* **17**, 1463–1465 (1963).

96. Carome, E. F., Clark, N. A. & Moeller, C. E. Generation of acoustic signals in liquids by ruby laser-induced thermal stress transients. *Appl. Phys. Lett.* **4**, 95–97 (1964).

97. Shen, Y. R. *The Principles of Nonlinear Optics*. (1984).

98. Niemz, M. H. *Laser-Tissue Interactions*.

99. Vogel, A., Nahen, K., Theisen, D. & Noack, J. Plasma formation in water by picosecond and nanosecond Nd:YAG laser pulses - Part I: Optical breakdown at threshold and superthreshold irradiance. *IEEE J. Sel. Top. Quantum Electron.* **2**, 847–859 (1996).

100. Sacchi, C. A. Laser-induced electric breakdown in water. *J. Opt. Soc. Am. B* **8**, 337 (1991).

101. Kennedy, P. K. A First-Order Model for Computation of Laser-Induced Breakdown Thresholds in Ocular and Aqueous Media: Part I—Theory. *IEEE J. Quantum Electron.* **31**, 2241–2249 (1995).

102. Rastopov, S. F. & Sukhodol'sky, A. T. Cluster nucleation in the process of CW laser induced thermocavitation. *Phys. Lett. A* **149**, 229–232 (1990).

103. Byun, K. T. & Kwak, H. Y. A Model of Laser-Induced Cavitation. *Japanese J. Appl. Physics, Part 1 Regul. Pap. Short Notes Rev. Pap.* **43**, 621–630 (2004).

104. Rastopov, S. F. & Sukhodolsky, A. T. Optical Radiation Interaction with Matter. in *Sound generation by thermocavitation-induced cw laser in solutions* **1440**, 127–134 (1991).

105. Padilla-Martinez J. P., Berrospe-Rodriguez C., Aguilar G., Ramirez-San-Juan J. C., and R.-G. R. Optic cavitation with CW lasers: A review. *Phys. Rev. Fluids* **26**, 122007 (2014).

106. Ramirez-San-Juan J.C., Rodriguez-Aboytes E., E. Martinez-Canton A., Baldovino-Pantaleon O., Robledo-Martinez A., Korneev N., and R.-G. R. Time-resolved analysis of cavitation induced by CW lasers in absorbing liquids. *Opt. Express* **18**, 8735–8742 (2010).

107. Vogel A., Noack J., Nahen K., Theisen D., Busch S., Parlitz U., Hammer D. X., Noojin G. D., Rockwell B. A., and B. R. Energy balance of optical breakdown in water at nanosecond to femtosecond time scales. *Appl. Phys. B* **68**, 271–280 (1999).

108. Zhang, L., Gong, S., Lu, Z., Cheng, P. & Wang, E. N. Boiling crisis due to bubble interactions. *Int. J. Heat Mass Transf.* **182**, (2022).

109. Nikolayev, V. S. & Beysens, D. A. Boiling crisis and non-equilibrium drying transition. *Europhys. Lett.* **47**, 345–351 (1999).

110. Cengel, Y. A. Boiling and condensation. in *Basics of heat transfer* 515–560 (Mc Graw Hill, 2002). doi:10.1016/0306-2619(91)90004-h

111. Rattray Maurice Jr. Pertubation effects in cavitation bubble dynamics. (California Institute of Technology, 1951).

112. Chapman Richard Bruce. Nonspherical vapor bubble collapse Citation. (California Institute of Technology, 1970).

113. Johnsen E. and Colonius T. Numerical simulations of non-spherical bubble collapse. *J. Fluid Mech.* **629**, 231–262 (2009).

114. Parkinson, L., Sedev, R., Fornasiero, D. & Ralston, J. The terminal rise velocity of 10-100 μm diameter bubbles in water. *J. Colloid Interface Sci.* **322**, 168–172 (2008).

115. Mawell, J. C. *A treatise on electricity and magnetism*. **1**, (Oxford University Press, Inc., 1873).

116. Dienerowitz, M., Mazilu, M., Reece, P. J., Krauss, T. F. & Dholakia, K. Optical vortex trap for resonant confinement of metal nanoparticles. *Opt. Express* **16**, 4991 (2008).

117. Gao, D. *et al.* Optical manipulation from the microscale to the nanoscale: Fundamentals, advances, and prospects. *Light Sci. Appl.* **6**, (2017).

118. Klaseboer E., Manica R., Hendrix M. H. W., Ohl C. D., and C. D. Y. C. A force balance model for the motion, impact, and bounce of bubbles. *Phys. Fluids* **26**, 092101 (2014).

119. Ohl C. D., Tijink A., and A. P. A. The added mass of an expanding bubble. *J. Fluid Mech.* **482**, 271–290 (2003).

120. Lazarus C., Pouliopoulos A. N., Tinguely M., Garbin V., and C. J. J. Clustering dynamics of microbubbles exposed to low-pressure 1-MHz ultrasound. *J. Acoust. Soc. Am.* **142**, 3135–3146 (2017).

121. Hashmi A., Yu G., Reilly-Collette M., Heiman G., and X. J. Oscillating bubbles: a versatile tool for lab on a chip applications. *Lab Chip* **12**, 4216–4227 (2012).

122. Wu, Z.-B. & Hu, W.-R. Thermocapillary migration of a planar droplet at moderate and large Marangoni numbers. *Acta Mech.* **223**, 609–626 (2012).

123. Shin, J. H., Seo, J., Hong, J. & Chung, S. K. Hybrid optothermal and acoustic manipulations of microbubbles for precise and on-demand handling of micro-objects. *Sensors Actuators B Chem.* **246**, 415–420 (2017).

124. Khoshmanesh K., Almansouri A., Albloushi H., Yi P., Soffe R. and, K.-Z. K. A multi-functional bubble-based microfluidic system. *Sci. Rep.* **5**, 9942 (2015).

125. Takahashi, K., Yoshino, K., Hatano, S., Nagayama, K. & Asano, T. Novel applications of thermally controlled microbubble driving system. in *14th IEEE International Conference on Micro Electro Mechanical Systems* 286–289 (2001).

126. Garbin, V. *et al.* Optical micro-manipulation using Laguerre-Gaussian beams. *Japanese J. Appl. Physics, Part 1 Regul. Pap. Short Notes Rev. Pap.* **44**, 5773–5776 (2005).

127. Y., F. J. and Y. L. Microscale acoustofluidics: Microfluidics driven via acoustics and ultrasonics. *Rev. Mod. Phys.* **83**, 647–704 (2011).

128. Angelsky, O. V. *et al.* Controllable generation and manipulation of micro-bubbles in water with absorptive colloid particles by CW laser radiation. *Opt. Express* **25**, 5232–5243 (2017).

129. Ortega-Mendoza J. G., Chávez F., Zaca-Morán P., Felipe C., Pérez-Sánchez G. F., Beltran-Pérez G., Goiz O., and R.-G. R. Selective photodeposition of zinc nanoparticles on the core of a single-mode optical fiber. *Opt. Express* **21**, 6509–6518 (2013).

130. Zaca-Morán, P. *et al.* High gain pulsed erbium-doped fiber amplifier for the nonlinear characterization of SWCNTs photodeposited on optical fibers. *Opt. Laser Technol.* **52**, 15–20 (2013).

131. Ortega-Mendoza, J. G. *et al.* Optical fiber sensor based on localized surface plasmon resonance using silver nanoparticles photodeposited on the optical fiber end. *Sensors (Switzerland)* **14**, 18701–18710 (2014).

132. Baffou G., Polleux J., Rigneault H., and M. S. Super-Heating and Micro-Bubble Generation around Plasmonic Nanoparticles under cw Illumination. *J. Phys. Chem. C* **118**, 4890–4898 (2014).

133. Pimentel-Domínguez R., Hernández-Cordero J., and Z. R. Microbubble generation using fiber optic tips coated with nanoparticles. *Opt. Express* **20**, 8732–8740 (2012).

134. Kitz M., Preisser S., Wetterwald A., Jaeger M., Thalmann G. N., and F. M. Vapor bubble generation around gold nano-particles and its application to damaging of cells. *Biomed. Opt. Express* **2**, 291–304 (2011).

135. Coronado, E. A., Encina, E. R. & Stefani, F. D. Optical properties of metallic nanoparticles: manipulating light, heat and forces at the nanoscale. *Nanoscale* **3**, 4042–4059 (2011).

136. Xie, Y. & Zhao, C. *An optothermally generated surface bubble and its applications*. *Nanoscale* **9**, (2017).

137. Deguchi, S., Takahashi, S., Hiraki, H. & Tanimura, S. Direct measurement of force exerted during single microbubble generation. *Appl. Phys. Lett.* **102**, (2013).

138. Vélez-Cordero, J. R. & Hernández-Cordero, J. On the motion of carbon nanotube clusters near optical fiber tips: thermophoresis, radiative pressure and convection effects. *Langmuir* **31**, 10066–10075 (2015).

139. Subramanian, R. S. & Balasubramanian, R. *The motion of bubbles and drops in reduced gravity*. (Cambridge University, 2001).

140. Vazquez, G., Alvarez, E. & Navaza, J. M. Surface Tension of Alcohol + Water from 20 to 50 °C. *J. Chem. Eng. Data* **40**, 611–614 (1995).

141. Jones, P. H., Stride, E. & Saffari, N. Trapping and manipulation of microscopic bubbles with a scanning optical tweezer. *Appl. Phys. Lett.* **89**, 081113 (2006).

142. Lukianova-Hleb Ekaterina, Hu Ying, Latterini Loredana, Tarpani Luigi, Lee Seunghyun, Drezek Rebekah A., Hafner Jason H., and L. D. O. Plasmonic Nanobubbles as Transient Vapor Nanobubbles Generated around Plasmonic Nanoparticles. *ACS Nano* **4**, 2109–2123 (2010).

143. Boyd David A., Adleman James R., Goodwin David G., and P. D. Chemical Separations by Bubble-Assisted Interphase Mass-Transfer. *Anal. Chem.* **80**, 2452–2456 (2008).

144. Whitesides, G. M. The origins and the future of microfluidic. *Nature* **442**, 368–373 (2006).

145. Ahmed, D., Mao, X., Juluri, B. K. & Huang, T. J. A fast microfluidic mixer based on

acoustically driven sidewall-trapped microbubbles. *Microfluid Nanofluid* **7**, 727–731 (2009).

146. Wu, T. H. *et al.* Pulsed laser triggered high speed microfluidic fluorescence activated cell sorter. *Lab Chip* **12**, 1378–1383 (2012).

147. You, Q. Y., Zhang, H. J., Wang, Y. D. & Chen, J. J. Dynamic properties of symmetric optothermal microactuator. *J. Micromechanics Microengineering* **27**, aa7e10 (2017).

148. Chung S. K., Rhee K., and C. S. K. Bubble actuation by electrowetting-on-dielectric (EWOD) and its applications: A review. *Int. J. Precis. Eng. Manuf.* **11**, 991–1006 (2010).

149. Fujii, S. *et al.* Fabrication and placement of a ring structure of nanoparticles by a laser-induced micronanobubble on a gold surface. *Langmuir* **27**, 8605–8610 (2011).

150. Ortega-Mendoza J. G., Sarabia-Alonso J. A., Zaca-Morán P., Padilla-Vivanco A., Toxqui-Quitl C., Rivas-Cambero I., Ramirez-Ramirez J., Torres-Hurtado S. A., and R.-G. R. Marangoni force-driven manipulation of photothermally-induced microbubbles. *Opt. Express* **26**, 6653–6662 (2018).

151. Faccio D., Tamošauskas G., Rubino E., Darginavičius J., Papazoglou D. G., Tzortzakis S., Couairon A., and D. A. Cavitation dynamics and directional microbubble ejection induced by intense femtosecond laser pulses in liquids. *PhysRevE* **86**, 036304 (2012).

152. Siems A., Weber S. A. L., Boneberg J., and P. A. Thermodynamics of nanosecond nanobubble formation at laser-excited metal nanoparticles. *New J. Phys.* **13**, 043018 (2011).

153. Supponen, O. *et al.* Shock waves from nonspherical cavitation bubbles. *Phys. Rev. Fluids* **2**, 1–31 (2017).

154. Vogel A., Noack J., Nahen K., Theisen D., Busch S., Parlitz U., Hammer D. X., Noojin G. D., Rockwell B. A., A. & R., B. Energy balance of optical breakdown in water at nanosecond to femtosecond time scales. *Appl. Phys. B* **68**, 271–280 (1999).

155. Vogel, A., Busch, S. & Parlitz, U. Shock wave emission and cavitation bubble generation by picosecond and nanosecond optical breakdown in water. *J. Acoust. Soc. Am.* **100**, 148–165 (1996).

156. Vogel, A., Linz, N., Freidank, S. & G. Paltauf. Femtosecond-Laser-Induced Nanocavitation in Water: Implications for Optical Breakdown Threshold and Cell Surgery. *Phys. Rev. Lett.* **100**, 038102 (2008).

157. Hu, W., Ishii, K. S. & Ohta, A. T. Micro-assembly using optically controlled bubble microrobots. *Appl. Phys. Lett.* **99**, 094103 (2011).

158. Chiou, P. Y., Ohta, A. T. & Wu, M. C. Massively parallel manipulation of single cells and microparticles using optical images. *Nature* **436**, 370–372 (2005).

159. J. H. Lienhard IV and J. H. Lienhard V. *A heat transfer textbook*. (Phlogiston Press, 2017).

160. Wang, J. & Fiebig, M. Measurement of the thermal diffusivity of aqueous solutions of alcohols by a laser-induced thermal grating technique. *Int. J. Thermophys.* **16**, 1353–1361 (1995).

161. Jiang, Y., Pillai, S. & Green, M. A. Re-evaluation of literature values of silver optical constants. *Opt. Express* **23**, 2133 (2015).

162. Cabrera, H. *et al.* Absorption Spectra of Ethanol and Water Using a Photothermal Lens

Spectrophotometer. *Appl. Spectrosc.* **72**, 1069–1073 (2018).

163. John, L. E. Ethanol. *Kirk-Othmer Encyclopedia of Chemical Technology* 35 (2004). doi:https://doi.org/10.1002/0471238961.0520080112150719.a01.pub2

164. Lindau, O. & Lauterborn, W. Cinematographic observation of the collapse and rebound of a laser-produced cavitation bubble near a wall. *J. Fluid Mech.* **479**, 327–348 (2003).

165. *CRC Handbook of Chemistry and Physics*. (Boca Raton, Florida : CRC Press, 2017).

166. Zhao, C., Xie, Y., Mao, Z., Zhao, Y. & Rufo, J. Theory and experiment on particle trapping and manipulation via optothermally generated bubbles. *Lab Chip* **14**, 384–391 (2014).

167. Otha, A. T., Jamshidi, A., Valley, J. K., Hsu, H.-Y. & Wu, M. C. Optically actuated thermocapillary movement of gas bubbles on an absorbing substrate. *Appl Phys Lett.* **91**, 074103 (2007).

168. Zhang, C. L. *et al.* The Generation and Assembly of Laser-Induced Microbubbles. *J. Light. Technol.* **36**, 2492–2498 (2018).

169. Sarabia Alonso, J. A. *et al.* Optothermal generation, trapping and manipulation of microbubbles. *Opt. Express* **28**, 17672–17682 (2020).

170. Zaca-Morán, P. *et al.* Saturable and two-photon absorption in zinc nanoparticles photodeposited onto the core of an optical fiber. *Opt. Express* **23**, 18721 (2015).

171. Gonçalves, F. A. M. M. *et al.* PVT, viscosity, and surface tension of ethanol: New measurements and literature data evaluation. *J. Chem. Thermodyn.* **42**, 1039–1049 (2010).

172. Oshemkov, S. V., Dvorkin, L. P. & Dmitriev, V. Y. Trapping and manipulating gas bubbles in water with ultrashort laser pulses at a high repetition rate. *Tech. Phys. Lett.* **35**, 282–285 (2009).

173. Lü, B. L., Li, Y. Q., Ni, H. & Wang, Y. Z. Laser-induced hybrid trap for micro-bubbles. *Appl. Phys. B Lasers Opt.* **71**, 801–805 (2000).

174. Ye, J. Y. *et al.* Trapping cavitation bubbles with a self-focused laser beam. *OSA Trends Opt. Photonics Ser.* **96 A**, 257–258 (2004).

175. Li, Y. DYNAMICS OF LASER-INDUCED 3D MICROBUBBLES IN AN ABSORBING LIQUID. (UNIVERSITY OF DAYTON, 2019).

176. Muñoz-Pérez, F. M. *et al.* Steady-State 3D Trapping and Manipulation of Microbubbles Using Thermocapillary. *Front. Phys.* **8**, (2020).

177. Duhr, S. & Braun, D. Optothermal molecule trapping by opposing fluid flow with thermophoretic drift. *Phys. Rev. Lett.* **97**, 1–4 (2006).

178. Shi, Y. *et al.* Chirality-assisted lateral momentum transfer for bidirectional enantioselective separation. *Light Sci. Appl.* **9**, (2020).

179. Zenteno-Hernandez, J. A., Vazquez Lozano, J., Sarabia-Alonso, J. A., Ramirez-Ramirez, J. & Ramos-Garcia, R. Optical trapping in the presence of laser-induced thermal effects. *Opt. Lett.* **45**, (2020).

180. Lin, L., Hill, E. H., Peng, X. & Zheng, Y. Optothermal Manipulations of Colloidal Particles and Living Cells. *Acc. Chem. Res.* **51**, 1465–1474 (2018).

181. Jiang, Y., Pillai, S. & Green, M. A. Realistic Silver Optical Constants for Plasmonics. *Sci. Rep.* **6**, 1–7 (2016).
